MODULATIONS OF CLIMATE VARIABILITY ON GLOBAL AND SOUTHERN OCEAN CHANGES

by

Lina Wang

A dissertation submitted to the Faculty of the University of Delaware in partial fulfillment of the requirements for the degree of Doctor of Philosophy in Oceanography

Spring 2021

MODULATIONS OF CLIMATE VARIABILITY ON GLOBAL AND SOUTHERN OCEAN CHANGES

by

Lina Wang

Approved: ______________________________
Mark A. Moline, Ph.D.
Director of the School of Marine Science and Policy

Approved: ______________________________
Estella Atekwana, Ph.D.
Dean of the College of Earth, Ocean, and Environment

Approved: ______________________________
Louis F. Rossi, Ph.D.
Dean of the Graduate College and Vice Provost for Graduate and Professional Education

I certify that I have read this dissertation and that in my opinion it meets the academic and professional standard required by the University as a dissertation for the degree of Doctor of Philosophy.

Signed: ______________________________

Xiao-Hai Yan, Ph.D.
Professor in charge of dissertation

I certify that I have read this dissertation and that in my opinion it meets the academic and professional standard required by the University as a dissertation for the degree of Doctor of Philosophy.

Signed: ______________________________

Xinfeng Liang, Ph.D.
Member of dissertation committee

I certify that I have read this dissertation and that in my opinion it meets the academic and professional standard required by the University as a dissertation for the degree of Doctor of Philosophy.

Signed: ______________________________

Wei Zhuang, Ph.D.
Member of dissertation committee

I certify that I have read this dissertation and that in my opinion it meets the academic and professional standard required by the University as a dissertation for the degree of Doctor of Philosophy.

Signed: ______________________________

Weiwei Zhang, Ph.D.
Member of dissertation committee

ACKNOWLEDGMENTS

I had a wonderful journey for this five years PhD program at UD. My thanks and appreciation to all these individuals for being part of this journey and making this dissertation possible.

Firstly, I would like to express my gratitude to my advisor Prof. Xiao-Hai Yan and my co-author Dr. Kewei Lyu for their great support and the valuable scientific guidance on my research. I would like to extend my gratefulness to the committee members, Dr. Xinfeng Liang, Dr. Wei Zhuang, Dr. Weiwei Zhang for their valuable feedback throughout this research.

I am also grateful to Dr. Victor Klemas and my master's advisor Prof. Wei-ran Pan, for their encouragement and support for my life here. In addition, I would like to show my appreciation to my statistical professors, Dr. Tomas Ilvento, Dr. Palaniappa Krishnan, Dr. Jing Qiu, for building my knowledge in Statistics. And I am thankful to my classmates, Lei Huang, Zelun Wu and Liangliang Yang for sharing their expertise on this research.

In addition, I thank my dear friends, Vahap Demir, Hall Withlock, Rusty Jordan, Jing Xu and those from WCEC, BHC, Mike&Karen's, and RUF for their love and care, and the wonderful dinner dicussions we spend together. Most importantly, I thank my family, especially my mom, I thank her for her continuous and unparalleled love throughout my life. This journey would not have been possible if not for them, and I dedicate this milestone to all of you.

TABLE OF CONTENTS

Appendix

LIST OF TABLES

LIST OF FIGURES

ABSTRACT

The historical global surface temperature (GST) exhibits staircase-like evolutions with both accelerated warming periods and warming slowdown periods. The rate of GST change slowed down during 2003-2012, relative to the warming acceleration in the late 20th century and is termed as the global warming slowdown period. Since 1850, other global warming slowdown periods have also been identified. The proposed explanations for this warming slowdown can be understood as whether it is caused by the external forcing (e.g. the increased volcano activities, the increased aerosols and decreased water vapor concentration) or it is due to the internal variability from the Pacific Ocean, the Indian Ocean, or the Atlantic Ocean. This study reviews the observed historical records, previous analysis, and offers interpretations of coupled climate model experiments, reconciles the proposed mechanisms and quantifies their relevant contributions to the GST evolution.

The first section of this study focuses on the surface signal, the evolution of GST, and the main drivers for the GST change in different time scales. In this section, the Ensemble Empirical Mode Decomposition (EEMD) method is applied to the observed GST time series for the period of 1850-2020, which is decomposed into a group of signals respectively on inter-annual (< 8 years), inter-decadal (9-20 years) and multi-decadal (60-80 years) timescales as well as a non-linear secular trend. Both the inter-annual and inter-decadal signals in GST can be linked to the El Niño-Southern Oscillation (ENSO)-like variability in the Pacific Ocean. In contrast, the

multi-decadal signal in GST is in phase with the Atlantic Multi-decadal Oscillation (AMO) and the associated sea surface temperature (SST) patterns resemble the AMO in the North Atlantic and its trans-basin footprints in the other oceans. In order to assess the respective roles of the Pacific, the Atlantic, and the external forcing in driving the GST change in historical records, a suit of Pacemaker experiments has been examined. It has been revealed that the Pacific is the main driver of the GST change on inter-annual and inter-decadal time scales. The Atlantic also contributes to the GST change on inter-decadal time scales through the atmosphere bridge teleconnection. The external forcing is capable of reproducing the timing and phase of the GST change and can successfully reproduce the observed multidecadal variability (MDV) spatial pattern. The results further suggest that the prolonged hiatus periods of ~30 years (1945-1975) are mainly attributed to the multi-decadal signal, whereas the relatively short-term hiatus events, such as the recent one over 2003-2012, are mainly caused by the inter-decadal signal. The findings in this section reconcile the debate on whether the Atlantic Ocean or the Pacific plays a critical role in modulating the GST changing rates.

The second section of this study emphasizes the energy redistribution in the Southern Ocean which also modulates the GST changes addressed in the first section. The recent global surface warming slowdown is associated with an increased heat uptake in the deep ocean, particularly, the Southern Hemisphere oceans experienced rapid warming during the decadal long global surface warming slowdown (2003–2012) and the earlier Argo period over 2006–2013. However, in this section, updated observations are examined to show that this rapid warming has slowed down, leading to less contribution of the Southern Hemisphere oceans to the global ocean heat storage (~65% over the available Argo period 2006–2019). Two warming hotspot regions, the Southeast Indian Ocean and the South Pacific Ocean have experienced cooling over 2013–2019. This decadal shift is related to variations in the Southern Annular Mode (SAM) and Interdecadal Pacific Oscillation (IPO). It has been further suggested that the isopycnal deepening (shoaling) forced by changing winds dominated the regional ocean temperature changes over the earlier warming (later cooling) period. The finding in this section demonstrates how decadal variability modulates long-term climate change and provides important observational information for the ongoing calibration of decadal prediction systems.

In the third section of this study, the role of Pacific forcing in enhancing the early 21st-century rapid warming in the Southern Ocean is further investigated. Using CESM large ensemble (CESM-LE) experiment and Pacific Pacemaker (CESM-PAC) experiment help to better understand the contributions of internal forcing associated with the eastern tropical Pacific SST change and impacts of external forcing on the Southern Ocean heat content change. Consistent with ocean reanalysis, the tropical Pacific forced signals can reproduce a pronounced La Niña-like warming pattern with enhanced warming in the Southeast Indian Ocean (SEIO) and South Pacific Ocean (SPAC), and cooling in the eastern Pacific Ocean. Around 1/3 of the peaks of warming in the mid-latitude of Southern Hemisphere oceans warming is estimated to be controlled by the tropical Pacific forcing through Pacific teleconnection. On the contrary, the external forcing performed by the CESM-LE experiment can only generate uniform warming, indicating the tropical Pacific is the main contributor to the rapid Southern Ocean warming during 2003-2012. Furthermore, the Empirical Orthogonal Function (EOF) decomposition method is utilized to identify the dominant spatial mode of ocean heat variability in the Southern Hemisphere oceans. The extracted first mode explaining 24% of the variance is the most influential mode related to the tropical interdecadal Pacific Oscillation (IPO) and is consistent with the CESM-PAC simulation. The second mode is related to the Southern Annular Mode (SAM). These two modes show that both SAM and IPO are the drivers of this Southern Ocean warming slowdown since 2013.

This study reconciles the explanations of whether the external forcing, the Atlantic Ocean or the Pacific Ocean plays a vital role in modulating the GST changing rates. And it further demonstrates how the Pacific together with the SAM drives the decadal variability in the Southern Ocean. Overall, this study provides important observational information for the ongoing calibration of climate prediction systems.

Chapter 1

INTRODUCTION

1.1 Background

The GST showed a century-long warming trend with decadal fluctuations since 1850 (Easterling and Wehner, 2009). The Fifth Assessment Report (AR5) of the Intergovernmental Panel on Climate Change (IPCC) claims that the upward warming trend of GST during 1998–2012 has been observed slowing (0.05 [−0.05 to +0.15] °C per decade) over 1998–2012, shows a smaller upward trend than the estimated warming trend over 1951–2012 (0.12 [0.08–0.14] °C per decade) (Hartmann et al., 2013). Many studies name it as “global warming hiatus”. When updated to 2014 (Karl et al., 2015), the rate of GST change started increasing. Now the “surface warming slowdown” is widely used to recognize that period (Yan et al., 2016).

This warming slowdown has received substantial interest and raises vigorous debate on whether this unexpected warming slowdown is caused by the natural processes or the external forced responses in the Earth system. Several studies suggest that the external forcing is the main driver for this surface warming slowdown. For example, the strong volcanic eruptions (Santer et al., 2014), weak solar activities (Fröhlich, 2012), increased anthropogenic aerosols concentrations (Smith et al., 2016), and decreased water vapor concentrations (Solomon et al., 2010) are proposed to have important contributions to this warming slowdown. Other studies emphasize contributions of the internal climate variability that generated from the major ocean basins, such as the Indian Ocean (Lee et al., 2015), the Pacific (England et al., 2014), the Atlantic (Stolpe et al., 2018) and the Southern Ocean (Chen and Tung, 2014), and the combinations of different oceans. For example, research has provided evidence that the positive (negative) phase transformation of the Interdecadal Pacific Oscillation (IPO) has contributed to the downward (upward) trend of GST change (Meehl et al., 2013; Brown et al., 2017). By prescribing the observed historical Sea Surface Temperature (SST) in the eastern tropical Pacific, climate model simulations successfully capture the major characteristics of the recent warming slowdown in observed GST (Kosaka and Xie,2013), showing that the current warming slowdown is due to the decadal cooling in the equatorial Pacific. Dai et al. (2015) examines the contribution of the leading mode of the interval climate variability to the observed GST change and lend support to the claim that the IPO related leading mode accounts for the decadal fluctuations in surface temperature change, especially the recent slowdown from 2000 to 2013 is largely attributed by IPO phase transition.

In addition, the Atlantic Multidecadal Oscillation (AMO) regarded as the leading natural variability in the North Atlantic, is another primary climate mode that has been suggested to cause the recent warming slowdown (Chen and Tung, 2017). Some authors point out that the weakened Atlantic Meridional Overturing Circulation (AMOC) variability transported heat into deeper layers in the in Atlantic and Southern Ocean, leading to surface warming slowdown (Chen and Tung, 2014, 2018). Other authors propose that the enhanced warming in the tropical Atlantic could drive the eastern Pacific cooling through basin wide atmosphere teleconnection and contribute to the pause in the global surface warming (McGregor et al., 2014; Li et al., 2016; Kucharski et al., 2016). Specifically, the Atlantic warming intensifies the easterly trade wind in the Pacific and Walk circulation, thereby enhancing the La Niña type response over the tropical Pacific, and thus leading to the recent decreased warming trend in GST change (Li et al., 2016).

In the study of Xie and Kosaka (2017), two approaches are suggested to study the historical GST evolution and to explore the underlying physical mechanisms of the recent global warming slowdown. The first approach is based on the view of surface signals that associated with the modulations by the internal climate variability arising from ocean basins. Using the decomposition analysis, recent studies reveal that the time series of GST contains signals with frequency bands ranging from interannual to multidecadal time scales (Wu et al., 2011; Wei et al., 2015). The oceans are the sources of these frequency dependent variabilities as they have much greater heat capacity than the land and the atmosphere. The Pacific contributes to the GST change mostly on the high frequency variabilities through is mostly associated with El Nino-Southern Oscillation (ENSO) and IPO, while the Atlantic is mainly responsible for the low frequency variability around 60 years through AMO (Chen and Tung, 2017).

The recent studies based on the climate model simulations bring more information on how the Pacific and the Atlantic modulate the global temperature change in different time scales. The “pacemaker” experiments prescribed with the observed SSTs and wind stress anomalies in the equatorial Pacific have been compared with observations, showing strong evidence that the interval variability in the Pacific accelerates and reduces the global warming rate (Kosaka and Xie, 2013; Watanabe et al., 2014). These pacemaker experiments input with the observed central-eastern tropical Pacific SST anomalies, and set with a negative phase of the IPO, successfully reproduce the recent warming hiatus. The underlying physical process is that the intensified Pacific trade winds accelerates the Pacific Ocean shallow overturning cells, thereby increases the upwelling of cold water at the eastern equatorial Pacific, leading to more ocean heat accumulated in the western Pacific (England et al. 2014; Maher et al. 2018). The strengthened Indonesian throughflow (ITF) transports this accelerated heat into the Indian Ocean and mostly stores in the upper 700m, contributing to an enhanced warming in the east of Indian Ocean (Lee et al. 2015).

The second approach for studying the historical GST and the warming slowdown emphases on energy redistribution perspective, specifically on ocean heat content (OHC). Previous research reports that more than 90% of the heat absorbed by Earth during 1971–2010 is stored in oceans (Rhein et al., 2013). The continuously increases in the global OHC over the hiatus period in the early 2000s also reveals oceans play a critical role in modulating the global surface warming and cooling. Thus, the second approach aims to relate the recent warming hiatus to the ocean heat redistribution in the subsurface oceans. The early study of Liu et al. (2016) suggests the increased heat in upper layers (<350m) of the Pacific and the Indian Ocean contributes to the slow-down in the GST. Over time, the coupled climate model simulations and observations consistent show that the increased heat uptake in the deep layers (>750m) of the Atlantic slows the surface warming (Levitus et al., 2012). In addition to the Atlantic, the Southern Ocean has received much attention due to its recent rapid warming (Tung and Chen, 2018). The Pacific and the Indian Ocean are suggested to be the main drivers of the horizontal exchanges of heat in the upper 300 m, while the Atlantic and the Southern Ocean is mainly responsible for the vertical redistribution in the depth of 200–1500 meters (Tung and Chen, 2018). When Argo floats are widely employed in the global scale, the dominance of the Southern Ocean in the global ocean heat uptakes is confirmed (Roemmich et al., 2015). The rapid warming in the Southern Ocean with most of the heat uptake located around 40°S is associated with the strengthening and poleward shift of the Southern Hemisphere westerly winds that steepens the isopycnal surface and carries large percentage of heat into the deeper layers (Llovel and Terray, 2016). The results of these prior research appear consistent in some degree, however, a number of questions regarding how these oceans modulate the GST in time scales over the historical periods are still uncleared.

1.2 Objectives and Motivation

Substantial work has been done to study the mechanisms of GST change in historical period and the recent warming slowdown from both the surface information and the Earth's interior energy redistribution. These studies are consistent in some respects, but how and how much these derivers modulate the GST change in different time periods, either accelerated warming periods or warming slowdown periods, still need further investigation. Furthermore, since 2006, the international Argo program has been providing continuous real-time ocean observations in the upper 2000 m from a near-global array of autonomous profiling floats. Previous studies based on the earlier Argo record (2006–2013) have shown rapid warming in the Southern Hemisphere Oceans and most of the global ocean heat storage occurred in the Southern Hemisphere (Roemmich et al., 2015). However, updated observations show that this rapid warming has slowed down and was even changed to cooling in certain regions since 2013. This shift is mainly driven by changing winds through the downwelling of the upper-layer warmer waters over the earlier period and the upward pumping of subsurface cooler waters over the later period. Improved understanding of the ocean heat redistribution and the underlying physical mechanisms will help to better monitor and quantify the impacts on the climate change.

Therefore, this study aims to investigate the role of ocean heat uptake in modulating the global warming rate. The objectives for this study are listed as below:

1. Identify the role of the Pacific, Atlantic and external forcing in modulating the evolution of GST change in historical record and quantify their contributions to the recent warming slowdown.

2. Investigate the mechanisms and drivers of the recent decadal shift of the Southern Ocean warming.

3. Investigate the role of tropical Pacific forcing in the early 21st century rapid warming in the Southern Ocean warming.

Accordingly, this dissertation is divided into three sections.

a) In the 2nd chapter, the GST time series is studied based on the observational dataset HadCRUT4 and the Community Earth System Model Large Ensemble (CESM-LE) Project (Kay et al. 2015), assessing the relevant role of both external and internal variability, particularly, the tropical Pacific forcing and the Atlantic forcing, in the GST changes over the historical period.

b) In the 3rd chapter, the underlying physical mechanisms of the rapid warming in the Southern Ocean and the global surface warming during slowdown period (2003–2012) and its shift afterwards, are examined using temperature decomposition (Bindoff and McDougall, 1994), their impacts on ocean heat redistribution and global temperature change during historical period since 1960s are also studied.

c) In the 4th chapter, the early 21st century rapid warming in the Southern Ocean is investigated using a coupled climate model experiment, in which the observed SST anomalies in the tropical Pacific are nudged in the model simulations to study the Pacific impacts on this warming.

Chapter 2

FREQUENCY-DEPENDENT MODULATORS OF THE HISTORICAL GLOBAL SURFACE TEMPERATURE CHANGE

2.1 Introduction

The historical global surface temperature (GST) exhibited complex multi-timescale variations. On decadal and longer timescales, the GST displays staircase-like evolutions with alternate warming acceleration periods and warming slowdown (often referred to as "hiatus") periods (Easterling and Wehner 2009; Foster and Rahmstorf, 2011).

External variability due to solar activity, water vapor concentrations and aerosol concentrations have been suggested to explain this phenomenon (Lean and Rind, 2009; Kaufmann et al., 2011; Solomon et al., 2010, 2011; Stauning, 2013; Santer et al., 2014). Internal variability is proposed as another primarily factor that affects the global warming rates through heat redistribution in the subsurface of oceans (Balmaseda et al., 2013). The Pacific and the Atlantic are main sources of the internal variability such as the ENSO (Loeb et al., 2012), IPO and PDO (Trenberth,2015) and AMO (Zhang and Delworth, 2007; McGregor et al., 2014).

By decomposing the GST into various characteristic timescales, some studies demonstrate that the importance of multi-decadal variability (MDV) in modulating the surface warming and cooling and attribute the slowing warming rate in the GST to the MDV's declined rising trend (Wu et al., 2011; Yao et al., 2016; Wei et al., 2015). Wu et al. (2011) states that up to one third of the rapid warming in the late twentieth century is contributed by a long-term warming trend and the multidecadal variability with mean period of 60-70 years which is associated with internal low frequency oscillations in the North Atlantic. A more comprehensive description can be found in Tung and Zhou (2013) who has reviewed both the latest HadCRUT4 data and the longest Central England Temperature data, and indicate the MDV is associated with the internal multidecadal variability in Atlantic and contributes around 40% of the observed warming trend over the past 50 years. By contrast, Meehl et al. (2016b) and Trenberth (2015) suggest that IPO and PDO have played more dominant role in such a multidecadal variation in the GST change. Some studies also address the debate on whether GST low frequency fluctuations is induced by the anthropogenic aerosol forcing (Booth et al. 2012; Zhang et al. 2013).

There is substantial uncertainty in the external and internal variabilities, their relative contributions to the observed GST change. Therefore, this study tries to reconcile the diverging views on the global temperature change mechanisms. The EEMD method is applied to the GST time series both on the observational data and a large ensemble of coupled climate model simulations to assess the relative role of the external and internal variability originated from Pacific and Atlantic in modulating the GST change over the historical record.

2.2 Data and Method

2.2.1 Observational datasets

The GST data is obtained from the combined land and ocean surface temperature anomaly data which is derived from Hadley Centre–Climatic Research Unit (HadCRUT) version 4.1.1.0 (1850-present). For SST data, we use the Extended

Reconstructed Sea Surface Temperature version 5 data (ERSST V5) which is obtained from the International Comprehensive Ocean–Atmosphere Dataset (ICOADS) (1854-present; Huang et al., 2017).

2.2.2 Coupled climate model experiments

Four model experiments are analyzed to identify the role of the external forced, Atlantic forced and Pacific forced responses in the GST simulation.

The first two model experiments are based on the fully coupled Community Earth System Model simulations (CESM1) (Kay et al., 2015), beginning in 1920 and ending in 2013. The output from a 40-member CESM Large Ensemble simulation (denoted CESM-LE) is analyzed to examine the external forcing, including greenhouse emissions, ozone, anthropogenic aerosols, land and solar radiance. Each ensemble member is prescribed with the same historical radiative forcing, but the start atmosphere conditions in the model simulation are slightly different, while the input initial conditions of ocean component are identical in all ensemble members. The discrepancy of the simulated GST among ensemble members is the generated by the internal variabilities from the atmosphere white noise. The ensemble-mean of all members can remove the internal forcing effect and only leave external forcing responses. The output from a 20-member ensemble of Pacific Pacemaker simulation (denoted CESM-PAC) is also analyzed. This simulation uses the identical model, forcing and initial conditions as the CESM-LE, the difference is nudged observed SSTs in the central-eastern equatorial Pacific (15° S–15° N, 180° W to the coast of South America) is obtained from the NOAA Extended Reconstruction Sea Surface Temperature, version 3 dataset (ERSSTv3b), allowing the rest of the model free to evolve. In this way, Pacific sets the pace and its forced response in the model simulation can be evaluated by the mean of all ensemble members.

Moreover, to examine the role of aerosol forcing on GST change in history, we use daily meteorological forcing from the CESM Single forcing Large Ensemble Project (Deser et al., 2020b; www.cesm.ucar.edu/working_groups/CVC/simulations/cesm1-single_forcing_le.html). The 'ALL-but-one-forcing-fixed' experiments follow the same simulation protocol as the CESM-LE project, with one forcing kept as constant at the start of simulation (1920). The fixed forcing can be biomass burning aerosols (BMB), industrial aerosols (AER), greenhouse gases (GHG) or land-use/land-cover (LULC) (Deser et al., 2020a). Here, a 20-members CESM-xaer model experiment with fixed observed industrial aerosol is used to isolating the aerosol forcing from other anthropogenic forcing agency.

The last model experiment with a 10-member ensemble of Atlantic Pacemaker experiments (referred as CESM-ATL) is used to identify the role of Atlantic forcing in GST change. In this model experiment, the climatology monthly SSTs is nudged in the North Atlantic (5ºN-55ºN). Also, the CO_2 emissions is set as constant at the middle of twentieth century.

2.2.3 Data analysis method

The GST contains signals in different time scales. To extract different frequency signals, the Ensemble Empirical Mode Decomposition (EEMD) (Wu and Huang, 2009) is applied both on the observed and modeled GST time series. The decomposed GST components are divided into three groups and a nonlinear monotonically increasing secular trend. The first group is defined as Inter-annual variability (IAV) with all periods below 8 years. The second group is termed as Inter-decadal variability (IDV) with a ~ 9 to 30-year periods. The last group is multi-decadal variability (MDV) with a mean period of around 60 years.

Simulations by individual ensemble members represent a combination of the forced response. While ensemble mean filters out the internal variability that beyond the forced ocean, retaining the forced response. Therefore, we process all the model experiments in the following steps. Firstly, GST simulated by each ensemble member is decomposed into different time scales and grouped into four components. And then SST is regressed to these four components by the multiple linear regression method to get the correlation maps. Finally, the ensemble mean regression pattern is estimated for each component (See supplementary Figure A1). In order to estimate the responses forced purely by the tropical Pacific and the Atlantic, the ensemble mean of CESM-LE is removed from both the Pacific and the Atlantic pacemaker ensemble members before regression.

2.3 Observational results analysis

Previous studies have applied EEMD method on GST time series using datasets ended in 2012 (Yao et al., 2016), this may influence the decomposition results as the EEMD is sensitive to the end and start date. Here, we use the updated HadCRUT4.5 GST data starting from 1850 to 2020 for EEMD decomposition. As the model experiment simulation period over 1920-2013 is shorter than the observed period, the period combinations of 1850-2020, 1850-2013, 1880-2020, 1920-2020 are selected to test the impact of the start and end date by EEMD. As shown in Figure 1, the decomposed IAV, IDV, and ST based on different time periods are consistent. The MDV decomposed based on the period of 1850-2013 shows a decreasing trend at the endpoint 2013 compared to others (Figure 2.1d), suggesting decomposition based on a long period, 1850-2020, is more robust. Therefore, the observed decomposition is all based on 1850-2020 in the further analysis.

2.3.1 Time-frequency analysis of historical GST

The historical GST change is controlled by frequency-dependent modulators in different time periods. Figure 2.1 displays the GST based on the HadCRUT4.5 land and ocean surface observations from 1850 to 2020 (Brohan et al., 2006; Morice et al., 2012). Using the EEMD method, the original GST time series (Figure 2.1a, in gray) is decomposed into various frequency components. These components are divided into three groups and a non-linear monotonically increasing secular trend (Figure 2.1b-e).

The superimposed multidecadal variability over the long-term secular trend provides us an overall increasing GST embedded with alternate accelerated warming and warming slowdown periods since 1850 (Figure 2.1a, in red). With the interdecadal signal is superimposed on the smoothed line, the temperature appears frequently fluctuate around the smoothed line (Figure 2.1a, in blue). The peaks (floors) of IDV and MDV are enhanced when they reach peaks (floors) at the same time. The shifted IDV phase from positive to negative in the early 2000s successfully resembles the recent warming slow down. After 2013, this cooling phase shifted to a warming phase and held it ever since. The MDV has two dominant cooling phases during 1880-1910 and 1945-1975, showing the warming rate is contributed by the MDV and ST's upward trend, consistent with Wei et al. (2015).

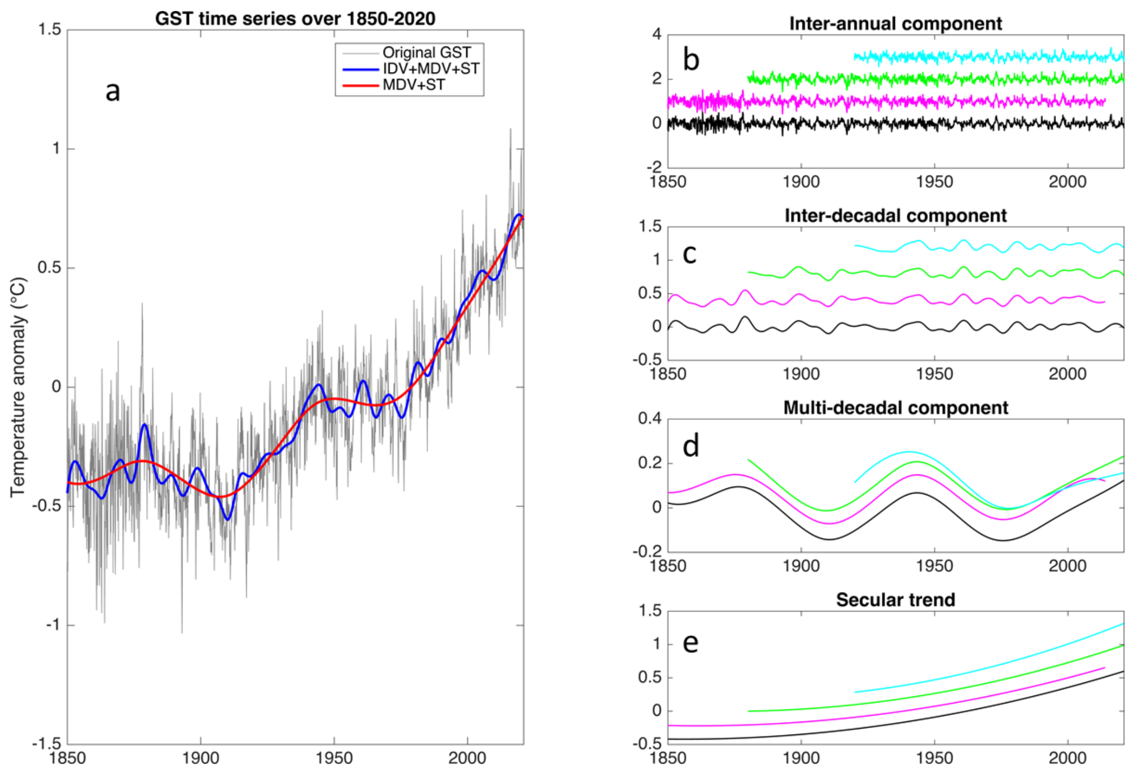

Figure 2.1. GST variations during 1850-2020 and its four components based on Hardcurt4.5 data. In a, the gray lines are the original GST change time series; the blue line is IDV+MDV+ST; the red line is MDV+ST. In b-e, black lines are the decomposition based on period of 1850-2020; pink lines are based on 1850-2013; green lines are based on 1880-2020 and the light blue lines are based on 1920-2020.

2.3.2 Modulation in different time periods

The GST has experienced a pronounced multi-decadal fluctuation. The recent warming slowdown also appeared in historical periods, such as the mid-twentieth century and the early 21st century (Kosaka and Xie, 2016; Meehl et al., 2016b). How signals on different time scales contribute to the historical surge and hiatus events. To address this question, the relative contributions of an individual component to GST change are quantified during difference time periods. The historical surge and hiatus periods are determined according to the threshold of the maximum magnitude of statistically significant trends in observed GST. During the two prolonged hiatus periods of ~30 years (1880-1910 and 1945-1975), the MDV plays the largest role, accounting for approximately 75% (-0.076 ℃/decade) and 54% (-0.086 ℃/decade) of the total GST warming rates, respectively. However, the IDV contribute more (-0.081 ℃/decade) to the GST cooling during the short warming slowdown period (1998-2014). For the accelerated warming periods (1911-1944 and 1976-1997), a large portion of the warming rate can be explained by MDV (0.058 °C/decade and 0.41 ℃/decade).

The two-dimensional parameter diagrams (Figure 2.2 and Figure 2.3) provide an alternative presentation showing the time-varying trends. The GST trends (Figure 2.2) and GST trends with removing one component (IAV, IDV, MDV) (Figure 2.3) are estimated for every possible time interval (larger than one year) by least-squares linear regression. Trends for time segments longer than 62 years are all positive. The overall warming trend is interrupted by two long periods of negative trends. Clearly, removing the MDV component can eliminate the existence of longer negative trends, while removing IDV results in fewer numbers of shorter periods of cooling (<15 years). More short periods of warming took place after removing the IAV component.

Furthermore, the running trends within the running windows of 10, 15, and 25 years are estimated for each component-time series (Figure 2.4). The 10 years running trend analysis (Figure 2.4a) clearly shows that the IAV and IDV are two main contributors to GST change in the decadal time scale fluctuation. For example, during the global warming slowdown period, 2003-2012, the IDV signal with a negative trend (-0.018 °C/year) contributes to 60% of the variance of GST change, regarded as the dominant driver for this warming slowdown. The IAV explains 30% of the warming slowdown according to its negative warming rate (-0.005°C/year) over the hiatus period. While the MDV and ST show a positive warming rate during this short 10-years hiatus period. Some studies argue that the hiatus period started from 1998 to 2012 which begins with one of the strongest El Niño events. Therefore, the 15-years running trend (Figure 2.4b) is also selected to test the contributions from these signals. Similar to the results with 10-years running window, the IDV and IAV are still the major contributors to this global warming slowdown, with dominance in the IDV time scale (-0.012°C/year). When the running window extends to 25-years (Figure 2.4c), the contributions of IDV and IAV variation become very small. The MDV signal becomes a dominant driver for the GST change.

This running trend analysis helps us to find that IDV is responsible for the recent warming slowdown, while MDV is most like to control the past prolonged hiatus events (e.g. mid-20 century).

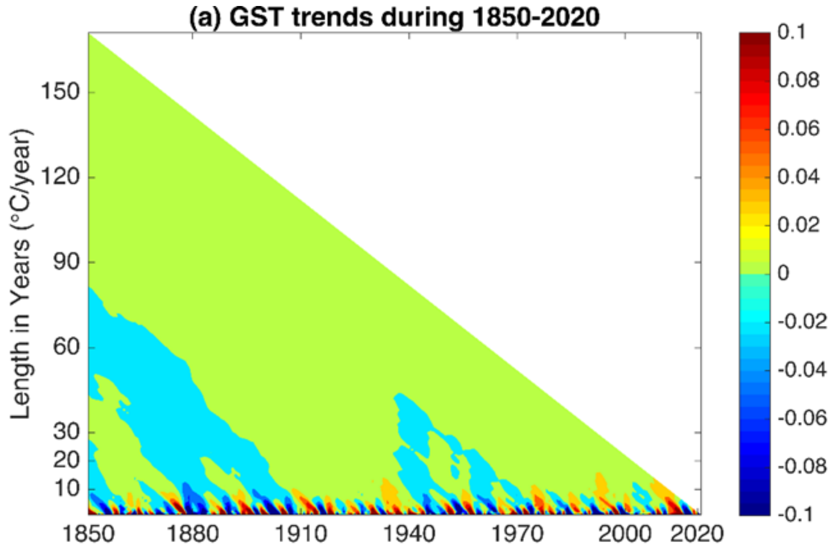

Figure 2.2. GST trends in different length of years during 1850-2020, unit: °C/year.

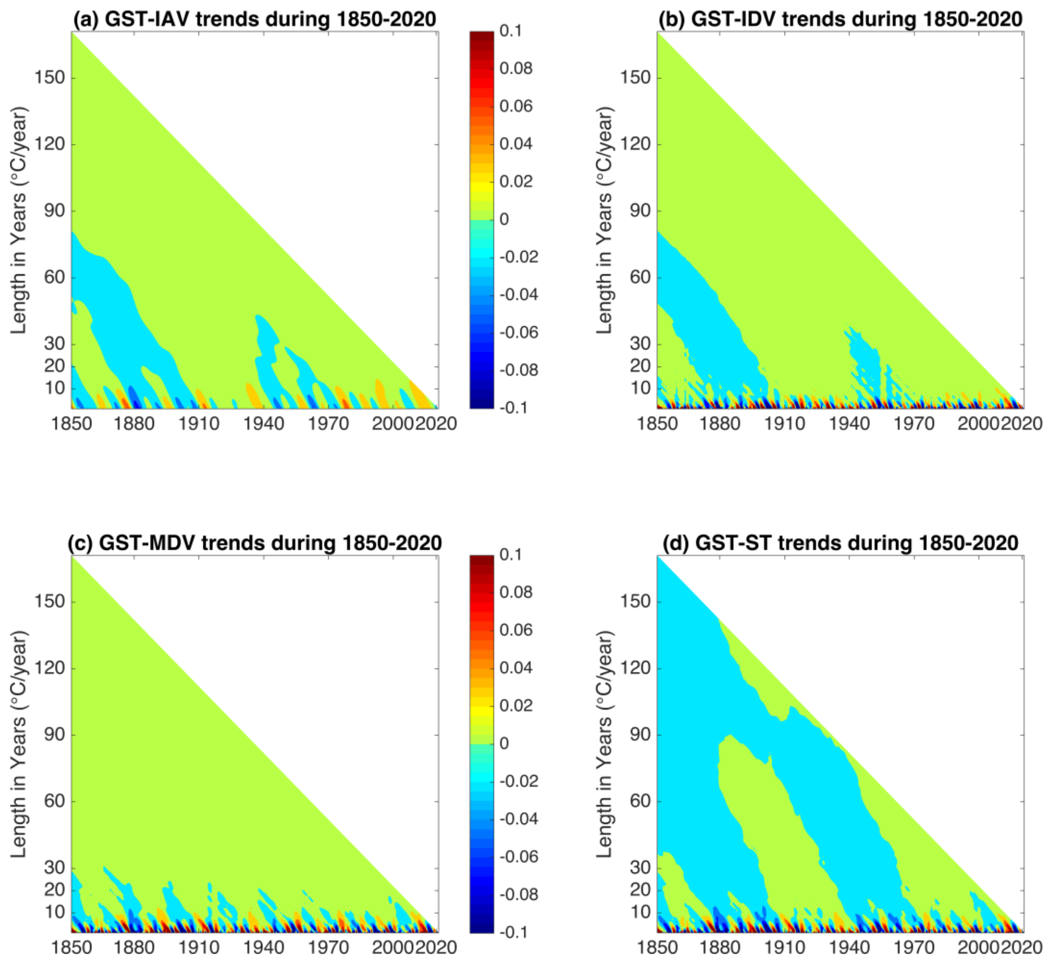

Figure 2.3. GST trends in different length of years during 1850-2020. (a) GST change removed IAV component. (b) GST change removed IDV component. (c) GST change removed MDV component. (d) GST change removed ST component.

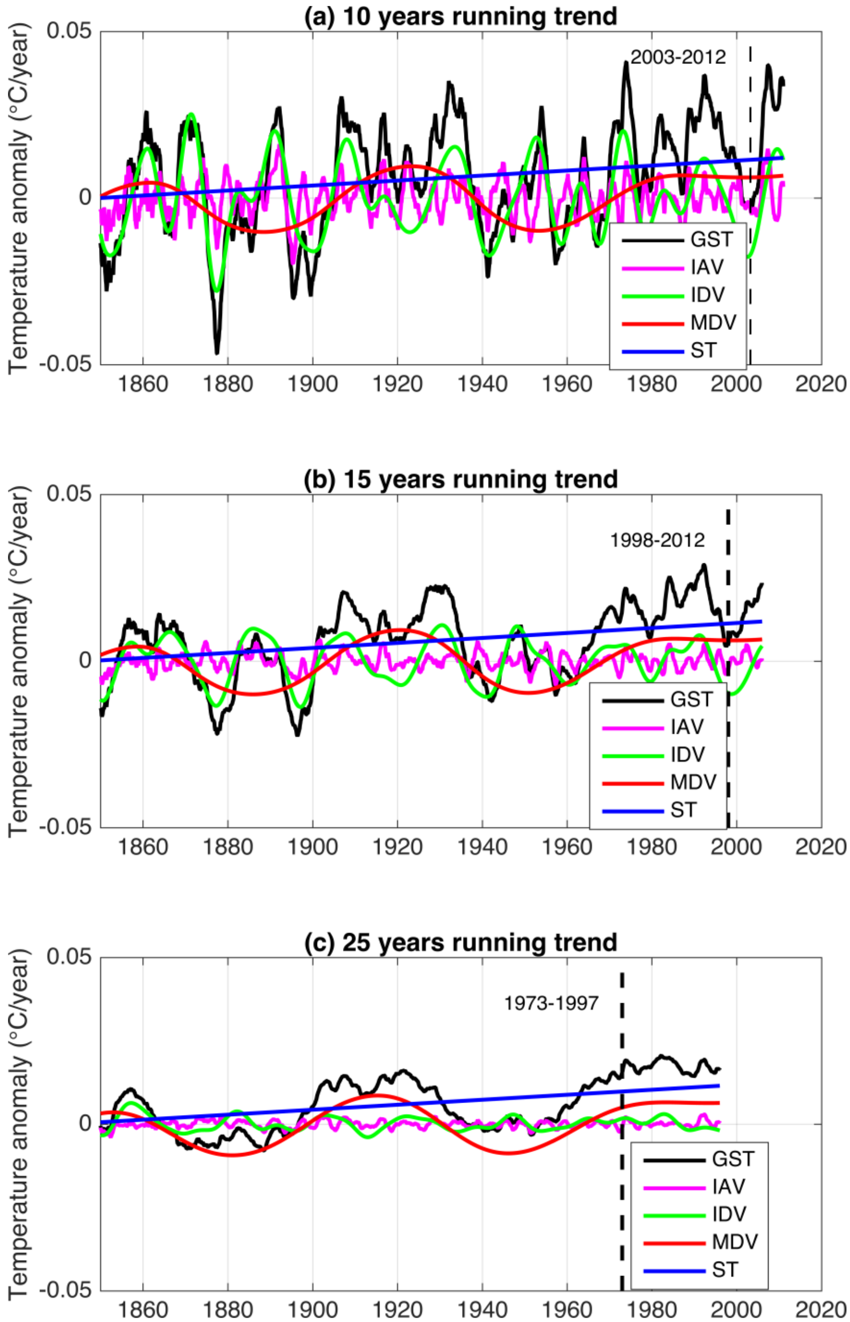

Figure 2.4. The running trends of GST time series and its four components. (a) 10 years running trend. (b) 15 years running trend. (c) 25 years running trend. Green lines are IAV signals, red lines are IDV signals, blue lines are MDV signals and black lines are ST.

2.3.3 Observational spatial pattern analysis

To identify the underlying oceanic physical processes that may have contributions to the GST change, the global monthly SST anomaly field is regressed onto the standardized IAV, IDV, MDV, and ST components for the period of 1920-2013 (Figure 2.5).

The IAV is ENSO related variability, as its spatial signature exhibits significant SST anomaly in the equatorial Pacific corresponding to the cold-tongue pattern (Chen and Tung, 2018). The IDV shows a similar spatial pattern with IAV, but with a more prominent SST anomaly in the extratropical Pacific. Zhang et al. (1997) explains the IDV is also referred as the ENSO-like variability due to its high correlations (r = 0.86) with the Cold Tongue Index. The signatures of the IDV on the SST field is not confined to the tropical eastern Pacific Ocean but extend to extratropical Pacific and the equatorial Indian Ocean and the North Atlantic Ocean. The connections between the tropical Pacific SST anomaly and SST variability in other oceans is modulated through the atmospheric bridge that enables ENSO to influence the remote oceans through anomalous heat and momentum fluxes (Alexander et al., 2002).

The spatial structure of the MDV is recognized as a tropical-wide SST pattern with significant warming in the North Atlantic, cooling in the eastern tropical Pacific, and warming in the subtropical Pacific and the Indian Ocean. This pattern is induced by the increased warming in the Atlantic through remote basin wide teleconnection (Li et al., 2016). The overall warming multidecadal SST signals in the North Atlantic and the Southern Ocean are generally out of phase with each other, which are suggested to be induced by the variations of AMOC (Seidov and Maslin, 2001). As the MDV is more strongly positively correlated with the AMO index (exceeding 0.8) rather than the negative correlation with the IPO index (approximately -0.4), it is confirmed that the MDV of GST is dominantly modulated by the SST changes in the North Atlantic, known as the AMO. The AMO variability has been reported to be driven by the internal variability from North Atlantic (Ting et al., 2009, 2014), in particular the AMOC (Knight et al., 2005; Delworth et al., 2016). However, this view has been challenged and several studies attribute the AMO to external forcing, such as aerosols and greenhouse gases (Otterå et al., 2010; Booth et al., 2012; Bellomo et al., 2016). Zhang et al. (2012) claims that the excessively strong aerosol effects in model simulation attributes to the discrepancies with observations, leading to an unrealistic MDV.

As for the ST component (Figure 2.d), the regression map exhibits the wide-spread warming trends over global oceans except for some patches of weak cooling in the Southern Ocean and the northwestern Atlantic Ocean. Previous studies have demonstrated that it is caused by the response to human-induced external forcing, particular the carbon dioxide (DelSole et al., 2011).

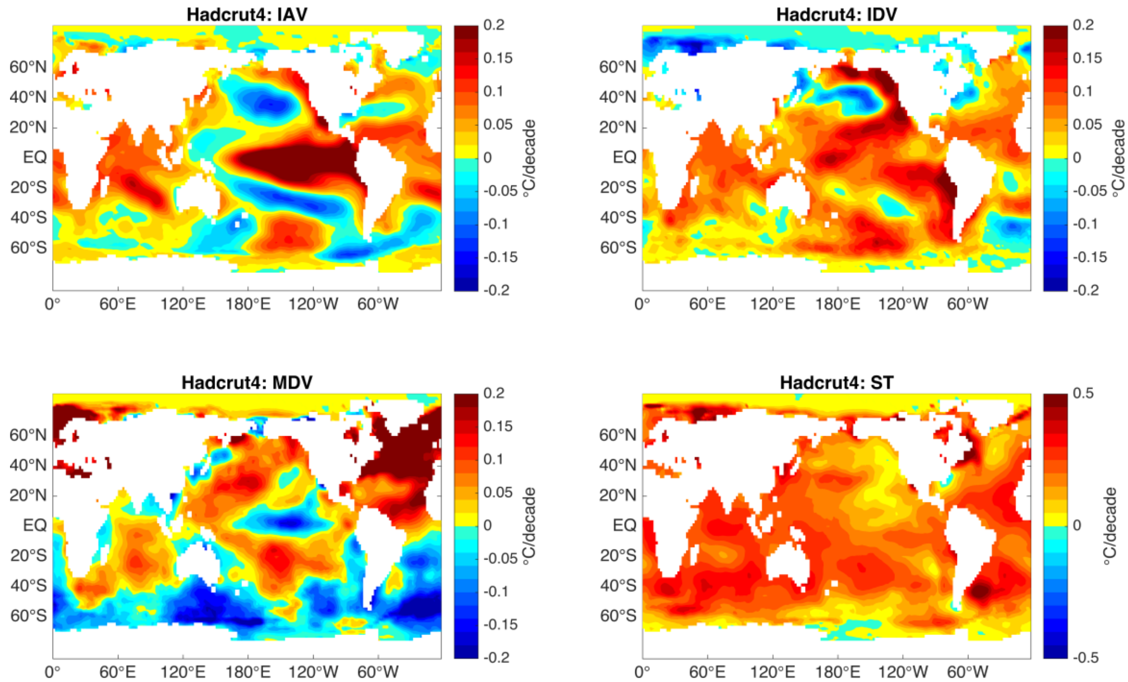

Figure 2.5. Regression of ERSST onto 4 components based on Hadcrut4 data set over 1920-2013. The 4 components have been normalized.

2.4 Analysis of coupled model experiments

The CESM-LE, CESM-xaer, Pacific Pacemaker and Atlantic Pacemaker model experiments are further used to analyze how the external forcing, the internal modes of internal climate variability in the Pacific and the Atlantic oceans modulated the historical GST change. Figure 2.6 depicts the time series of GST change estimated based on the observational data and the four model experiments. Correspondingly, Figure 2.7 displays the observed spatial patterns and those forced by the model simulations. Firstly, the externally forced responses are analyzed in order to compare with the contribution of aerosol forcing. And then, the Pacific and the Atlantic forced response are examined to quantify their contributions to the GST change.

2.4.1 CESM-LE model experiment

We begin with the CESM-LE model results. The ensemble mean of the CESM-LE model experiments represent the external radiative forced responses (termed as externally forced response, see methods). Thus, the 40-members of the CESM-LE is analyzed to address the contributions of the external forcing.

The external forcing can produce most part of the GST variation in the historical record (Figure A.1), except for the variation in the last decade. In particular, the external forcing is not able to reproduce the recent warming slowdown since the 2000s. In terms of the four components of time series (Figure 2.6), the external forcing can explain very little (~1%) GST variation in the interannual time scale. But the percentage that could use to explain the external forcing has increased to 18% in interdecadal time scale. This ratio further increased to 56%~75% in the multidecadal time scale. Clearly from the time series analysis, each ensemble the simulated MDVs from ensemble members and the ensemble mean all exhibit consistent phase change compared with the observed MDV change, showing that the external forcing is the main factor controlling GST change in multi-decadal time scale, consistent with previous studies that the external forcing is responsible for the MDV of GST. In addition, the CESM-LE simulations faithfully reproduced the observed MDV spatial pattern (Figure 2.7) characterized with large warming in the subtropical western Pacific, the tropical Indian Ocean, and the North Atlantic, and a cooling in the eastern tropical Pacific Ocean, except for the opposite phase in the Southern Ocean and south of Atlantic Ocean. Furthermore, the externally forced signal counted 96% of the variance of ST, suggesting it is the main contributor to the long-term warming.

Therefore, based on the CESM-LE experiment, we conclude that the external forcing is the dominant factor controlling the GST change on the multi-decadal and longer time scales.

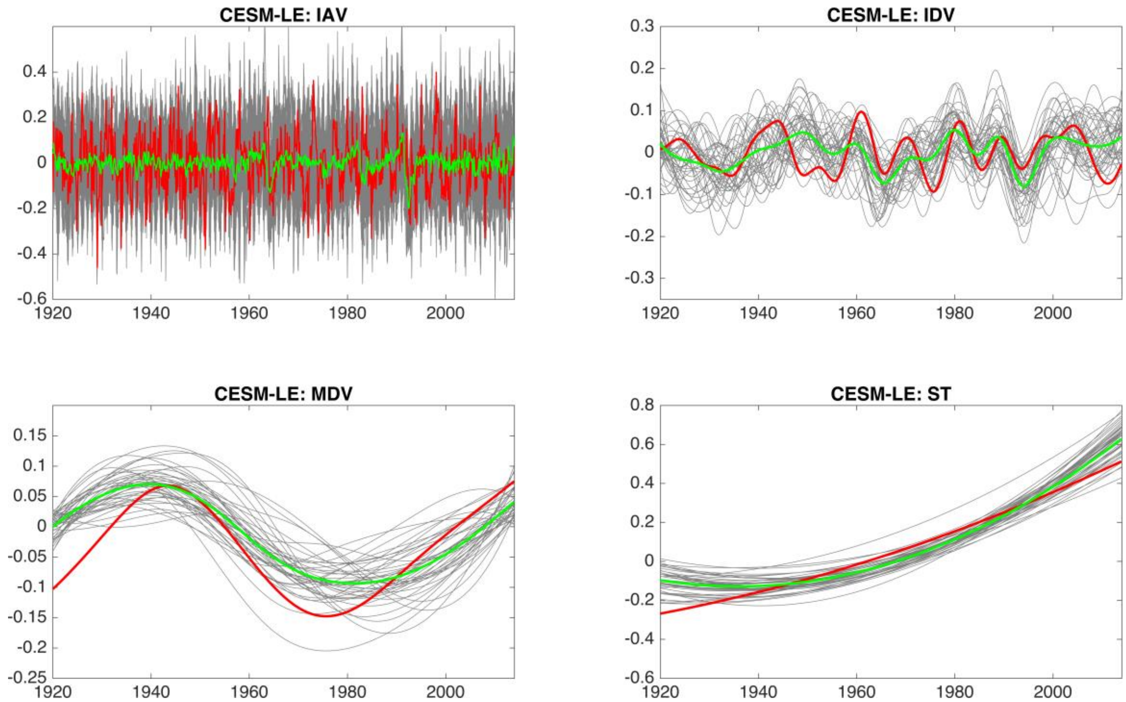

Figure 2.6. The four components (IAV, IDV, MDV and ST) of GST change over 1920-2013 forced by CESM-LE experiment. The gray lines are ensemble members. The green line is the ensemble mean of CESM-LE. The red line is the observed GST change estimated by HadCRUT4 data set.

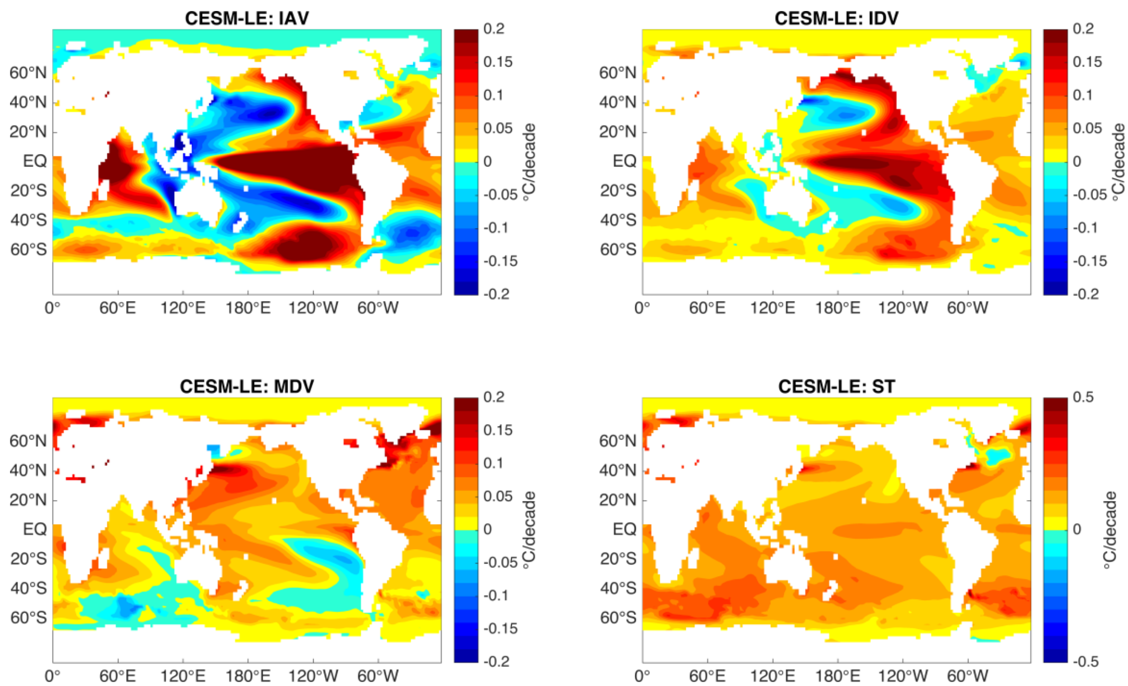

Figure 2.7. Regression of ERSST onto 4 components based on CESM-LE model experiment over 1920-2013. The 4 components have been normalized.

2.4.2 CESM-xaer model experiment

Aerosol forcing is another factor reported having an impact on the GST change. Next, we use the CESM-xaer model experiment which has the fixed industrial aerosol forcing to identify the role of aerosol forcing in modulating the GST change.

The forced IAV and IDV by CESM-xaer (Figure 2.8, IAV and IDV, green lines) shows little change compared to the externally forced signals (Figure 2.6, IAV and IDV, green lines). This little change is consistent in all the ensemble members, suggesting the aerosol forcing is not dominant in driving IAV and IDV in GST change. However, on the multi-decadal time scale, CESM-xaer (Figure 2.8, MDV, green line) shows much weaker variability, whose varying amplitude is ~1/4 of that in CESM-LE (Figure 2.6, MDV, green line) and only explaining 18% of the total observed variance. Moreover, the spatial pattern (Figure 2.9, MDV) generated by CESM-xaer shows a large discrepancy compared to that forced by external forcing (Figure 2.7, MDV), indicating the aerosol forcing largely contributed to GST change in multi-decadal time scale. The long-term warming becomes stronger as well due to less aerosol-induced offsetting on the radiative heat fluxes.

Thus, the aerosol forcing is found to be the main contributor for the MDV of GST among all the external forcing.

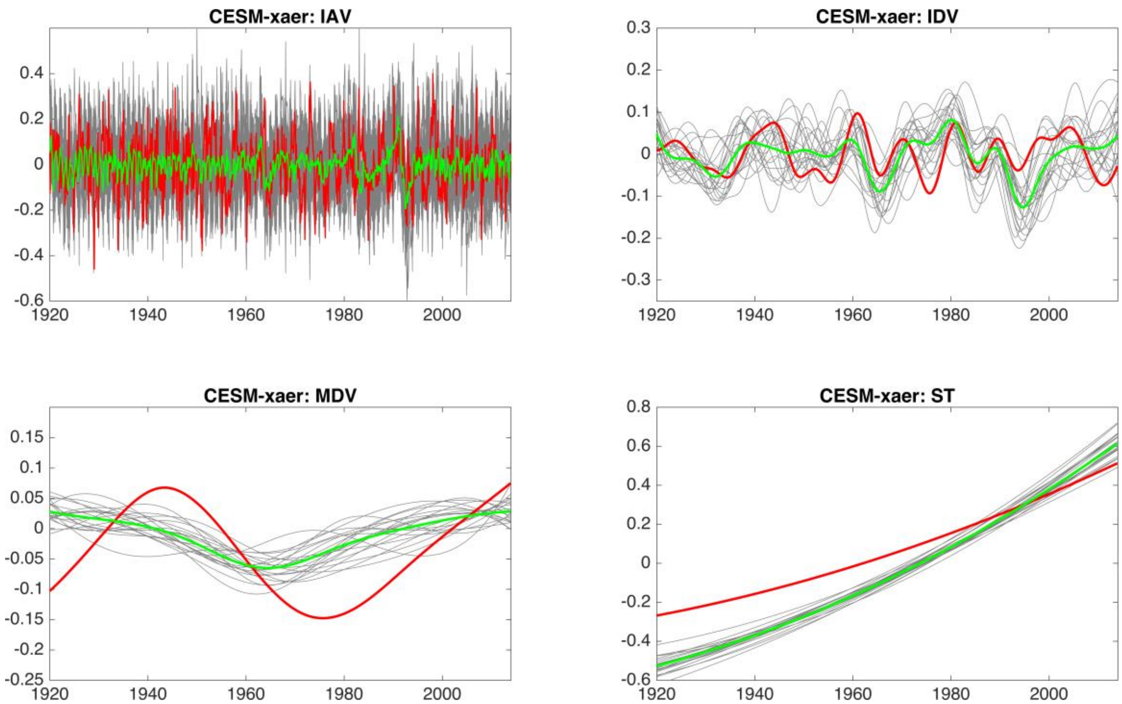

Figure 2.8. The four components (IAV, IDV, MDV and ST) of GST change over 1920-2013 forced by CESM-xaer experiment. The gray lines are ensemble members. The green line is the ensemble mean of CESM-xaer. The red line is the observed GST change estimated by HadCRUT4 data set.

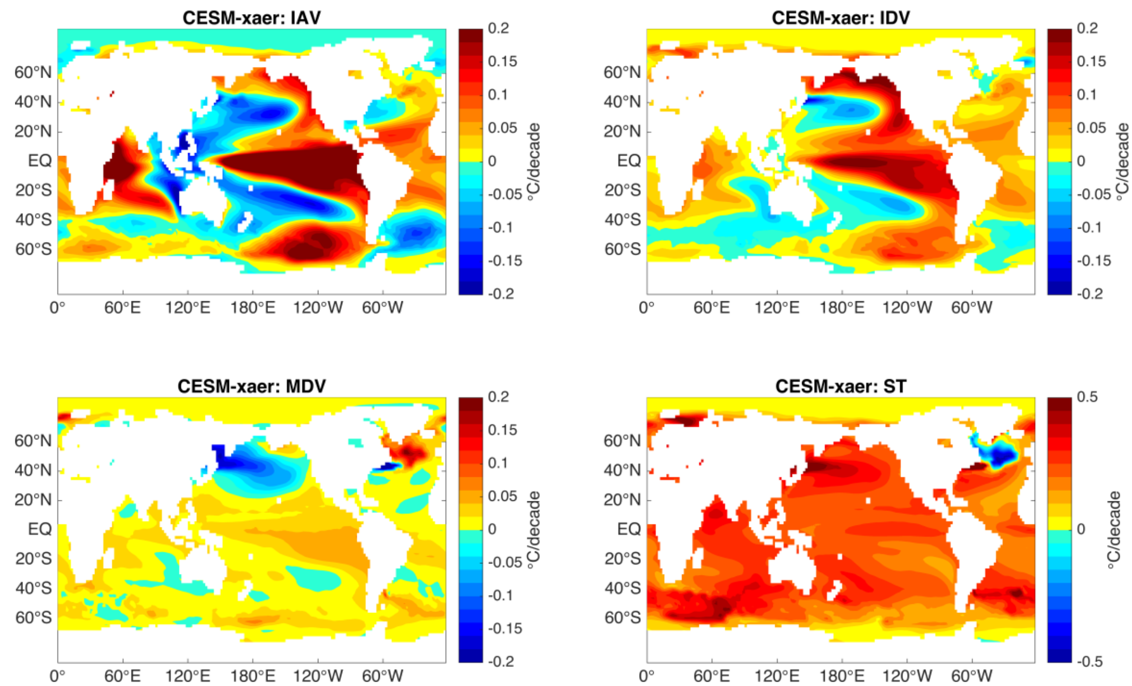

Figure 2.9. Regression of ERSST onto 4 components based on CESM-xaer model experiment over 1920-2013. The 4 components have been normalized.

2.4.3 Pacific Pacemaker model experiment

The CESM-LE and CESM-xaer model analysis suggest that the external forcing, especially the aerosol forcing is the dominant driver for the GST change in MDV and ST time scales. However, neither the external forcing nor the aerosol forcing shows a large contribution to the IAV and IDV of the GST change. What may drive the variation of high-frequency signals? Some studies illustrate that the coulpled climate mode in the tropical Pacific is the main driver of the GST change on interannual and interdecadal time scales. However, these studies focus on the Pacific's contribution to the global GST change. Here, we use the Pacific Pacemaker (denoted as CESM-PAC) model experiment to explore the role of the tropical Pacific forcing in modulating the GST change in different time scales. To obtain the forced signals purely from tropical Pacific, each ensemble member in the CESM-PAC model experiment has removed the external forcing by subtracting the ensemble mean of CESM-LE model. As shown in Figure 2.10, the CESM-PAC model faithfully reproduced most of the evolution of GST change in the historical record. In particular, the tropical Pacific forcing successfully reproduced the warming slowdown trend in the last decades, consistent with Kosaka and Xie (2013) that the Pacific is the main driver of the recent warming slowdown. Compared to other model simulations, the simulated time and phase of the IAV and IDV by CESM-PAC model experiment is highly consistent with the observations. The IAV and IDV forced by CESM-PAC explain 36% and 67% of the observed IAV and IDV, respectively. For example, the Pacific forced IDV reproduced the strong signals in 1997/1998(Figure 2.10, IDV). During the warming slowdown period between 2003-2012, the Pacific forcing explains over 60% of the observed negative trend.

The spatial pattern forced by tropical Pacific forcing is capable of capturing the most characteristics of the observed SST changes in the tropical area (Fig. 2.11). The dipole structures of warming in the western Pacific and cooling the eastern Pacific are successfully captured by the Pacific forced responses. In particular, the Pacific cooling is significant in the ensemble simulations during the hiatus period 2003-2012, implying the IAV and IDV in the GST change are primarily driven by the interval variability in the equatorial eastern Pacific. On the multi-decadal time scale, the amplitude of MDV forced by the Pacific is very weak. And the corresponding MDV pattern is distinct from the observational result. In addition, the tropical Pacific forcing is not able to generate a long-term warming trend.

The result of CESM-PAC model experiment reveals that the Pacific forcing has strong control on the interannual and interdecadal time scales, but it has limited power to drive the GST change on the multi-decadal and longer-term time scales.

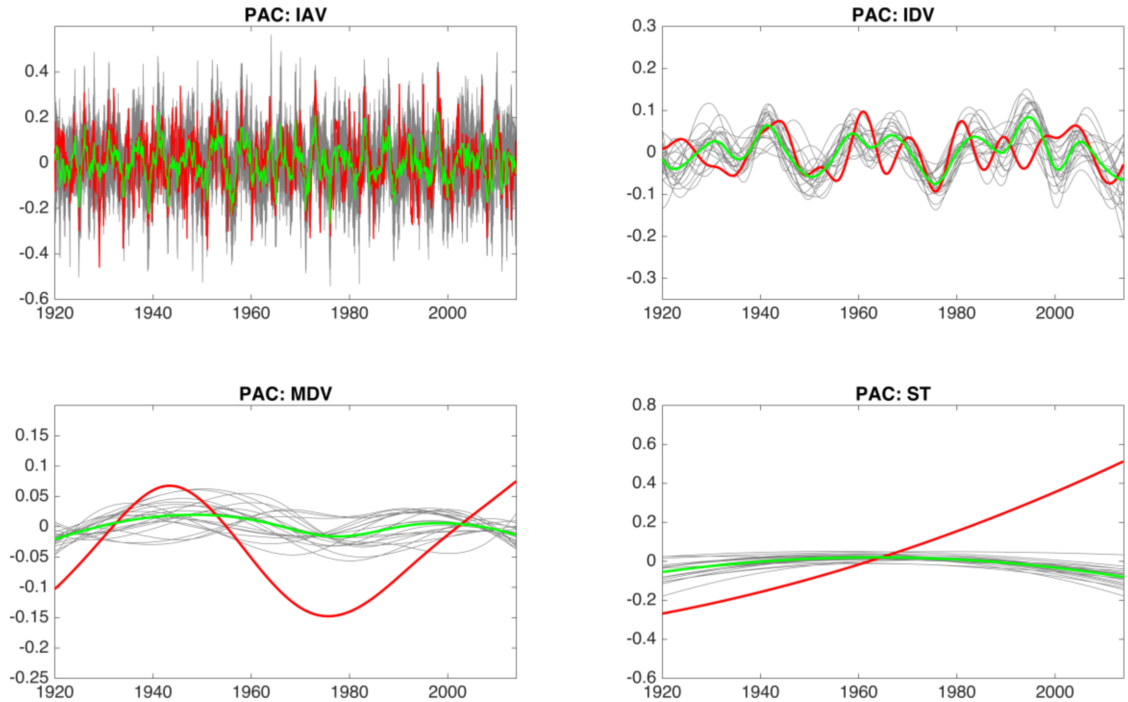

Figure 2.10. The four components (IAV, IDV, MDV and ST) of GST change over 1920-2013 forced by Pacific Pacemaker experiment. The gray lines are ensemble members. The green line is the ensemble mean of Pacific Pacemaker. The red line is the observed GST change estimated by HadCRUT4 data set.

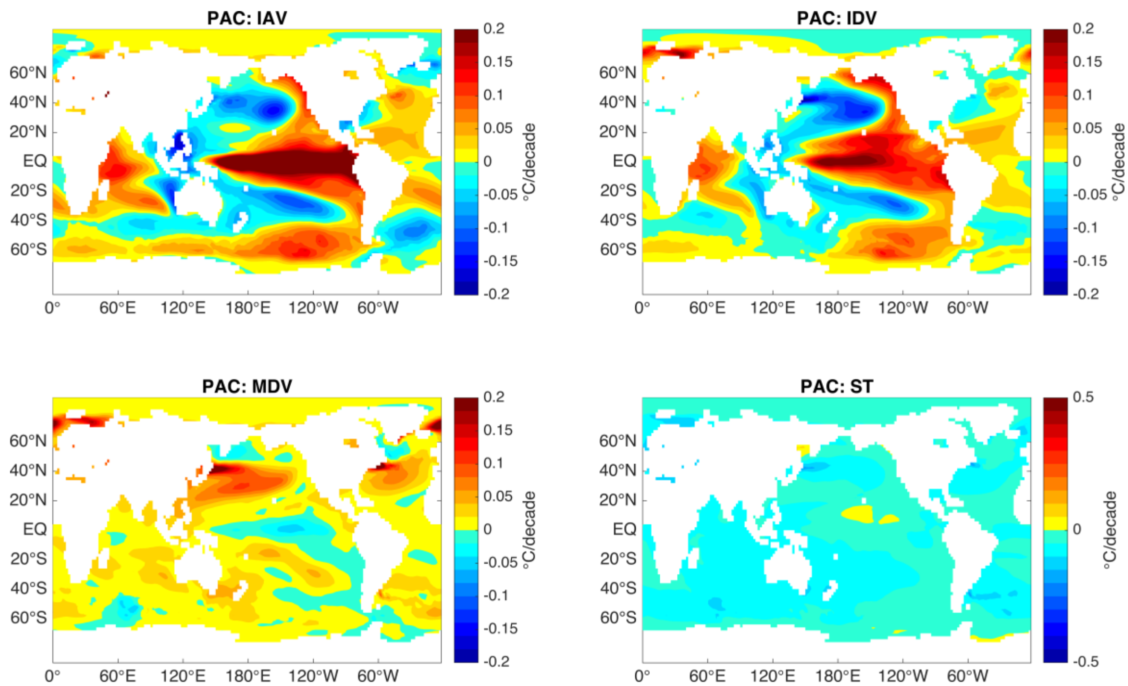

Figure 2.11. Regression of ERSST onto 4 components based on Pacific pacemaker (PAC) model experiment over 1920-2013. The 4 components have been normalized.

2.4.4 Atlantic Pacemaker model experiment

Previous studies also claim that the North Atlantic is the main driver of the GST change on multi-decadal time scales through AMO and AMOC. However, the previous study of Rodríguez et al., (2009) suggests that the Atlantic SST change enhanced the Pacific ENSO events through the atmospheric teleconnections. How much do observed North Atlantic SST changes contribute to the GST change, and on which time scale the Atlantic contribute more? To answer this question, we use the Atlantic Pacemaker model experiment (denoted as CESM-ATL) to identify the role of Atlantic forcing in GST change. Similarly, to get the pure Atlantic forcing, the CESM-LE ensemble mean is subtracted from each CESM-ATL ensemble member to removes the effect of external forcing. In contrast to the previous studies, the Atlantic forced MDV

Similarly, to get the pure Atlantic forcing, each of the CESM-ATL ensemble members is removed from the external forcing by subtracting the CESM-LE ensemble mean. Contrary to the previous studies, the Atlantic forced MDV (Figure 2.12, ATL-MDV, green line) shows very weak amplitude which can only explain 15% of the observed variance (Figure 2.12, ATL-MDV, red line), the same as the Pacific forced MDV (Figure 2.10, PAC-MDV, green line). Consistently, the CESM-ATL ensemble members have considerable diversity in their phases (Figure 2.12, ATL-MDV, gray lines). For instance, in the 1990s, some ensemble members exhibit a positive phase consistent with the observation, while other members show negative trends. The negative and positive phases would cancel out, leading to a small estimate of MDV by ensemble mean. Moreover, the Atlantic cannot capture the main features of the observed MDV spatial pattern, it only reproduced the warming in the North Atlantic and the North Pacific, suggesting that the Atlantic itself is not strong enough to control

MDV of GST change, in other words, the Atlantic forcing contributed less to the GST change in MDV time scale.

As opposed to MDV, at the inter-annual and inter-decadal time scale, CESM-ATL forced signals have a large contribution to the observed variance. The spatial patterns of the IAV and the IDV components forced by the Atlantic forcing are similar to those forced by the Pacific, except for a slight cooling in the Southern Ocean. Especially at inter-decadal time scales, the variance of IDV forced by Atlantic is 0.0015 accounting for 72% of the observed variance, implying the Atlantic forcing also contribute to GST change at inter-decadal times scales.

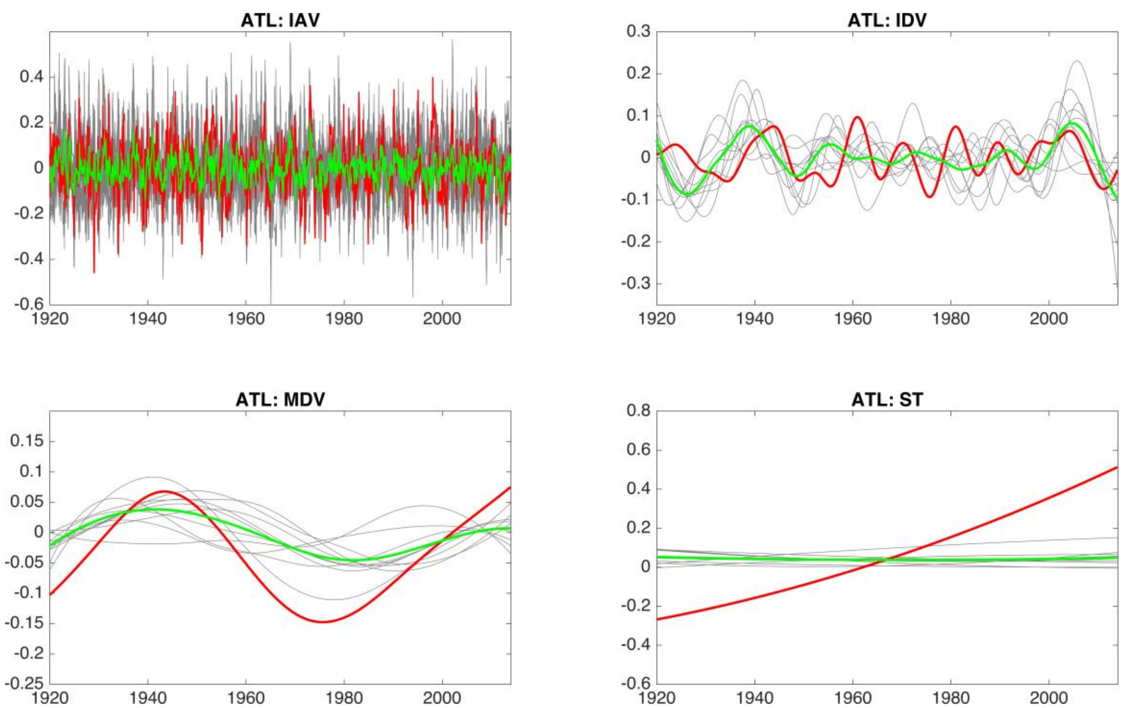

Figure 2.12. The four components (IAV, IDV, MDV and ST) of GST change over 1920-2013 forced by Atlantic Pacemaker experiment. The gray lines are ensemble members. The green line is the ensemble mean of Atlantic Pacemaker. The red line is the observed GST change estimated by HadCRUT4 data set.

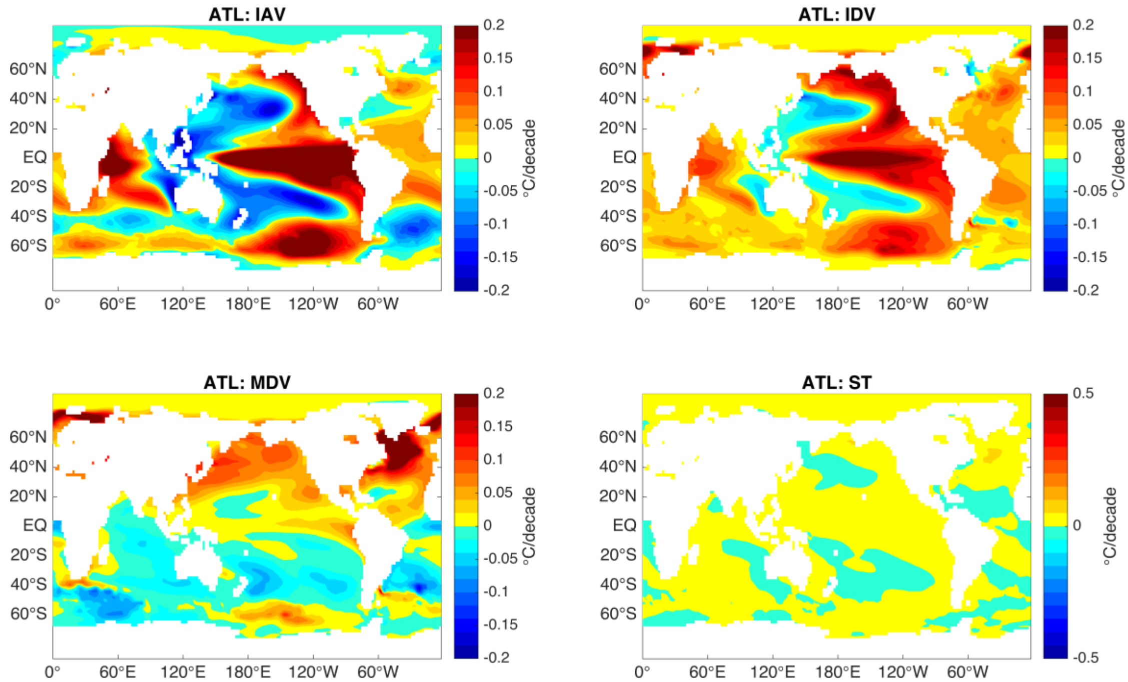

Figure 2.13. Regression of ERSST onto 4 components based on Atlantic pacemaker (ATL) model experiment over 1920-2013. The 4 components have been normalized.

2.5 Summary and Discussions

The GST variability since the industrial revolution has shown significant multi-scale characteristics. This study tried to address the respective roles of external forcing and internal climate modes to the GST variations on different timescales. The observed GST derived from Hadcrut4 data is decomposed into IAV, IDV, MDV and a secular trend using EEMD method. Their associated SST spatial patterns are obtained to get some indication of related physical dynamical processes. The high-frequency variabilities, including inter-annual variation (IAV) and inter-decadal variation (IDV), are ENSO-like signals mostly associated with the SST change in Pacific. The low-frequency MDV is an AMO like signal highly correlated with the AMO index and has connections with the Pacific and the Indian Ocean. The monotonous increasing secular trend and its worldwide warming spatial pattern are related to the anthropogenic greenhouse gases in the last twentieth century.

The decomposition of GST is indicative of the internal variabilities that prominently generated by Pacific and Atlantic and external variabilities caused by anthropogenic forcing are likely to be responsible for the variation of the GST. Thus, the role of the Pacific, the Atlantic and external forcing in modulating the observed GST over the historical period has been investigated using a series of climate model simulations. The Pacific Pacemaker model experiments show that the Pacific mainly contributes the GST variations at interannual and inter-decadal time scales through ENSO. The Atlantic also modulated the GST changes in inter-decadal time scales through the atmosphere teleconnection on the easter Pacific. The externally forced simulations from the majority of CESM-LE ensemble members can reproduce MDV changes that are significantly correlated with the observed MDV and can explain up to 86% of the observed variance, indicating the external forcing, especially the aerosol forcing, has a great contribution to control timing and phase of MDV in the GST change, while the forced signal by Atlantic forcing contribute very little to the MDV change as previous studies suggested. Furthermore, for the prolonged hiatus periods of ~30 years (1945-1975), the multi-decadal signal is dominant in driving the GST change, whereas the relatively shorter hiatus periods, such as the recent one over 1998-2014, are mainly caused by the inter-decadal signal.

This study took comprehensive approaches to understand derivers of the GST change in different time scales during the historical period since 1850. The results have important meaning in understanding how the external and internal climate variability contribute to the GST change in different time scales. Results are based on experiments from one climate model, the multiple model simulations from CMIP6 would help to better address this question.

Chapter 3

RECENT SHIFT IN THE WARMING OF THE SOUTHERN OCEANS MODULATED BY DECADAL CLIMATE VARIABILITY

3.1 Introduction

Nearly 90% of the excess heat received by the Earth due to anthropogenic warming is stored in the ocean (von Schuckmann et al., 2020), which leads to increases in the global ocean heat content (OHC) and sea-level rise. It has been shown that the Southern Ocean plays an important role in the global ocean heat uptake and storage due to its unique circulation patterns (Frölicher et al., 2015; Sallée, 2018). Over the past several decades, rapid and deep-reaching warming has been observed in the Southern Hemisphere extratropical ocean, especially at the middle latitudes between 35°S and 50°S (Gille, 2008; Cai et al., 2010), which can be primarily attributed to anthropogenic greenhouse gas forcing (Swart et al., 2018). Over the earlier period (2006–2013) of the Argo record, global ocean warming predominantly occurred in the Southern Hemisphere, with two hotspot regions in the southeast Indian Ocean and South Pacific Ocean (Roemmich et al., 2015; Llovel and Terray, 2016). The Southern Ocean has also been suggested to be one key region for downward heat transport into deeper layers during the temporary global surface warming slowdown earlier this century (Chen and Tung, 2014; Yan et al. 2016), although it is still unclear whether the observed Southern Ocean warming over this period is of anthropogenic or natural origin (Liu et al., 2016). Several studies have identified the southeast Indian Ocean as a hotspot region of upper-ocean warming during this global surface warming slowdown period, which was mainly contributed by the increased Indonesian Throughflow heat transport (Lee et al., 2015; Li et al., 2017; Zhang et al., 2018).

One important driver of the Southern Ocean warming is the strengthening and poleward shift of the Southern Hemisphere westerly winds (Swart and Fyfe, 2012), which is associated with a positive trend in the Southern Annular Mode (SAM; Marshall, 2003). Over the relatively short Argo period, a key process in the Southern Ocean warming is the wind-driven thickening of the Subantarctic Mode Water (SAMW) (Gao et al., 2018) due to the increased subduction rate (Qu et al., 2020). Changing winds also lead to the continuous spin-up of the Southern Hemisphere subtropical ocean gyres (Roemmich et al., 2016; Qu et al., 2019). However, despite the fact that the wind forcing can drive adiabatic warming signals and that the poleward displacement of the climatological temperature field can largely reproduce the observed multidecadal warming patterns (Gille, 2008), the net OHC increase in the Southern Ocean requires extra heat from the surface heat uptake (Cai et al., 2010; Swart et al., 2018). The surface heat and freshwater fluxes are also required for explaining the observed multidecadal changes in the Southern Ocean temperature and salinity on pressure or density surfaces (Böning et al., 2008; Meijers et al., 2011). It has been shown that the ocean warming patterns over the multidecadal historical period or the Argo period are mainly determined by the heat redistribution by the changing ocean circulation (Bronselaer and Zanna 2020; Zika et al. 2020). In contrast, numerical model experiments suggest that the projected future ocean warming is dominated by the redistribution of added heat at the ocean surface (Liu et al. 2018; Dias et al. 2020).

In this study, based on updated observations until 2019, we find that the previously reported rapid warming in the Southern Hemisphere extratropical ocean during the earlier period of the Argo record (2006–2013) or the global surface warming slowdown period (2003–2012) has slowed down afterward and was even changed to cooling in certain regions due to a phase shift in the SAM and Interdecadal Pacific Oscillation (IPO). We further decompose observed subsurface ocean temperature and salinity changes into changes along isopycnals (known as spiciness) and changes resulting from the displacements of isopycnals (known as heave) to understand mechanisms and drivers for the Southern Ocean warming and its recent shift (Bindoff and McDougall, 1994).

3.2 Data and Method

Our analysis is mainly based on the objectively analyzed EN4 dataset over 1960–2019 (Good et al., 2013). Another objectively analyzed ocean dataset (Ishii et al., 2017) and an Argo-based gridded product (Argo, 2000; Roemmich and Gilson, 2009) are also used for inter-comparison. Monthly anomalies of the ocean potential temperature and salinity were derived by subtracting the calculated monthly climatology over the Argo period 2006–2019. The OHC anomalies at each grid point were calculated as the vertical integration of the potential temperature anomalies multiplied by the constant density (1035 kg/m^3) and specific heat capacity (3985 J/K/kg). We also use surface wind stress from the Japanese 55-year reanalysis (JRA-55; Kobayashi et al., 2015).

The observed potential temperature and salinity anomalies at the depth levels ($\theta'|_z$ and $S'|_z$) at each grid point can be decomposed into spiciness and heave components as follows:

$$\theta'|_z = \theta'|_n + N'\theta_z, S'|_z = S'|_n + N'S_z, \quad (1)$$

in where $\theta'|_n$ and $S'|_n$ are density-compensating spiciness anomalies along the neutral density surfaces (Jacket and McDougall, 1997), N' is the neutral density surface height change (downward is positive), and θ_z and S_z are the vertical gradients of the potential temperature and salinity. The residuals can be obtained as the differences between the observed anomalies on the left-hand side of Eq. (1) and the sum of the two components on the right-hand side of Eq. (1). In consistency with previous studies (Köhl, 2014; Desbruyères et al., 2017), the residuals are relatively small except for in the upper mixed layer.

Such decompositions have been widely applied in observational data and model simulations to understand which processes determine the regional changes in the ocean temperature and salinity properties (Bindoff and McDougall, 1994; Durack and Wijffels, 2010; Köhl, 2014; Häkkinen et al., 2016; Desbruyères et al., 2017; Zhang and Yan, 2017; Clément et al., 2020; Lyu et al., 2020). The spiciness is expected to reflect the changes in the water mass properties due to the subduction of the surface anomalies primarily modified by air-sea fluxes, while the heave component arises from both dynamically induced adiabatic heave of isopycnals and also diabatic processes such as the downward diffusion and subduction of heat (Häkkinen et al., 2016). The analyzed changes over the global surface warming slowdown period 2003–2012 are likely biased in the historically under-sampled regions due to the transition to increased sampling by the Argo floats in around 2005/2006 (Clément et al., 2020).

3.3 Decadal Warming Shift and Large-scale Climate Drivers

The upper-2000m OHC changes are examined over four time periods: the temporary global surface warming slowdown period 2003–2012, the earlier period of the Argo record 2006–2013 as used in the study of Roemmich et al. (2015), the recent period 2013–2019, and the multidecadal historical period 1960–2019 (Figure 3.1). Similar OHC changes over these periods can be found with the Ishii dataset (Figure B 1). The upper-700m OHC gives virtually the same patterns with slightly smaller magnitudes (Figure B.2). The Argo-only product also confirms the robustness of observed changes over the earlier (2006–2013) and later (2013–2019) periods of the Argo record (Figure B.3). Throughout this study, a change refers to a linear trend estimated over a given period unless otherwise stated.

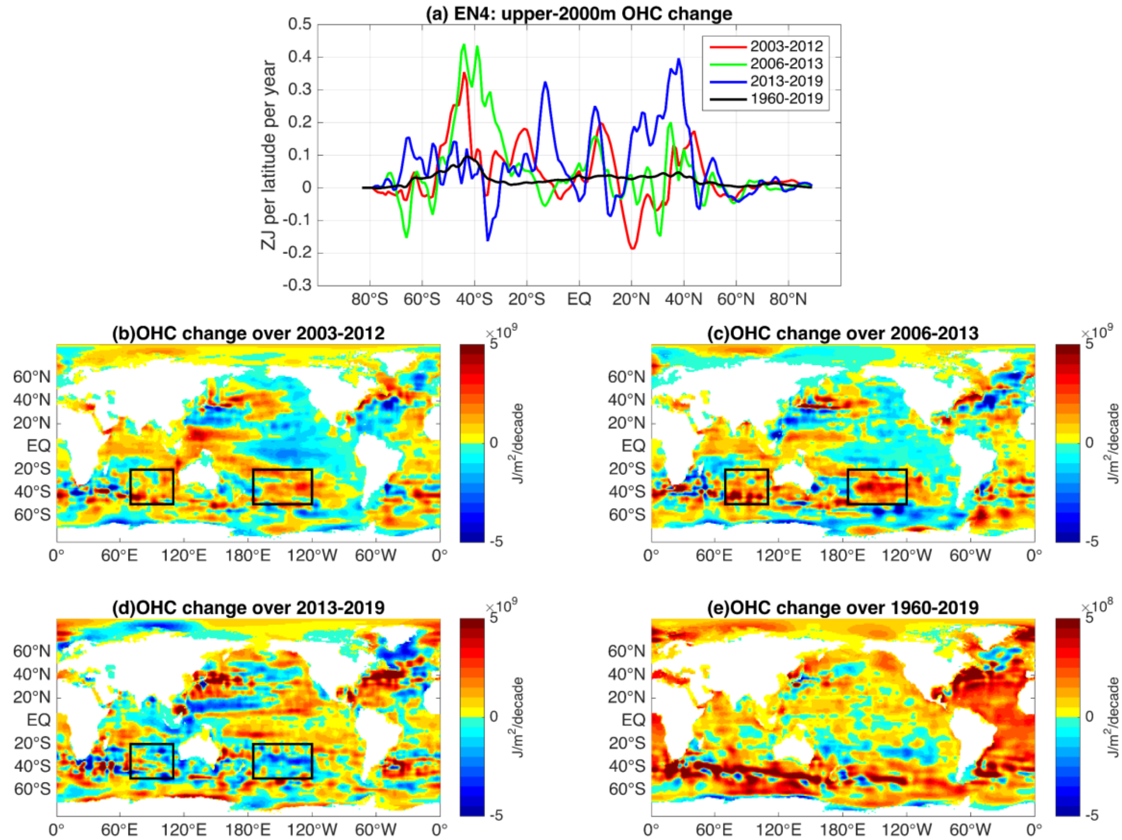

Figure 3.1. The Upper-2000m depth-integrated OHC changes calculated from the EN4 data. (a) Global zonal integrated OHC changes (ZJ per degree latitude per year) over 2003–2012 (red line), 2006–2013 (green line), 2013–2019 (blue line), and 1960–2019 (black line). (b)-(e) Spatial patterns of the OHC changes (J/m^2/decade) over 2003–2012, 2013–2019, 2006–2013, and 1960–2019, respectively. The black boxes in (b)-(d) indicate the two studying regions in the SEIO (70°–110°E, 20°–50°S) and SPAC (185°–240°E, 20°–50°S). Note the range on the color bar in panel (e) is one order of magnitude smaller than in panels (b)-(d).

The maximum ocean heat storage occurred in the Southern Hemisphere mid-latitude band at around 40°S over both 2003–2012 and 2006–2013, which was largely reduced over 2013–2019 (Figure 3.1a). Meanwhile, the Northern Hemisphere extratropical oceans experienced increased heat storage. The ratio of the Southern

Hemisphere OHC increase to the global OHC increase decreased from 81% over the earlier Argo period 2006–2013 to 43% over the later Argo period 2013–2019 and 65% over the entire Argo period 2006–2019. Very similar ratios can be obtained from the Ishii dataset (81%, 44%, 66% over the same periods). The Argo-only product also shows that the Southern Hemisphere oceans account for 34% (64%) of the global OHC increase over 2013–2019 (2006–2019), which is in clear contrast to its predominant contribution over the earlier period 2006–2013. The extended Argo record suggests that the large hemispheric asymmetry in global ocean warming derived from the earlier relatively short Argo record is mainly due to the natural climate variability, a conclusion also supported by climate model simulations (Irving et al., 2019; Rathore et al., 2020).

The OHC change patterns show two centers of maximum OHC increase located in the southeast Indian Ocean (SEIO) and South Pacific Ocean (SPAC) over both 2003–2012 and 2006–2013 (Figure 3.1b and 3.1c). In contrast, the OHC in these two regions decreased over the recent period 2013–2019 (Figure 3.1d). The upper-2000m OHC time series integrated over the SEIO (70°–110°E, 20°–50°S) and SPAC (185°–240°E, 20°–50°S), the same domains as used in the study of Llovel and Terray (2016), indeed show that the rapid warming since earlier this century has stopped or even changed to a cooling trend roughly after 2013 (Figure 3.2a and 3.2b). The OHC time series in these two regions also exhibit considerable interannual variations. A recent study by Volkov et al. (2020) highlighted an unprecedented drop in the OHC and sea level in the SEIO during the 2015/16 strong El Niño and a quick recovery afterward during the 2017/18 weak La Niña, as also seen in our analysis (Figure 3.2a).

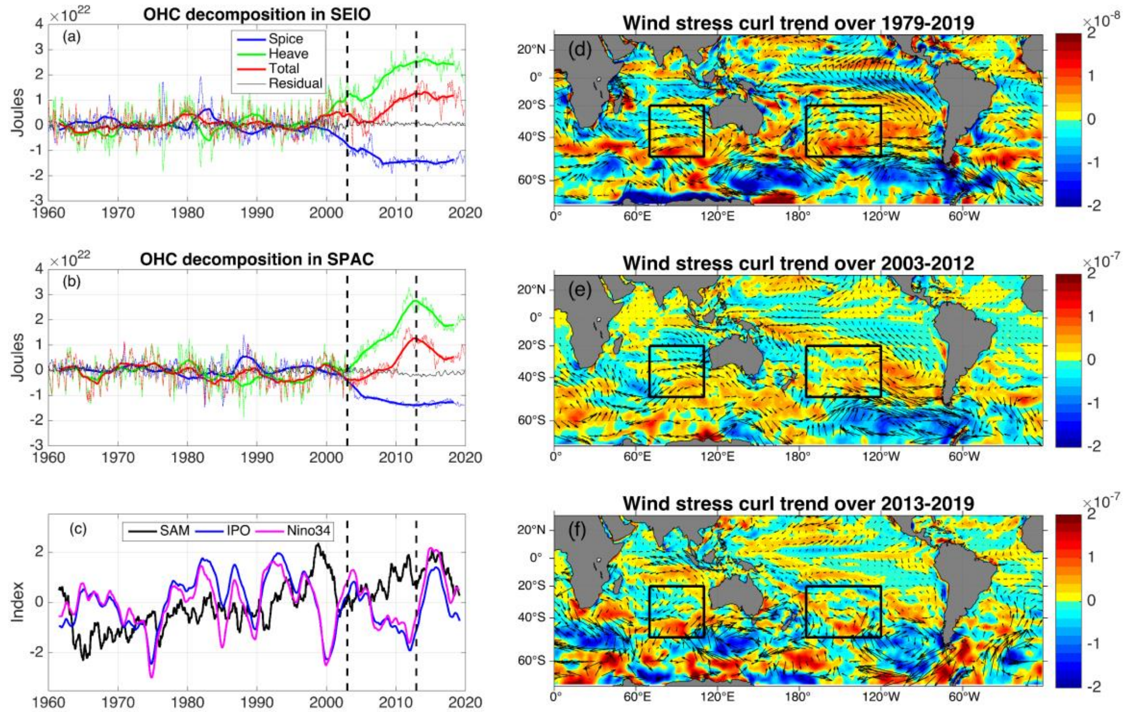

Figure 3.2. Upper-2000m depth-integrated OHC changes in the (a) SEIO and (b) SPAC regions over 1960–2019. The dashed red, green, blue, and black lines are the monthly OHC anomalies relative to 1960–1980 along with their heave, spice, and residual components, respectively, and the bold lines denote the smoothed time series after the 37-month running mean. (c) Smoothed SAM (black), IPO (blue), and Niño 3.4 (pink) indices after the 37-month running mean over 1960–2019 with the two vertical dashed black lines marking the 2003–2012 period. (d)-(f) Changes in the surface wind stress (vectors, N/m^2/decade) and wind stress curl (shading, N/m^3/decade) calculated from the JRA-55 reanalysis data over 1979–2019, 2003–2012, and 2013–2019, respectively. The Mercator projection is used in (d-f), with the black boxes indicating the two studying regions in the SEIO (70°–110°E, 20°–50°S) and SPAC (185°–240°E, 20°–50°S). Note the range on the color bar in panel (d) is one order of magnitude smaller than in panels (e) and (f).

We then identify the large-scale climate drivers that might be responsible for this recent shift (Figure 3.2c). As the leading mode of climate variability in the extratropical Southern Hemisphere, the SAM has been showing an upward trend in the past several decades (0.5 hPa per decade over 1960–2019 based on annual SAM index), accompanied by westerly wind anomalies poleward of 40°S (Figure 3.2d) and the enhanced warming in the Southern Ocean (Figure 3.1e). Stronger westerly wind anomalies can be found especially over the southeast Pacific Ocean over 2003–2012 (Figure 3.2e) when the SAM had a larger upward trend (1.7 hPa per decade). However, as the long-term upward trend in the SAM has become slower in the past decade or so (-2.3 hPa per decade over 2013–2019), easterly wind anomalies have prevailed over the high-latitude Southern Hemisphere (Figure 3.2f). Therefore, it seems that this recent shift in the Southern Ocean warming coincided with a decadal variation in the SAM.

The OHC (Figure 3.1b and 3.1d) and surface wind (Figure 3.2e and 3.2f) changes over 2003–2012 and 2013–2019 largely resemble the sea level and wind patterns associated with the Pacific decadal variability (Lyu et al., 2017). Indeed, the large declining trend in the IPO index (Henley et al., 2015) over 2003–2012, which is a key driver of the global surface warming slowdown over this period (England et al., 2014), has changed to a rising trend afterward (Figure 3.2c). Although another declining tendency seemed to appear after the 2015/16 strong El Niño, continuous monitoring is needed to see whether it is an interannual signal or another decadal shift toward the opposite phase.

The Niño 3.4 index exhibited very similar variations as those of the IPO index. A cooling trend in the Niño 3.4 index over 2003–2012 was accompanied by intensified easterly trade winds over the tropical Pacific (Figure 3.2e), heat accumulation in the western tropical Pacific, and enhanced warming in the SEIO through the increased ITF transport (Figure 3.1b). Gastineau et al. (2019) conducted a partially coupled experiment to show that such La Niña-like change in the tropical Pacific could also contribute to the observed westerly (easterly) wind anomalies over the South Pacific (South Indian Ocean) through atmospheric teleconnections (Figure 3.2e). These changes were weakened or reversed to their opposite signs over 2013–2019 with the rising of the Niño 3.4 index. Some recent studies have also pointed out the important contribution of tropical teleconnections to the mixed-layer variability and SAMW formation in the Southern Ocean (Meijers et al., 2019; Li and England, 2020). Therefore, the recent shift in the Southern Ocean warming is also in phase with the Pacific basin-wide decadal climate variability (i.e., IPO), with possible remote forcing from the tropical Pacific.

3.4 Mechanisms: Heave and Spice Analysis

In the last section, we examined the co-variations between the OHC, winds, and the major climate variability modes during this recent shift in the Southern Ocean warming. Here, we further explore mechanisms regarding how these large-scale climate modes drive the observed changes in the ocean. We first start with the SPAC region. The multidecadal warming over 1960–2019 mainly occurred in the upper 400 m and extended deeper south of 35°S (Figure 3.3a), which was strengthened over 2003–2012 (Figure 3.3b) but reversed to cooling over 2013–2019 (Figure 3.3c).

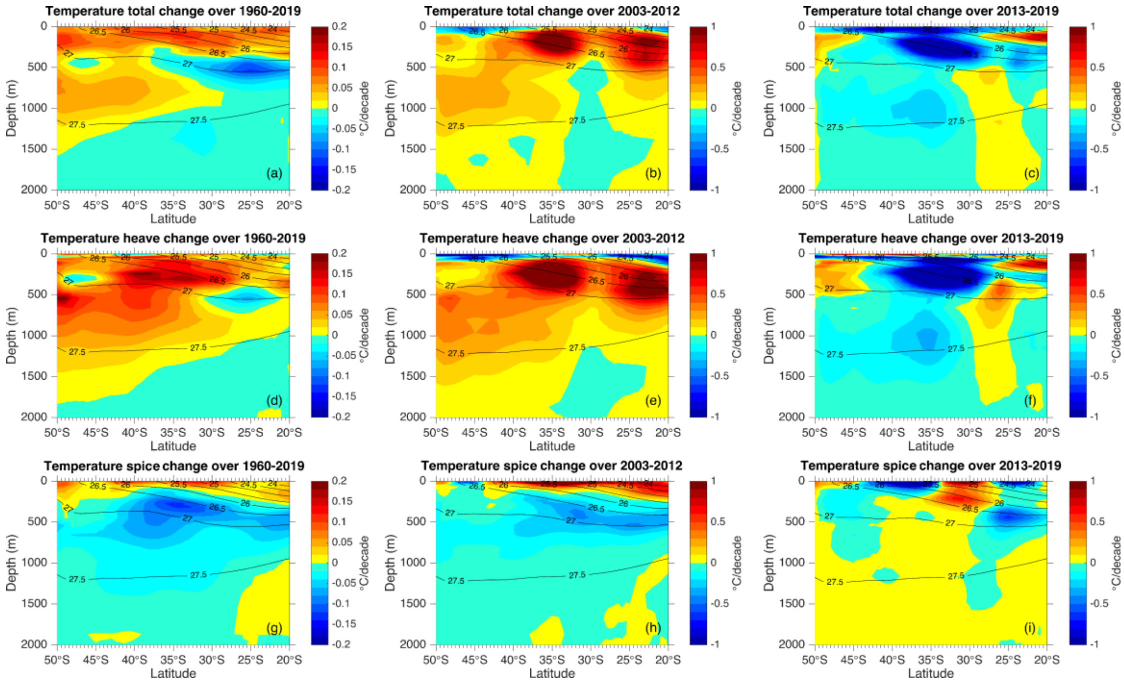

Figure 3.3. Zonal averages of the changes in the potential temperature, heave, and spice components (°C/decade) in the SPAC region over (left panels) 1960–2019, (middle panels) 2003–2012, and (right panels) 2013–2019. The mean density surfaces over each period are superimposed as contours. Note the left panels use smaller range on the color bars than the middle and right panels.

Changes in the heave component dominate the observed ocean temperature changes over these three periods (Figure 3.3d-f) and the OHC time evolutions (Figure 3.2a and 3.2b). The heave-related temperature changes are due to the deepening of isopycnals up to 10 (60) m/decade between 26.5–27.5 kg/m^3 over 1960–2019 (2003–2012) and their shoaling over 2013–2019 (Figure 3.4a). Over 1960–2019 and 2003–2012, the downward displacements of isopycnals particularly between 35°S–50°S (Figure B4) are likely driven by positive wind stress curl anomalies at similar latitudes (Figure 3.2d and 3.2e) through the enhanced wind-driven Ekman transport convergence and resultant downward Ekman pumping (Roemmich et al., 2016). Over 2013–2019, the upward displacements of isopycnals seem to be inconsistent with the local wind stress curl anomalies but could be explained by a spin-down of the subtropical gyre as the westerly winds displaced equatorward associated with a declining trend in the SAM over this period (Qu et al. 2019). The deepening (shoaling) of isopycnals also led to saltier (fresher) changes mainly between 100–500m above the salinity minimum of the Antarctic Intermediate Water (AAIW) (Figure B.5).

The spice component plays a second role by partially offsetting the heave component contribution (Figure 3.2a and 3.2b; Figure 3.4b and 3.4c). The multidecadal spice changes over 1960–2019 show cooling and freshening below warming and salinization in the upper 100–200 m (Figure 3.3g). These subsurface cooling and freshening spice changes occurred over wide depth and density ranges, reaching maximum on the density surfaces within the SAMW (26.5–27.1 kg/m^3; Gao et al., 2018) and extending deeper into the AAIW. These observed cooling and freshening spice changes on the density surfaces within the SAMW and AAIW have been widely reported (Bindoff and Church, 1992; Aoki et al., 2005; Durack and Wijffels, 2010; Helm et al., 2010) and reproduced in climate model simulations (Banks and Bindoff, 2003; Lyu et al., 2020; Silvy et al. 2020). The spice changes over 2003–2012 show very similar patterns to the multidecadal changes but with much larger magnitudes (Figure 3.3g and 3.3h), while the spice changes over 2013–2019 have less coherent patterns (Figure 3.3i). The spatial patterns of the spice changes along 26.75 kg/m^3, which is roughly the average density of the SAMW, generally show cooling and freshening over 1960–2019 and 2003–2012 but warming and salinization over 2013–2019 (Figure B.6).

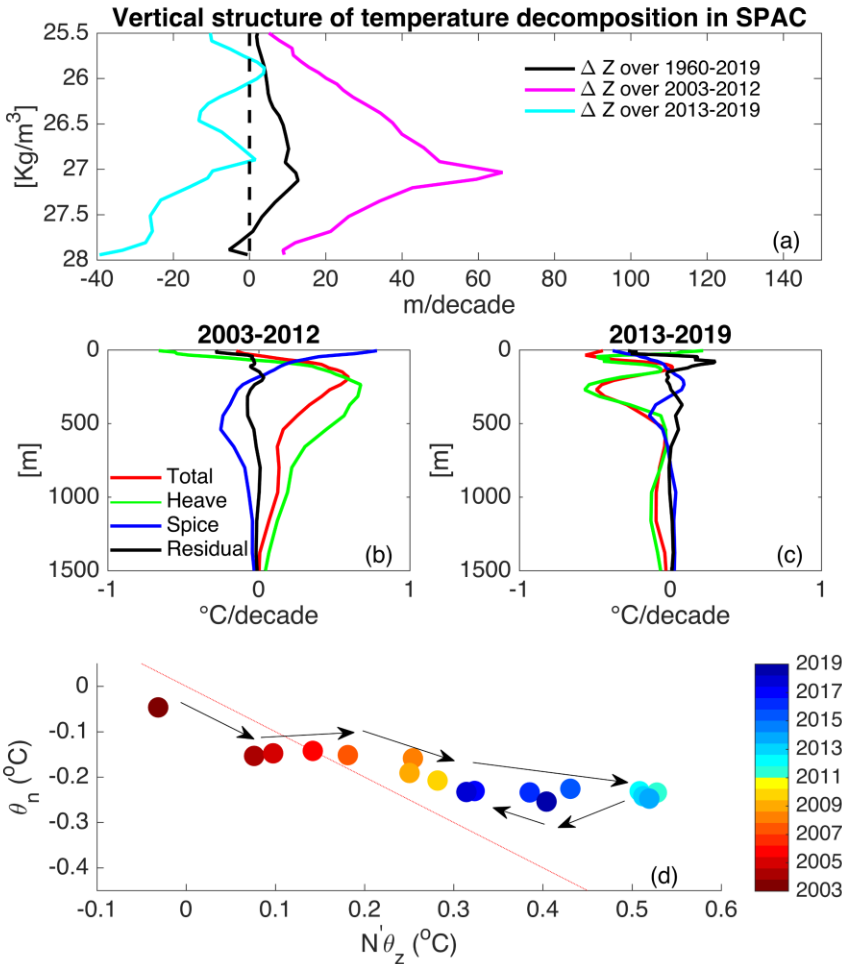

Figure 3.4. (a) Vertical displacement (m/decade) of the density surfaces in the SPAC region over 1960–2019 (black line), 2003–2012 (pink line), and 2013–2019 (cyan line). (b) Vertical profiles of the temperature changes (red line) along with the heave (green line), spice (blue line), and residual (black line) components over 2003–2012 in the SPAC region. (c) Similar as in (b) but for changes over 2013–2019. (d) Hodograph of the heave and spice components of the 200–700m annual temperature anomalies relative to 1960–1980 in the SPAC region. The red dashed line indicates the zero temperature anomalies, as the heave and spice components cancel each other out. The colors of circles and the arrows illustrate the time evolution from 2003 to 2019.

Following Bindoff and McDougall (1994), we use a hodograph to illustrate the relationship between the heave and spice changes averaged over 200–700m (Figure 3.4d). The upper-200m was excluded due to the large residuals for the heave and spice decomposition (Figure 4b and 4c). From 2003 to 2012, the heave-related temperature anomalies increased by more than 0.5°C, while the spice anomalies decreased by ~0.2°C. The wind forcing could explain the changes due to the heave of the isopycnals but not the spice changes, which are likely indicative of the subduction of warming and freshening anomalies due to the heat and freshwater input at sea surface (Bindoff and McDougall, 1994). These spice changes are consistent with the increased surface heat fluxes into the Southern Ocean over 2003–2012 (Queste et al., 2020). The observed changes over 2003–2012 might be understood as a combination of the idealized "pure warming" and "pure heave" processes proposed by Bindoff and McDougall (1994). The pure warming process was defined to represent the subduction of the surface warming signal which induces both the heave of isopycnals and spice changes, while the pure heave process was defined as no spice change to represent the adiabatic heave of isopycnals. From 2013 to 2019, the heave-related temperature anomalies decreased by ~0.2°C, but the spice anomalies had little change over this period, although the spice changes might still be large locally at certain depth levels (Figure 3i). These changes could be explained solely by the wind forcing without surface heat and freshwater flux changes and thus might be approximated as the idealized pure heave process. In fact, the surface heat fluxes into the Southern Ocean had a slightly declining trend since 2013 although they rebounded again in 2019 (Queste et al., 2020).

The temperature and salinity changes in the SEIO show similar large-scale features, similar contrasts between these three periods, and similar relationships between the heave and spice components, as in the SPAC. However, some details still differ (Figure B.7-B.11). Compared with the warming in the SPAC (Figure 3.3a and 3.3b), the maximum and deep-reaching warming in the SEIO are stronger and confined to a narrower band between 40°S–45°S (Figure B.7a and B.7b). Another unique feature of the SEIO is the downstream effect of the ITF which could dominate over the local wind forcing. The northern part of the SEIO along the western Australia became warmer (Figure B.7b) and fresher (Figure B.9b) in the upper 200m over 2003–2012 mainly due to the increased ITF transport (Makarim et al., 2019), which was then changed to a cooler (Figure B.7c) and saltier (Figure B.9c) trend over 2013–2019.

3.5 Summary and Discussion

In this study, we have shown that the rapid warming in the Southern Hemisphere extratropical ocean has slowed down and reversed to a cooling trend in the SEIO and SPAC over 2013–2019. When estimated over the entire available Argo period 2006–2019, the contribution of the Southern Hemisphere ocean to the global ocean heat storage is ~65%, which is lower than the previous estimates over the earlier Argo period, e.g., 90% over 2005–2014 (Llovel and Terray, 2016). This recent shift is modulated by decadal variations in the SAM and IPO, with a possible contribution from tropical Pacific teleconnections.

We further explored the mechanisms for this decadal shift by decomposing the subsurface ocean temperature and salinity changes into heave and spice components. The subsurface ocean warming (cooling) structures over the earlier (later) period were largely determined by the deepening (shoaling) of isopycnals in response to changing winds. The earlier rapid warming period was also featured by an enhancement of the multidecadal spice change patterns, especially in regarding to the cooling and freshening changes along the isopycnals within the SAMW and AAIW, which are likely signatures of the surface buoyancy forcing. Note that the salinity change patterns were instead dominated by the spice component (Figure B.5 and B.9), suggesting that the temperature and salinity changes are determined by different dynamical processes, which requires further investigation.

It is important to note that the global OHC is still increasing as a strong indication of the ongoing global warming (Johnson et al., 2020). The recent shift in the Southern Ocean warming is only one example among many others that illustrate that the observed changes over a relatively short period are dominated by natural decadal variability, which can temporally enhance or weaken the long-term climate change signal (Johnson and Lyman, 2020). An improved understanding of the natural decadal variability and extended observational record are needed to better detect the climate change signal from observations, which in turn might be useful for constraining future changes. Meanwhile, it is critical to examine whether the current decadal prediction systems initialized with recent reliable and extensive observations can forecast this decadal shift and its climate impacts.

Chapter 4

EARLY 21st CENTURY RAPID WARMING IN THE SOUTHERN OCEAN ENHANCED BY TROPICAL PACIFIC FORCING

4.1 Introduction

Oceans have an important impact on the Earth's Energy imbalance due to its great capacities for heat storage (Rhein et al., 2013). As the connector with the Pacific, the Atlantic and the Indian Ocean, the Southern Ocean plays a critical role in transporting surface heat to the deep oceans. Observations reveal that the Southern Ocean exhibits pronounced warming during the past decades (Durack et al., 2014; Roemmich et al., 2015). Since 2006, most of the heat gain (60%–90%) is stored in the subsurface of the Southern Hemisphere oceans (Roemmich et al., 2015).

The model simulation suggests that the heat exchange between the surface and subsurface of oceans is mostly controlled by the Southern Ocean through the Ekman pumping by the changing westerly wind stress in the mid-latitude of Southern Hemisphere (Gregory, 2000). In the interior of the Southern Ocean, two primary processes could be important in balancing the heat transport (Morrison et al., 2016). One is through southward and upward eddy processes (Gregory, 2000). The other is the northward and downward advections by the mean flow (Marshall and Zanna, 2014). The heat balance is not only determined by the transportation along isopycnals, as both the mean flow and the eddy transport can cause heat redistribution in the subsurface of the Southern Ocean. The wind stress changes due to anthropogenic forcing has a great impact on the Southern Ocean circulation system (Gillett and Thompson, 2003). Some studies have emphasized that the increased greenhouses gases and ozone depletion result in the recent strengthening of westerly wind and with a positive phase of the southern annular mode (SAM) (Swart and Fyfe, 2012; Gillett and Thompson, 2003; Fyfe and Saenko, 2006). As the leading atmospheric climate variability in the Southern Ocean, the SAM has been shown to be related to different sources of external forcing. Observations over 1969-1998 provide the evidence that the positive SAM trend since the 1960s is associated with increasing stratospheric ozone depletion (Thompson and Solomon, 2002). A similar study by Arblaster and Meehl (2006) further indicates that various external forcings, including the polar troposphere and stratosphere ozone changes, contribute the upward trend of SAM. The contributions of internal variability sourced from the Pacific have also been investigated. Previous studies have linked the negative phase of IPO to the Antarctic sea ice expansion (Meehl et al., 2016a, 2019). Although many studies have addressed and explained the processes of southern oceans warming and their regional distribution, the underlying physical mechanisms related to wind stress, eddies, and tropical Pacific teleconnection have rarely been studied directly.

The aim of this work is to examine how the external forcing and the atmospheric circulation changes forced by the eastern equatorial Pacific SSTs influence the mid-latitude of Southern Ocean warming. Here, we use two sets of model experiments obtained from the CESM Large Ensemble project. The first experiments model experiment is simulated with all radiative forcings, such as the greenhouse gases, aerosols and other radiative forcing. While in the second experiment, the impact from the tropical variability is added in the model simulations by nudging the observed SSTs in the eastern equatorial Pacific. The rest of this chapter, the two coupled model experiments, observational datasets, and analysis method is described in section 4.2. The global OHC time series and spatial patterns are analyzed in section 4.3. The contributions of anthropogenic external forcing and internal climate variability from the Pacific to the South Pacific Ocean (SPAC) and Southeast Indian Ocean (SEIO) are assessed in section 4.4. Section 4.5 discusses the physical mechanisms that influence the two hotspots. A summary and discussion are provided in section 4.6.

4.2 Model, Data and Method

4.2.1 Coupled climate model experiments

In this chapter, the CESM Large Ensemble project is still used to examine the role of external forcing and the Pacific forcing in the Southern Ocean warming. This coupled climate model project is an open data set that has been widely used in climate studies to have an advanced understanding of internal climate variability and the climate change. As descripted in Chapter two, the CESM1(CAM2) is coupled with ocean, land, atmosphere and sea ice models and performed with 1° horizontal resolution in all model simulations (Kay et al., 2015). Here, two major model simulations from CESM version 1.1 experiments are analyzed, details can be found in Table 4.1.

The first experiment is the CESM Large Ensemble, hereafter "CESM-LE", a 40-member model experiment used to evaluate the impacts of external forcing on the heat gain in Southern Ocean. In this model experiment, each ensemble member is initialized with an identical historical radiative forcing, except for the slightly different atmospheric conditions at the beginning of the simulation. The small difference in the initial atmospheric state brings spreading among the ensemble members but can be cancelled out by averaging all ensemble members. Therefore, the mean of all CESM-LE ensemble members is used to quantify the external forcing's contribution to the heat redistribution.

The second experiment is CESM Pacific Pacemaker, hereafter "CESM-PAC". This experiment has 20 members. In addition to radiative forcing, the observed SSTs in the central to eastern Pacific (15°N–15°S; 80°–180°W) are also initialed in the model simulations, leaving the rest of the model free to evolve. The same as Kosaka and Xie (2013), the observed SSTs is obtained from the Version 3b (v3b) of the Extended Reconstruction SST dataset (Smith et al., 2008) and performs as initialized heat input in the ocean model part. This 20-members of Pacific pacemaker is using the internal variability sourced from the eastern tropical Pacific sets the pace and leaving all other oceans free to response. The model simulations start from 1920 to 2013.

All CESM-LE and CESM-PAC ensemble members are initialized with the same external forcing, using the observed historical radiative forcing (greenhouse gases, ozone concentrations, etc.) for 1920–2005 and the RCP 8.5 forcing for 2006–2013. The only difference is that the CESM-LE uses ozone concentrations produced by the whole atmosphere community climate model (WACCM; Marsh et al., 2013), while the CESM-PAC ensemble uses the ozone depletion data from the SPARC dataset (Cionni et al., 2011), which is widely used in the CESM CMIP5 models. The difference between SPARC ozone and WACCM ozone forced simulations is minimal and can be neglected (Schneider et al., 2015).

Table 4.1 Summary of the CESM large ensemble experiments

Experiments	*Model input*	*Ensemble members*
CESM-LE	All historical radiative forcings	40
CESM-PAC (Pacific Pacemaker)	All histrocial radiative forcings, + intrinsic variability+ Observed eastern Pacific SST anomalies (15°N-15°S; 80°-180°W)	20

4.2.2 Observational datasets

To estimate the Ocean heat content (OHC) changes in the Southern Hemisphere Oceans, subsurface ocean temperature obtained from objectively analyzed subsurface temperature fields from the ENACT/ENSEMBLES version 4 (EN4) (Good et al., 2013), the Ishii data (Ishii et al., 2017), the Institute of Atmospheric Physics (IAP) temperature data (Cheng et al., 2017), and the data from Levitus et al. (2010) are used together with the Argo based gridded product JAMSTEC for inter-comparison among observations.

The EN4 dataset version EN.4.2.1 is monthly mean potential temperature at 42 levels extending to beyond 5,000m from 1900 to the present, can be obtained from the Met Office Hadley Centre at https://www.metoffice.gov.uk/hadobs/en4/download-en4-2-1.html

The Ishii data is monthly mean temperature at 26 levels with depth in 2,000m, starting from 1960 to 2019, which is available from the Japan Meteorological Agency https://www.data.jma.go.jp/gmd/kaiyou/english/ohc/ohc_global_en.html

The IAP data is monthly mean temperature in the upper 2,000m from 1940 to present, available at ftp://ds1.iap.ac.cn/ftp/cheng/CZ16_v3_IAP_Temperature_gridded_1month_netcdf/

The Levitus data is annual temperature at 26 levels in the upper 2,000m during 1960–2019, which can be found at https://iridl.ldeo.columbia.edu/SOURCES/.LEVITUS/.MONTHLY/?Set-Language=en

The Japan Agency for Marine-Earth Science and Technology (JAMSTEC) data is an Argo data can be found at ftp://ftp2.jamstec.go.jp/pub/argo/MOAA_GPV/Glb_PRS/OI/.

4.2.3 Method

The ensemble mean removes the internal variability that beyond the forced ocean and retains the forced response. In the CESM-LE experiment, the forced response is from the external forcing, while the internal variability beyond the forced response is the slight difference of atmospheric state among each ensemble member at the beginning of the simulation. Therefore, the ensemble mean of the CESM-LE experiment (denoted “CESM-EM”) is used to identify the external forcing. Model simulation from individual ensemble members of the Pacific Pacemaker contains the external forced response, the interval variability from the eastern tropical Pacific forced response, and the response beyond the Pacific. Thus, the mean of Pacific Pacemaker ensemble (denoted “PACE-EM”) includes both the external forced responses and the internal variability responses from the tropical Pacific. In order to extract pure Pacific forced response, each ensemble member of the Pacific Pacemaker experiment is firstly removed the external forced response from the CESM-EM, and then processed with ensemble mean. Here, the responses to the tropical Pacific SSTs and the external forcing are assumed linear additive. It is may not strictly in theory, but it is the best way to separate the external forced response and the Pacific forced response as the SST change in tropical Pacific may also be influenced by the external forcing. The OHC spatial pattern is calculated based on the ensemble mean and can be understood as the model's response to the external forcing. The ensemble mean of CESM-PAC is interpreted as the estimate of model's response to the observed SST variations in tropical eastern Pacific.

Here, the Empirical Orthogonal Functions (EOF) analysis method is applied to identify the dominant spatial pattern of OHC variability. The details of EOF method can be found in the study of Chen and Tung (2014, 2018).

Table 4.2 Summary of forced responses

Response	*How derived*
Radiatively forced response	CESM-EM: mean of CESM-LE ensemble members
Tropical Pacific forced response	PACE-EM: mean of (individual CESM-PAC ensemble members minus CESM-EM)

4.3 Global OHC estimates

4.3.1 Global OHC time series

Figure 4.1 and Figure 4.2 display the time evolution and trends of global OHC at different depth ranges (upper 700m and upper 2000m). Here, the OHC integrated into 700/2000 m is denoted as OHC700/OHC2000. The observational data sets used here include the EN4, IAP and Levitus data sets. The analysis of OHC2000 excludes the result from Levitus data due to a lack of data at depths exceeding 700m until the year 2005. The observed evolution of OHC700 is dominated by an evident warming trend starting around 1970, with two distinct cooling phases in the mid-1980s and in the mid-1990s, and an accelerating increase during 2003-2012 at a rate of about 2.9x1022 J per decade (Chen and Tung, 2014; Trenberth et al., 2014). These two cooling episodes are attributed to the two largest volcanic eruptions of El Chichón in 1982 and eruptions of Mount Pinatubo in 1991 (Trenberth and Dai, 2007). Volcano eruptions increased the sulfate aerosols concentration across the entire globe, leading to stratosphere warming and troposphere cooling. After 2000, there are two more cooling phase of volcanic activities followed by the intensive El Niño event, which influenced depth extends to 2000m in the ocean. Then after that event, the ocean warming starts again dramatically. Both OHC700 and OHC2000 exhibit a rapid warming trend with more heat into the deep ocean.

The overall time and phase of the OHC variability simulated by CESM-LE and CESM-PAC model experiments in the upper 700m and upper 2000m compare with observations, suggesting these two model experiments have reasonable representations of the OHC and the analysis of both models is able to generate applicable results compared to the observed climate. Both CESM-LE and CESM-PAC experiments successfully reproduced the warming accelerating trend and two cooling phases in the late 20th century, despite the warming trends of upper 2000m since 2000 forced by two model experiments are slightly weaker than the observed ones. These weaker forced trends are due to the coupled climate model's limitations in the deep ocean simulation.

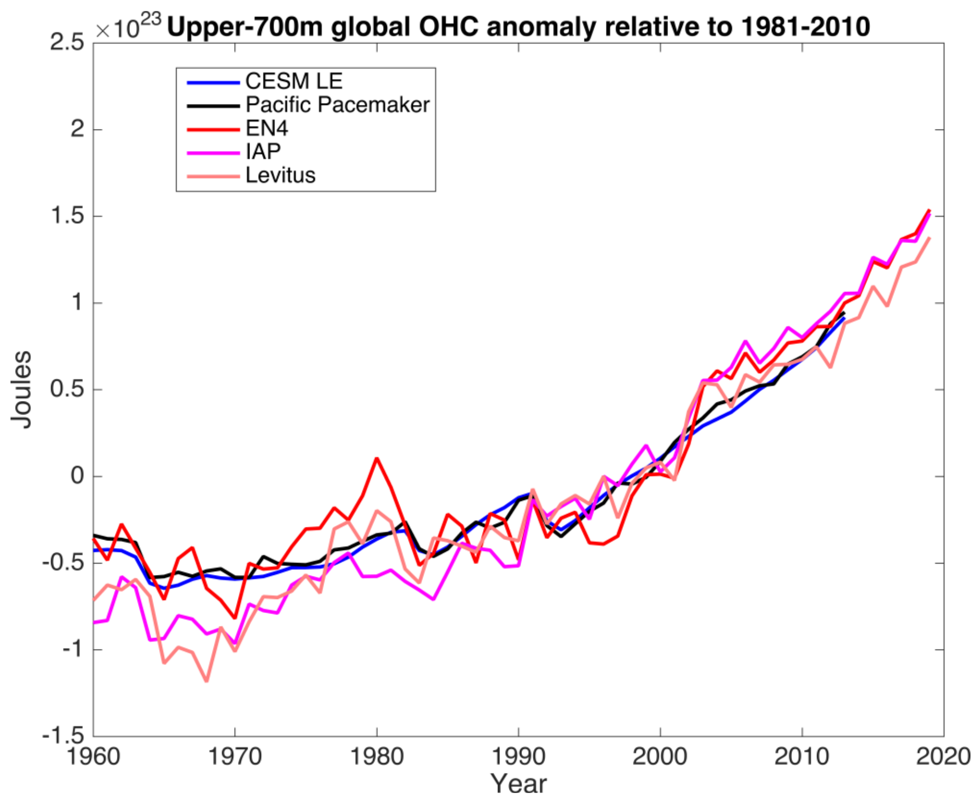

Figure 4.1. Time series of Ocean Heat Content integrated from 0 to 700 m from CESM-LE (blue), Pacific Pacemaker (black), EN4(red), IAP(Magenta) and Levitus (Pink). The time series show anomalies with respect to the 1981-2010 base period. The unit is Joules.

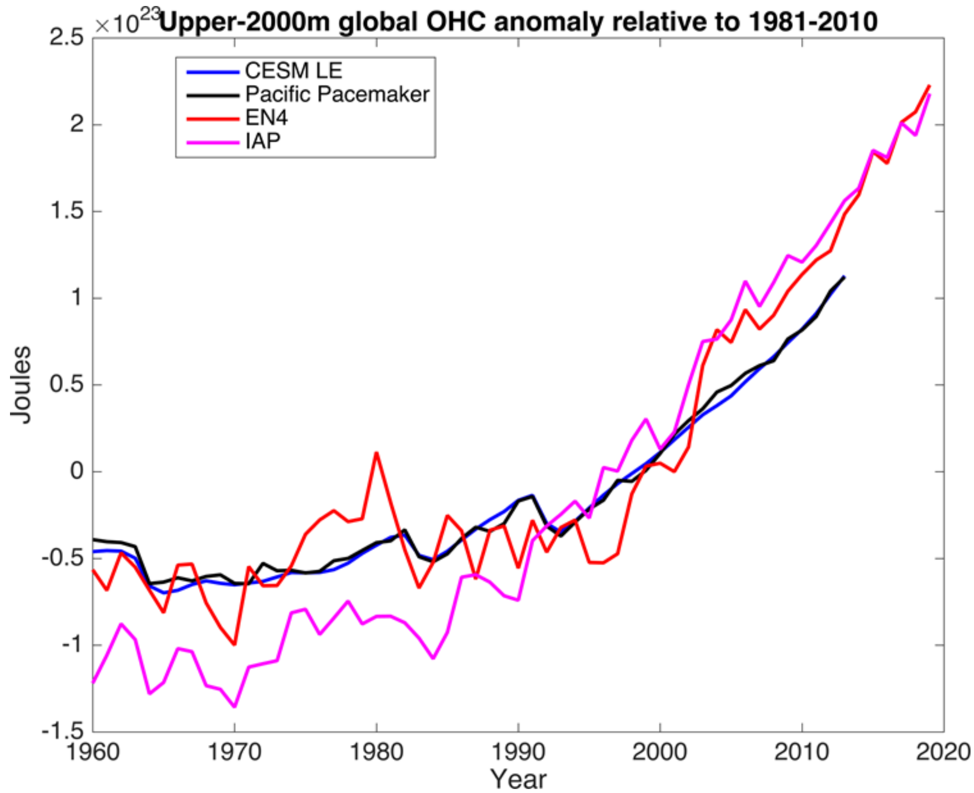

Figure 4.2. Similar to Figure 4.1.A but for the OHC integrated from 0 to 2000 m from CESM-LE (blue), Pacific Pacemaker (black), EN4(red), IAP(Magenta). The time series show anomalies with respect to the 1981-2010 base period. The unit is Joules.

4.3.2 Global OHC spatial pattern analysis

In this section, we explore the role of external forcing and tropical Pacific forcing in modulating the OHC variation in the Southern Ocean. Figure 4.3 shows the observed and forced OHC spatial patterns over three time periods. These three time periods include the temporary global surface warming slowdown period 2003–2012, the earlier period of the Argo record 2006–2013 and the multidecadal historical period 1979–2019.

Observed OHC trends during 1979–2013 based on IAP data (Figure 4.3a) exhibit a global wide warming, except for the tropical Pacific region. The positive warming trends are mostly found in the middle and high latitude of the Southern Hemisphere (SH). The negative OHC trends mainly appear in the eastern tropical Pacific, contrasted with the positive OHC trend in the western Pacific. During the warming slowdown 2003-2012 period (Figure 4.3b), observed OHC variation shows a clearly La Niña-like pattern with enhanced warming trend in the western Pacific and subtropical regions, such as the South Indian Ocean and South Pacific Ocean. Meanwhile, the cooling trends are enhanced with mostly appeared in the tropical Pacific, in the 60°S polar ward of the Southern Hemisphere and the North Atlantic. These enhanced warming and cooling trends also appear in the earlier period of the Argo record 2006–2013 (Figure 4.3c), but with more heat stored in the South Pacific Ocean and the South East Indian Ocean.

The externally forced responses by the CESM-LE show less contribution to the observed OHC variations. As shown in Figure 4.3d-f, the externally forced responses only capture the word-wide warming, showing the positive OHC trends nearly everywhere. Most of the warming occurs in the middle latitudes of the Southern Hemispheres between 30-60°S. Over the period of 2003-2012, the forced response of OHC shows a light cooling in the eastern tropical Pacific which is far smaller than the observed pattern. Meanwihle, the forced OHC spatial pattern in the tropical and middle latitude areas also shows a weak warming trend compared to the observation.

The most notable OHC pattern forced by the external forcing is a SAM-like pattern which is associated with the wind forcing in the Southern Hemisphere midlatitudes.

On the contrary, the Pacific forced responses successfully reproduced the observed OHC variations over three periods (Figure 4.3g-i), illustrating that the CESM-PAC model has captured the main physical processes that determine the OHC variability in the Southern Ocean. Over the 1979-2013, enhanced warming appears in the western Pacific and Southern Ocean showing a considerably larger warming magnitude than that forced by CESM-LE. The forced eastern Pacific cooling is also significant. The warming pattern in OHC trends in the Southern Hemisphere, similar in phase with only slightly weaker in magnitude compared to the observation, is also evident in Pacific Pacemaker. Furthermore, CESM-PAC has faithfully reproduced the observed both the warming and cooling pattern during the warming slowdown period and the earlier Argo period, whereas CESM-LE can only capture the worldwide warming, and its magnitude is evidently weaker than Pacific Pacemaker (Figure 4.3e and Figure 4.3f). The CESM-LE fail to present the cooling in the eastern Pacific and the high latitude in both hemispheres, and in the western tropical Indian Ocean it shows a warming trend, which is opposite to observation.

The pure Pacific forced response, assessed by differencing the CESM-PAC and CESM-LE patterns, greatly resembles the observed trend in most areas. During 1979-2013, the pure Pacific forced warming mainly occurs in the western Pacific, south Pacific and south east of Indian Ocean. During the warming slowdown period and Argo period (Figure 4.3k and Figure 4.3l), both the warming and cooling trends are enhanced, following the observed features. This confirms the tropical response largely accounts for warming pattern of Southern Ocean, with predominant contribution in the center of South Pacific Ocean and South East Indian Ocean in the mid-latitude between 20°-50°S. The upper 2000m OHC (Figure C.2) gives virtually the same patterns with slightly larger magnitudes.

In summary, the observed OHC variation during the historical record shows a La Niña-like pattern, recognized as large warming in the tropical western Pacific, Indian Ocean and Atlantic, and cooling in the eastern tropical Pacific and western tropical Indian Ocean. This La Niña-like warming and cooling pattern is enhanced during warming slowdown and the early Argo period, showing more heat is stored in the mid-latitude of the Southern Ocean. The OHC trend patterns simulated by PACE-EM are in good agreement with observations both over the long-term and short-term records, suggesting the internal variability associated with the tropical Pacific SST change accounts for most of the variability in the Southern Ocean. What is more, the pure Pacific forced OHC variability (after removing externally forced signal) confirms the tropical Pacific SST contributing to the rapid warming in the Southern Ocean, especially in the two warming spots in the South East Indian Ocean and the South Pacific Ocean. While the CESM-LE only represents worldwide warming and its forced magnitude is much smaller than that forced by PACE-EM, indicating external forcing makes a secondary contribution to the OHC variability in Southern Ocean warming.

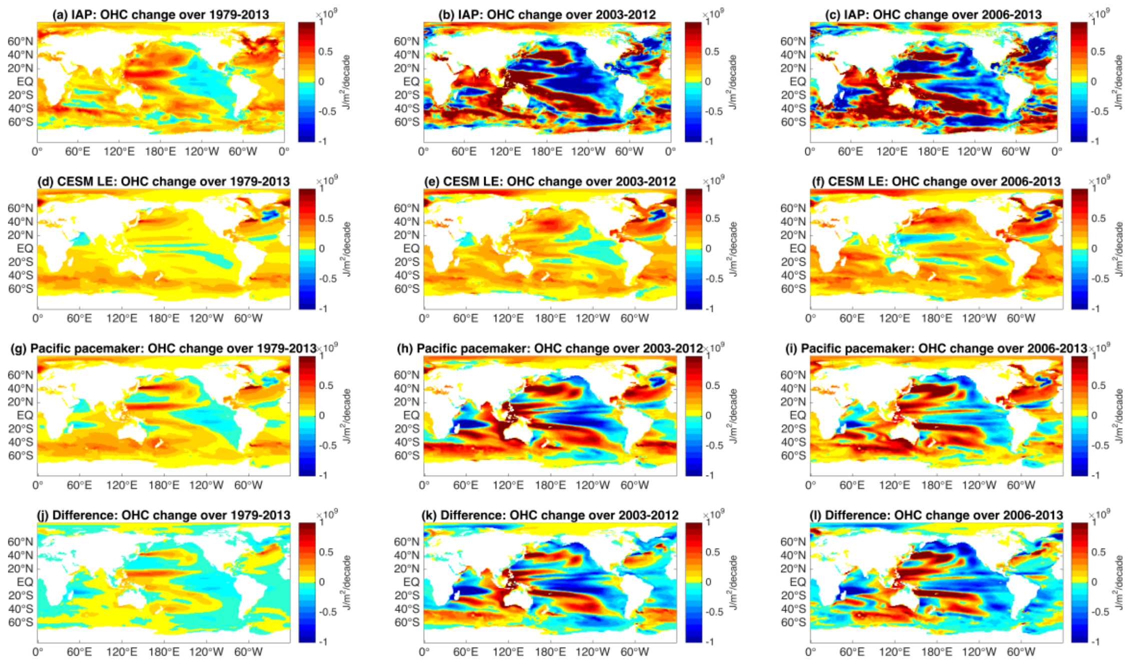

Figure 4.3. The Upper-700m depth-integrated OHC changes calculated from the IAP data and model simulations. (a) Spatial patterns of the OHC changes (J/m^2/decade) over 1979-2013, 2003-2012,2006-2013. (a)-(c) is from IAP data set. (d)-(e) is from CESM-LE model experiment. (g)-(i) is from the Pacific Pacemaker model experiment. (j)-(l) is obtained from Pacific Pacemaker model experiment minus CESM-LE ensemble mean.

4.3.3 Zonal mean of OHC change analysis

Figure 4.4 depicts the linear trend of the zonally integrated OHC700 fields for the three periods as a function of latitude for the global ocean. For the multi-decadal period 1979-2013 (Figure 4.4a), at nearly every latitude the global ocean has warmed. Relative extrema in the linear trend of OHC occurs at the mid-latitude of the Southern Hemisphere and the low latitude in the north. The result is robust in all observations, indicating that most heat gain for the long-term record is stored in the Southern Oceans and the tropical areas, such as the tropical Pacific and Atlantic oceans. Figure 4.4b and Figure 4.4c confirm the visual assessment of Southern Ocean warming with consistency across the observations and the model experiments. Integrating over the entire extratropical Southern Hemisphere oceans, the estimate of heat accumulation in the upper 700 meters ranges from 2.4 to 3.8×10^{21} J yr-1 during the 2003-2012 period and 2.1 to 4.6×10^{21} J yr-1 during the early Argo record period 2006-2013. The estimated trends in the tropical areas and the subtropical areas in the Northern Hemisphere are much weaker. The maximum heat gain occurs in the location of middle latitude around 40°S, near subtropical gyres cycle areas.

During the multi-decadal period 1979-2013 (Figure 4.4a), the Pacific Pacemaker has a good performance, showing a close time and phase with the observations in both hemispheres. The CESM-LE can reproduce the OHC trend well in the Southern Hemisphere, but in the Northern Hemisphere, especially in the tropical areas (0-20°N), CESM-LE forced warming trend only explain less half of the observed variance.

During the warming slowdown period over 2003-2012(Figure 4.4b), the peak of the observed warming trend near the 40°S is around 0.2 ZJ per latitude per year. The warming signal forced by external forcing explains only 40% (0.08 ZJ per latitude per year) of the observed variance. While, at the same latitude, the warming trend simulated by the PACE-EM is enhanced to 80% (0.15 ZJ per latitude per year). The slightly difference between PACE-EM and observation is likely induced by the intrinsic variabilities, associated with the strong SAM variability at that time. Both the CESM-LE and Pacific Pacemaker perform well in the Northern mid-latitude oceans.

During the early Argo period 2006-2013(Figure 4.4c), the warming signal forced by tropical Pacific compared to the warming trend forced by the external forcing increased around 20% in terms of the peak warming around 40°S, but it is still only about half of the observed warming. This weaker simulated trend may be due to the strong warming and cooling signals in the Southern Ocean may cancel out each other, leading to a small the zonal integration (Figure 4.3k and Figure 4.3l).

The above analysis indicates the Pacific forcing and external forcing both contribute to the Southern Ocean warming in multi-decadal time scales. However, the decadal OHC variability in the Southern Ocean is mainly linked to internal variability of the tropical Pacific. The discrepancy of decadal OHC variability between the Pacific forced and the observation implies the local natural variabilities, such as the SAM variability which is enhanced during the warming slowdown period, may have some contributions to the recent enhanced Southern Ocean warming.

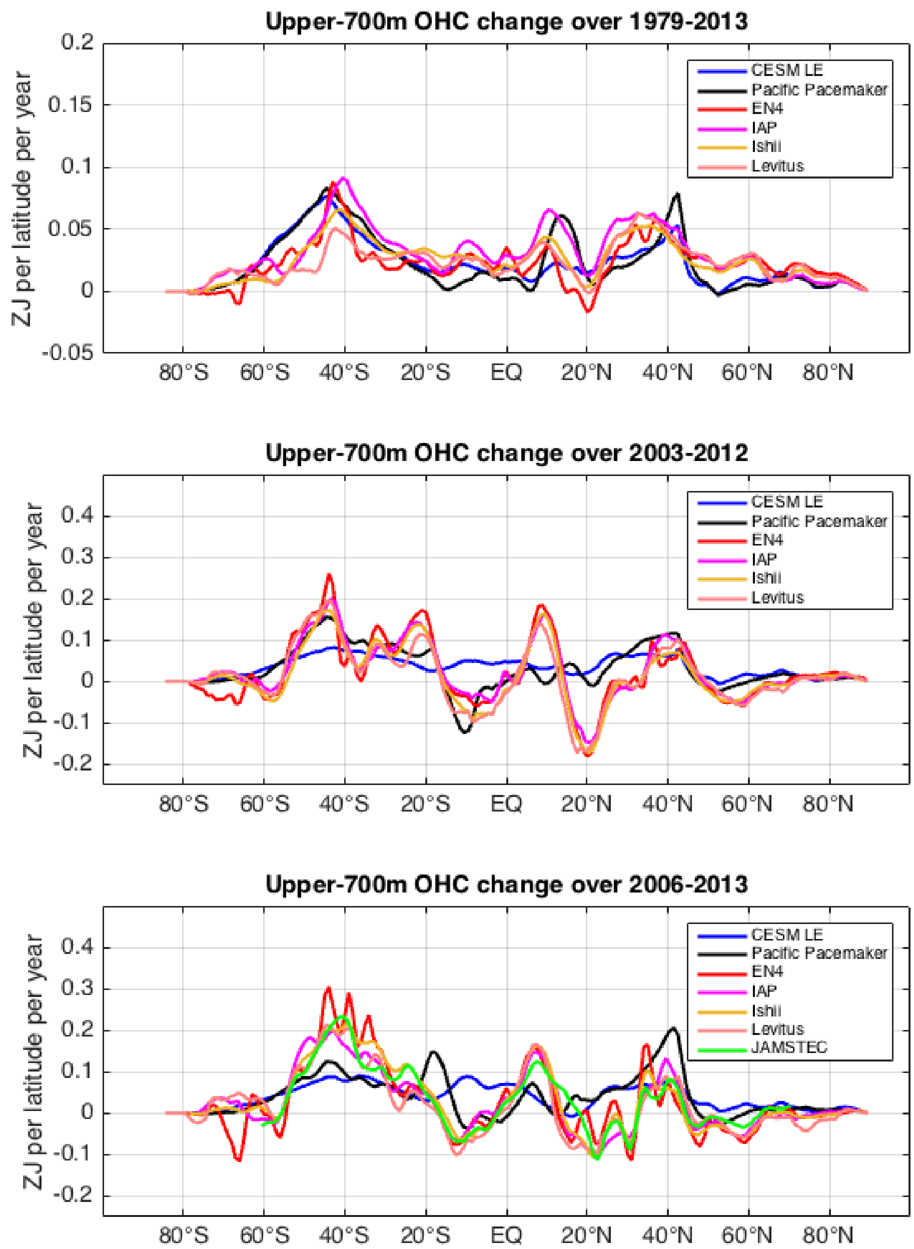

Figure 4.4. Globally zonal integrated OHC changes (ZJ per degree latitude per year) in the upper 700m over 1979-2013(a), 2003–2012 (b) and 2006-2013(c). CESM-LE (blue), Pacific Pacemaker (black), EN4(red), IAP (magenta) Ishii (orange), Levitus (pink), JAMSTEC (green). Note, the JAMSTEC data is only showed in the period of 2006-2013.

4.4 South Pacific and Southeast Indian Ocean analysis

The enhanced Southern Ocean warming over 2003-2012 and 2006–2013, has two centers of maximum OHC increase located in the southeast Indian Ocean (SEIO) and South Pacific Ocean (SPAC) (Figure 4.3k and Figure 4.3l). Thus, our further analysis will focus on these two hotspots to quantify the relative contributions of external forcing and Pacific forcing to OHC variability in the Southern Ocean. From the global OHC change analysis, the tropical Pacific forcing is suggested to be responsible for the fast warming in these two regions. To have a closer look at how the tropical Pacific forcing and external forcing contribute to this enhanced Southern Oceans warming, the upper-700m OHC time series integrated over the SEIO (20°–50°S, 70°–110°E) and SPAC (185°–240°S, 20°–50°E), the same domains as used in the study of Llovel and Terray (2016), are analyzed during 1960-2013 (Figure 4.5 and Figure 4.6).

The OHC time series in these two regions exhibits considerable interannual variations and continues warming during the historical period and warming acceleration period since 2003. All ensemble members of both the CESM-LE and CESM-PAC experiments exhibit positive trends during 1960-2013, consistent with the observed warming trend. The CESM-PAC ensembles (Figure 4.5, dark gray lines) closely follow most of the interannual and decadal variations of observed OHC change. The forced signal by the ensemble mean of CESM-PAC (Figure 4.5, black line) shows closer time and phase with the observed OHC change (Figure 4.5, red line), especially successfully reproduces the rapid warming since 2003. While the CESM-EM only represents the long-term warming trend, its forced magnitude is much smaller than that of observation.

To compare the observed and modeled OHC trends, the upper 700 integrated OHC trends are calculated over the three periods for the observation, the ensemble mean and each ensemble member (Figure 4.7 and Figure 4.8). During the multi-decadal period 1979-2013, in the SPAC region (Figure 4.7), the OHC trends estimated by observation, CESM-EM, and PACE-EM are 2.2×10^8, 0.9×10^8 and 1.5×10^8 J/m^2/ decade, respectively. The PACE-EM simulated trends are closer to observation, with a small spreading in ensemble members (ranging from 0.5×10^8 ~ 2.3×10^8 J/m^2/ decade). The CESM-LE forced OHC trends are all smaller than the observed trend largely spreading from -0.3×10^8 J/m^2/decade to 2.1×10^8 J/m^2/decade.

During the 2003-2012 period, the forced response from PACE-EM is 0.4×10^9 J/m^2/decade, two times bigger than that from CESM-EM. The simulated trends from CESM-PAC are all positive trends. Its maximum trend is around 0.9×10^9 J/m^2/decade, slightly higher than the observed trend (0.75×10^9 J/m^2/decade). The CESM-LE shows a wide spreading among ensemble members, containing both negative and positive trends starting from -0.4×10^9 J/m^2/decade to 0.7×10^9 J/m^2/ decade.

Similar results are shown over the Argo period. The observed warming trend increased to 0.8×10^9 J/m^2/decade. The forced trend from CESM-EM is around 0.2×10^9 J/m^2/ decade. The ensemble members from CESM-LE show both positive and negative trends with the highest trend around 1.25×10^9 J/m^2/decade. While the PACE-EM trend is twice larger than the CESM-EM and 95% of the forced trends are positive trends. The estimations of the warming trends over these three periods bring evidence that internal variability from the eastern Pacific, plus the external forced response largely account for the phase and magnitude of the warming variations in the SPAC.

The results in SEIO shows a different story. Over the multi-decadal period 1979-2013, external forcing generated trend (2.05×10^8 J/m^2/decade) almost the same as the observation (2×10^8 J/m^2/decade). The ensemble members in CESM-LE are close to the observed trend with a range of 0.25×10^8 J/m^2/decade to 3.5×10^8 J/m^2/decade. While the trend forced by PACE-EM is 25% larger than the observed trend. However, over the warming slowdown period 2003-2012 and the early Argo period 2006-2013, CESM-PAC model turns to be able to reproduce closer trend values than CESM-LE, indicating the tropical Pacific forcing is also responsible for OHC variability in SEIO in the decadal time scale.

The OHC trends analysis in SPAC and SIO further reveals a key role of tropical Pacific in modulating the decadal OHC variability in Southern Ocean.

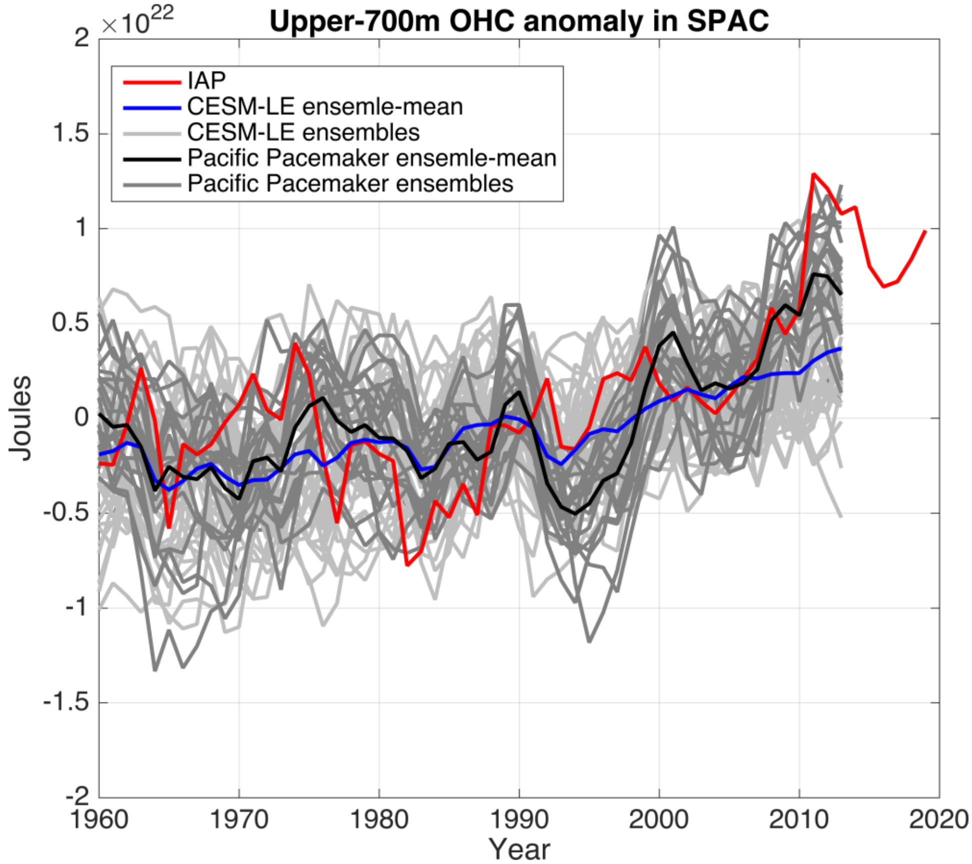

Figure 4.5. Upper-700m depth-integrated OHC changes in SPAC during 1960-2013. The light gray lines are CESM-LE ensemble members. The blue line is the CESM-LE ensemble mean. The dark gray lines are the Pacific Pacemaker ensemble members. The black line is the Pacific Pacemaker ensemble mean. The red line is the IAP data starting from 1960 to 2019. All OHC time series is anomalies relative to 1981-2010.

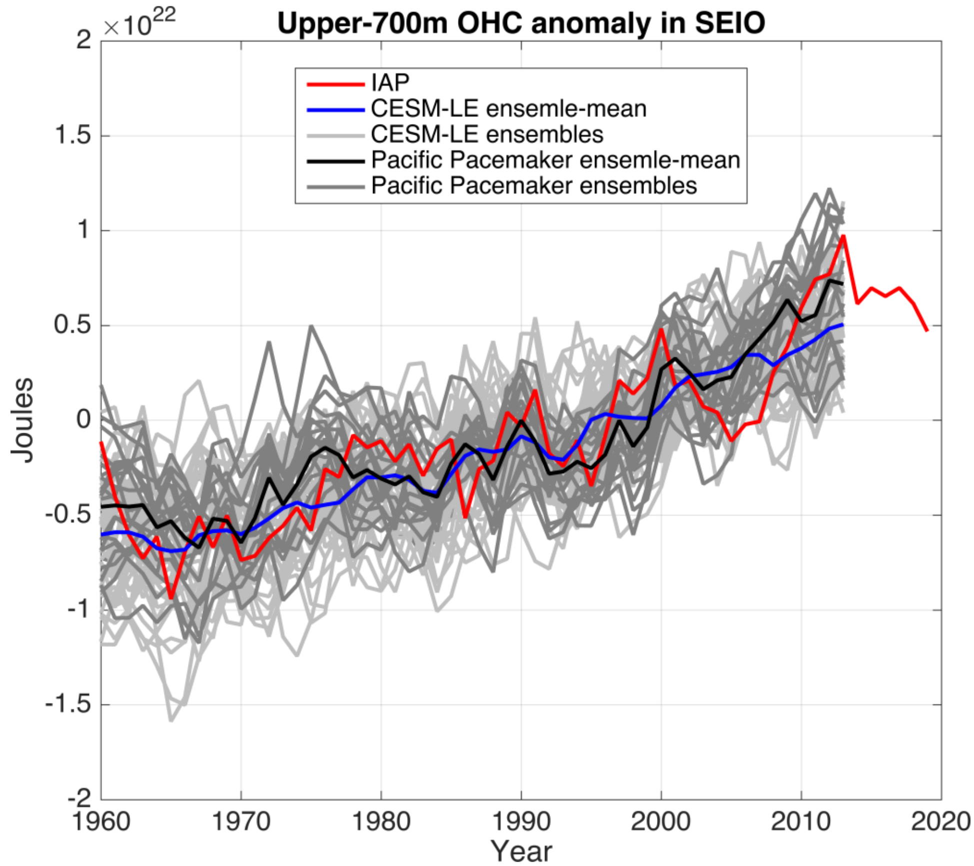

Figure 4.6. Upper-700m depth-integrated OHC changes in SEIO during 1960-2013. The light gray lines are CESM-LE ensemble members. The blue line is the CESM-LE ensemble mean. The dark gray lines are the Pacific Pacemaker ensemble members. The black line is the Pacific Pacemaker ensemble mean. The red line is the IAP data starting from 1960 to 2019. All OHC time series is anomalies relative to 1981-2010.

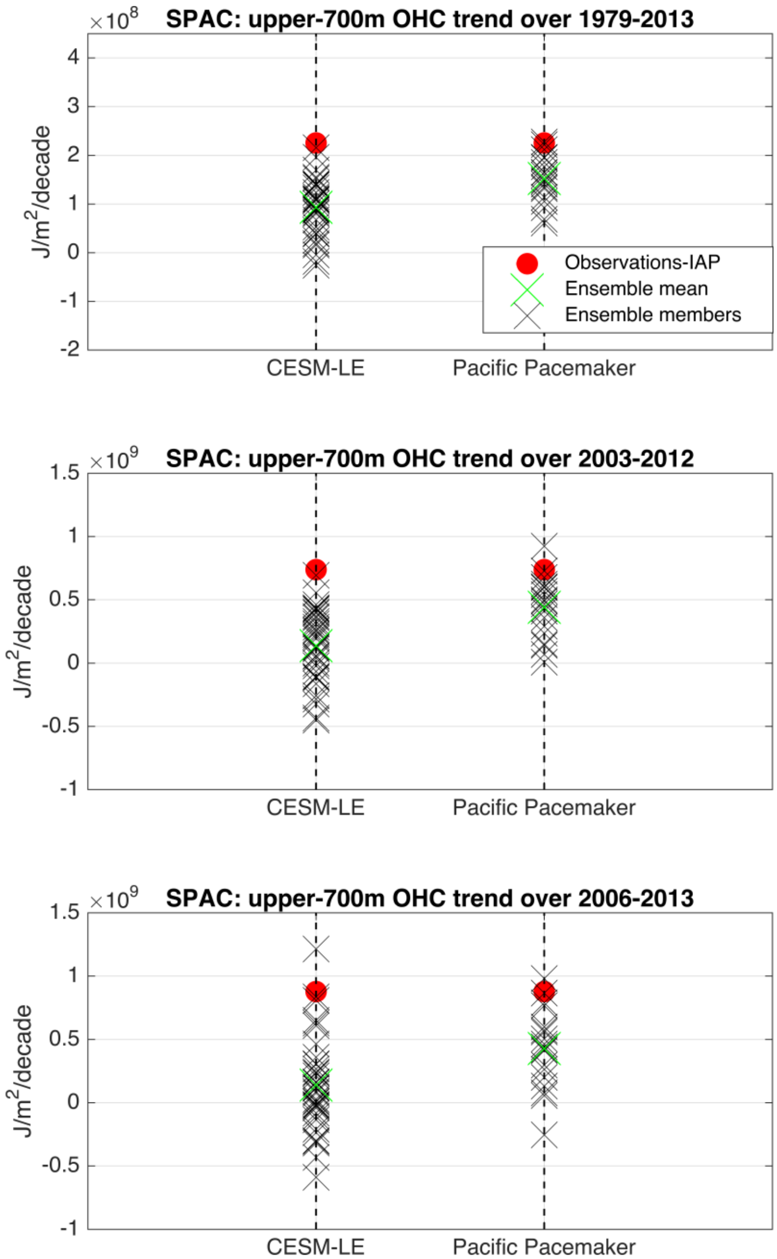

Figure 4.7. Upper-700m depth-integrated OHC trends in SPAC during (a) 1979-2013; (b)2003-2012; (c) 2006-2013. The red dot is the observed trend by IAP data. The green cross is trend from the ensemble mean. The black cross is the trend from each ensemble member.

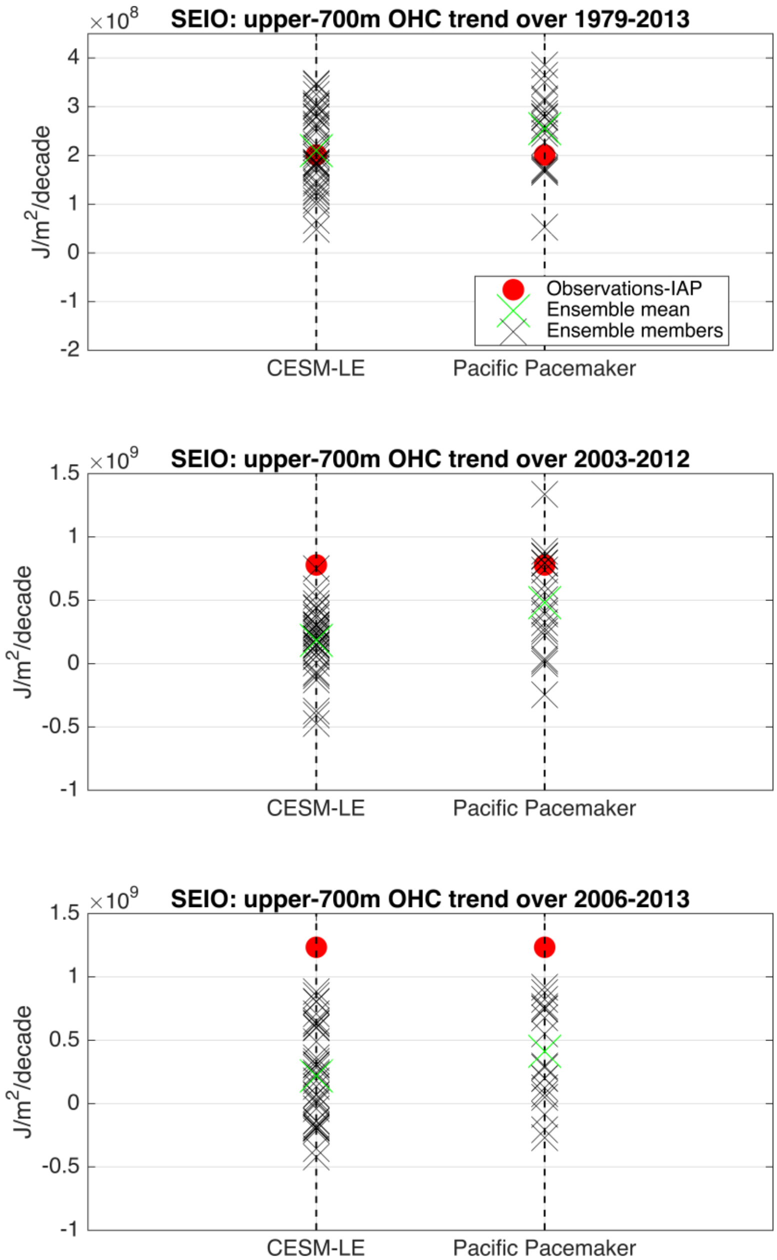

Figure 4.8. Upper-700m depth-integrated OHC trends in SEIO during (a) 1979-2013; (b)2003-2012; (c) 2006-2013. The red dot is the observed trend by IAP data. The green cross is trend from the ensemble mean. The black cross is the trend from each ensemble member.

4.5 Mechanisms

Next, we will examine the related physical mechanisms of the Southern Oceans warming using the EOF decomposition technique (Figure 4.9). The dominant mode (EOF1) forced by pure tropical Pacific forcing contains La Niña signal in the tropical Pacific, referred to ‘La Niña-like” mode. It has the shape of an equatorial cold tongue pattern in the eastern Pacific and a warming pattern in the western Pacific. The dominant mode (EOF1) derived from IAP has a similar pattern with the tropical Pacific forced pattern, except for the tropical Atlantic. Its time series, PC, is dominated by interannual variability and is highly correlated with IPO index (r=-0.86) and Nino3.4 index (r=-0.83) (Table C.1). The EOF2 decomposed from IAP has a spatial pattern with worldwide warming, except for the western tropical Pacific. The related PC time series reveals a dominant increasing trend over the historical period. While in the recent decade, since 2010, this warming rate has slowed down. By smoothing the PC of EOF2 from IAP data and the SAM index, a high correlation coefficient r=0.76 is estimated, indicating this long-term warming trend and the recent decadal shift is related to the SAM variability. These results further illustrate that the decadal variability of the Southern Ocean warming is due to the natural variability induced by the SAM and the tropical Pacific.

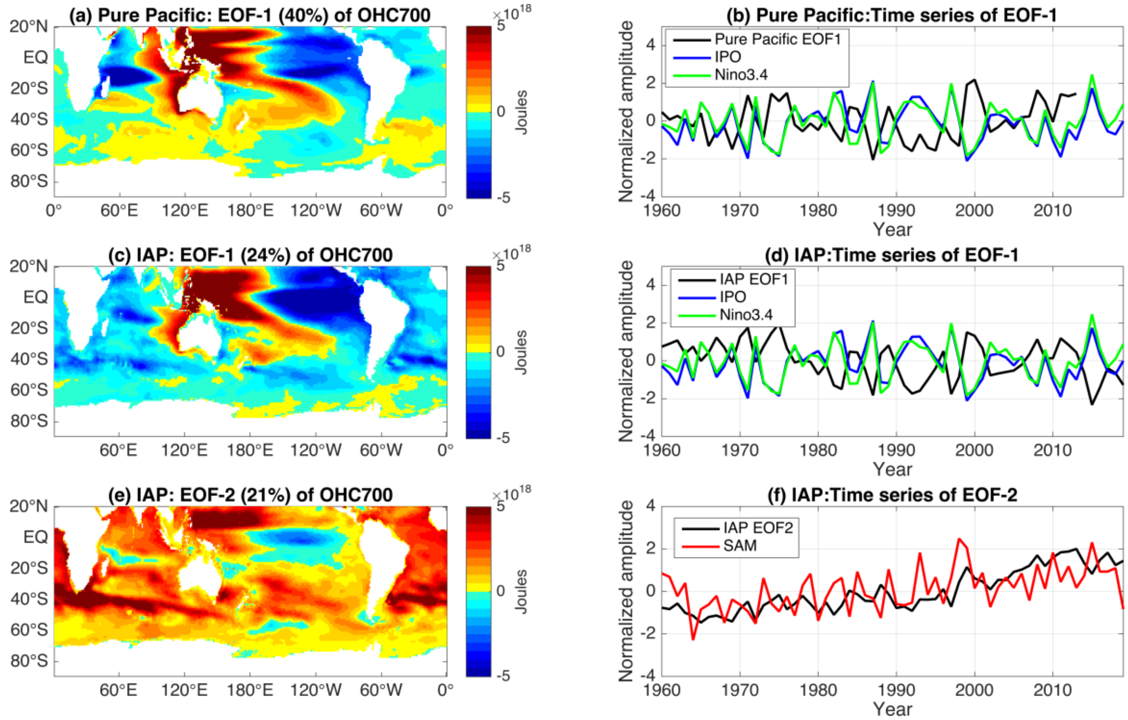

Figure 4.9. The EOF decomposition of upper-700m depth-integrated OHC change from Pacific experiment over 1960-2013 and from IAP data over 1960-2020. (a) is the first EOF mode derived from pure Pacific forced OHC variability and (b) is its corresponding PC time series (black line on the right). (c) to (f) are the EOF modes and their PC time series obtained from IAP data.

4.6 Summary and Discussion

In this chapter, the output from coupled CESM model experiments is used to examine the contributions of internal variability from the tropical eastern Pacific and the external forcing to the variations of heat gain in the subsurface Southern Ocean. The mechanisms of what internal climate variability in the Pacific Ocean drives the recent decadal variability in the Southern Ocean are also studied.

Two model experiments obtained from the CESM Large Ensemble project are used for the trend, time series and spatial pattern analysis. The CESM-LE experiment is used to examine the external forcing in explaining the explaining recent enhanced warming in the South Ocean. Given that the CESM-LE forced warming, both its spatial pattern and the time series variation is not comparable to the observed increase during 1979–2013 and the warming slowdown period, it seems that externally forced responses alone is not sufficient to generate the recent increased warming trend. The CESM-PAC model experiment provide evidence that the SST variations in the eastern Pacific drives the heat variations in the Southern Ocean. In particular, the Pacemaker experiment successfully generates similar warming patterns with the observation during three periods. Especially, the enhance warming in the early 21st century. Additionally, the CESM-PAC experiment captures the dominant pattern of warming trends in the mid-latitude of Southern Hemisphere, and significant warming in the Southeast of Indian Ocean and the South Pacific Ocean has been represented by the Pacific forcing. Nudging with the observed tropical Pacific SST variation enables the model simulations reproduce more realistically phenomenon and reduce the model-observation discrepancies.

The EOF decomposition method is applied both on the Pacific forced OHC and the observed OHC to find out the dominant mode in the Southern Ocean warming. The leading mode is suggested to be highly correlated with the IPO and Nino 3.4 index, highlighting the role of SST variations in the tropical Pacific in driving the decadal variations in Southern Ocean warming. While the second dominant mode has linked the warming acceleration in the Southern Ocean to the SAM variability. This confirms the finding derived from the second part of this dissertation that both the Pacific and the SAM contribute to the decadal shift in the South Ocean warming. The results obtained from the two sets of models may limited to the model experiment conditions and model sample size. Thus, further examinations on multiple model comparison and large model sample size are needed.

Chapter 5

CONCLUSIONS

Starting with the GST historical evolution and its recent warming slowdown during 2003-2012, I have investigated the main drivers of the GST change in different time scales and identified the importance of internal variability related to the eastern Tropical Pacific in modulating the decadal variation in Southern Ocean warming. Moreover, the contributions from Pacific forcing are quantified for the two warming hotspots in the Southeast Indian Ocean and South Pacific Ocean.

5.1 The drivers for the GST change in historical record

The recent slowdown of the global surface temperature has caused great attention in research community. The explanations of this warming slowdown have been discussed by a great number of authors in literature. There has been an inconclusive debate about whether the external forcing or the internal climate variabilities originated from the Pacific and the Atlantic is the main driver of this warming slowdown. In this part, the observed GST data and coupled climate model experiments are used to have a further examination on the role of external forcing and internal variabilities in modulating the GST change.

The observed GST derived from Hadcrut4 data has been decomposed into signals with different time scales. The IAV signals are those with periods lower than 8 years. The signals with periods ranging from 9-30 years are considered as inter-decadal signal (IDV). The multi-decadal variation (MDV) contains the signals with a mean period of around 60 years. And a long-term secular trend (ST). In order to get some indication of related physical dynamical processes, the ERSST is regressed on these four signals. The results reveal that IAV and IDV signals resemble ENSO like patterns, which are associated with the SST variability in the eastern tropical Pacific Ocean. The MDV signal generated a pattern more related to the AMO, resembles the AMO-like signal. The monotonous increasing secular trend and its worldwide warming spatial pattern is related to the buildup of anthropogenic greenhouse gases in the last twentieth century. The decomposition of GST is indicative of the internal variabilities that prominently generated by the Pacific and Atlantic and external variabilities caused by anthropogenic forcing are likely to be responsible for the variation of the GST.

A suite of climate coupled model simulations is analyzed to identify the role of the Pacific, the Atlantic, and the external forcing in modulating the observed GST over the historical periods. We first assess the role of external forcing using the CESM-LE experiment. The close resemblance of the MDV time series and its spatial pattern between the observation and the externally generated variation suggests that the external forcing is driving the GST change in multi-decadal time scales. For example, the MDV time series forced by CESM-EM explains 72% of the observed variance. The consistency among the ensemble member convinces this assumption.

The second model with fixed aerosol forcing, termed as CESM-xaer, is used to examine the contributions from aerosol forcing. The results show that, without aerosol forcing, the externally forced response is not strong enough to control the MDV change. This model experiment confirms the importance of external forcing in modulating the MDV change. Most importantly, it reveals aerosol forcing is the main driver of MDV among all the radiative external forcing.

Next, the CESM-PAC is used to identify the contributions from the Pacific forcing. The forced IAV and IDV signals generate spatial patterns and phase and time changes that are consistent to the observation, indicating the SST variations from the eastern tropical Pacific accounts for most of GST variations at interannual and inter-decadal time scales. For example, the Pacific forced IDV signal successfully captures the recent warming slow down during 2003-2012, consistent with previous study (Kosaka and Xie, 2013) that the Pacific cooling caused the recent warming slowdown.

And then the CESM-ATL model experiment is assessed to figure out the role of Atlantic forcing. The Atlantic also has the ability to reproduce the recent observed declining trend in IDV, implying it has contributed to the GST changes in inter-decadal time scale through the atmosphere teleconnection. Unlike previous studies demonstrated, our analysis shows the Atlantic forcing alone is not able to control the MDV change. The forced amplitude of MDV is far small compared to the observed MDV, indicating fewer contributions to the GST change in the multi-decadal time scale.

Therefore, we conclude that external forcing is responsible for the GST change in the multi-decadal time scale. Among all the radiative external forcing, the aerosol forcing performs as the main driver for MDV change. The Pacific forcing mainly modulates GST changes mainly in the inter-annual and inter-decadal time scale. The Atlantic forcing also contributes to the GST change in inter-decadal time scale. We further suggest the prolonged warming slowdown periods of ~30 years (1945-1975) are due to the MDV signal, whereas the relatively shorter warming slowdown periods, such as the recent one over 1998-2014, are mainly caused by IDV signal.

5.2 Decadal shift of warming in the Southern Ocean

The rapid warming in the Southern Hemisphere extratropical oceans, particularly, in the SEIO and SPAC has slowed down and reversed to a cooling trend over 2013–2019. The heat content is also estimated over the entire available Argo period over 2006–2019. The contribution of the Southern Ocean warming to the global ocean heat storage is ~65%, showing lower estimates compared to the previous estimates over the earlier Argo period, e.g., 90% over 2005–2014 (Llovel and Terray, 2016). The SAM and IPO indexes are used to identify their relationships with this decadal variation. The result shows that this recent decadal shift is modulated by decadal variations in the SAM and IPO, with a possible contribution from tropical Pacific teleconnections.

The mechanisms for this decadal shift are investigated by decomposing the subsurface ocean temperature and salinity changes into heave and spice components. The heave component is the changes along the isopycnals, while the spice component is the changes caused by the movement of the isopycnals which is associated with the water mass process. The warming (cooling) in the subsurface ocean over the earlier (later) warming slowdown period were largely induced by the deepening (shoaling) of isopycnals in response to changing winds. The earlier rapid warming period was also featured by an enhancement of the multidecadal spice change patterns, especially in terms of the cooling and freshening changes along the isopycnals within the SAMW and AAIW, which are likely signatures of the surface buoyancy forcing. Note that the salinity change patterns were instead dominated by the spice component, suggesting that the temperature and salinity changes are determined by different dynamical processes, which requires further investigation.

5.3 Pacific forcing enhanced the Southern Ocean warming

The potential role of external forcing and Pacific forcing in contributing to the recent rapid Southern Oceans warming is quantified using the coupled CESM-LE and CESM-PAC model experiments.

The CESM-LE forced warming pattern and the OHC time series variation is not comparable to the observed increase during 1979–2013, 2003-2012 and 2006-2013 periods. It seems that externally forced response alone is not strong enough to generate an enhanced warming pattern as the observation, indicating that the external forcing is not the main driver in modulating the OHC variability in Southern Ocean. On the contrary, the CESM-PAC model experiment which is nudged with observed SST variability in the tropical Pacific can successfully reproduce similar warming pattern with the observation during three periods, as well as the similar time series of OHC change in Southern Oceans, suggesting the tropical Pacific forcing is the dominant driver for Southern Ocean warming. In addition, the Pacemaker experiment is able to reproduce the warming (cooling) patterns in the Southeast Indian Ocean and the South Pacific Ocean during/after the warming slowdown period.

The EOF decomposition is applied to identify the dominant mode in Southern Ocean warming and its related physical mechanisms. The first mode is highly correlated with the IPO and Nino 3.4 index, suggesting that SST variability in the tropical Pacific is driving the decadal variations in Southern Ocean warming. While the second dominant mode has linked the Southern Ocean warming and its recent warming slowdown to the SAM variability. This confirms the finding obtained from the second part of this dissertation that both the Pacific and the SAM contribute to the decadal shift in the South Ocean warming.

REFERENCES

Alexander, M. A., Bladé, I., Newman, M., Lanzante, J. R., Lau, N. C., & Scott, J. D. (2002). The atmospheric bridge: The influence of ENSO teleconnections on air–sea interaction over the global oceans. Journal of climate, 15(16), 2205-2231.

Aoki, S., Bindoff, N. L., & Church, J. A. (2005). Interdecadal water mass changes in the Southern Ocean between 30oE and 160oE. Geophysical Research Letters, 32, L07607. https://doi.org/10.1029/2004GL022220.

Arblaster, J. M., & Meehl, G. A. (2006). Contributions of external forcings to southern annular mode trends. Journal of climate, 19(12), 2896-2905.

Argo. (2020). Argo float data and metadata from Global Data Assembly Centre (Argo GDAC): SEANOE. https://doi.org/10.17882/42182.

Balmaseda, M. A., Trenberth, K. E., & Källén, E. (2013). Distinctive climate signals in reanalysis of global ocean heat content. Geophysical Research Letters, 40(9), 1754-1759.

Banks, H. T., & Bindoff, N. L. (2003). Comparison of observed temperature and salinity changes in the Indo-Pacific with results from the coupled climate model HadCM3: Processes and mechanisms. Journal of Climate, 16(1), 156–166. https://doi.org/10.1175/1520-0442(2003)016<0156:COOTAS>2.0.CO;2

Bellomo, K., Clement, A. C., Murphy, L. N., Polvani, L. M., & Cane, M. A. (2016). New observational evidence for a positive cloud feedback that amplifies the Atlantic Multidecadal Oscillation. Geophysical Research Letters, 43(18), 9852-9859.

Bindoff, N. L., & Church, J. A. (1992). Warming of the water column in the southwest Pacific Ocean. Nature, 357(6373), 59–62. https://doi.org/10.1038/357059a0.

Bindoff, N. L., & Mcdougall, T. J. (1994). Diagnosing climate change and ocean ventilation using hydrographic data. Journal of Physical Oceanography, 24(6), 1137–1152. https://doi.org/10.1175/1520-0485(1994)024<1137:DCCAOV>2.0.CO;2.

Böning, C. W., Dispert, A., Visbeck, M., Rintoul, S. R., & Schwarzkopf, F. U. (2008). The response of the Antarctic Circumpolar Current to recent climate change. Nature Geoscience, 1(12), 864–869. https://doi.org/10.1038/ngeo362.

Booth, B. B., Dunstone, N. J., Halloran, P. R., Andrews, T., & Bellouin, N. (2012). Aerosols implicated as a prime driver of twentieth-century North Atlantic climate variability. Nature, 484(7393), 228-232.

Brohan, P., Kennedy, J. J., Harris, I., Tett, S. F., & Jones, P. D. (2006). Uncertainty estimates in regional and global observed temperature changes: A new data set from 1850. Journal of Geophysical Research: Atmospheres, 111(D12).

Bronselaer, B., & Zanna, L. (2020). Heat and carbon coupling reveals ocean warming due to circulation changes. Nature, 584(7820), 227–233. https://doi.org/10.1038/s41586-020-2573-5.

Brown, P. T., Ming, Y., Li, W., & Hill, S. A. (2017). Change in the magnitude and mechanisms of global temperature variability with warming. Nature climate change, 7(10), 743-748.

Cai, W., Cowan, T., Godfrey, S., & Wijffels, S. (2010). Simulations of processes associated with the fast warming rate of the southern midlatitude ocean. Journal of Climate, 23(1), 197–206. https://doi.org/10.1175/2009JCLI3081.1

Chen, X., & Tung, K. K. (2014). Varying planetary heat sink led to global-warming slowdown and acceleration. Science, 345(6199), 897–903. https://doi.org/10.1126/science.1254937

Chen, X., & Tung, K. K. (2018). Global-mean surface temperature variability: Space–time perspective from rotated EOFs. Climate Dynamics, 51(5), 1719-1732.

Cheng, L., Trenberth, K. E., Fasullo, J., Boyer, T., Abraham, J., & Zhu, J. (2017). Improved estimates of ocean heat content from 1960 to 2015. Science Advances, 3(3), e1601545.

Cionni, I., Eyring, V., Lamarque, J. F., Randel, W. J., Stevenson, D. S., Wu, F., ... & Waugh, D. W. (2011). Ozone database in support of CMIP5 simulations: results and corresponding radiative forcing. Atmospheric Chemistry and Physics, 11(21), 11267-11292.

Cionni, I., Eyring, V., Lamarque, J. F., Randel, W. J., Stevenson, D. S., Wu, F., ... & Waugh, D. W. (2011). Ozone database in support of CMIP5 simulations: results and corresponding radiative forcing. Atmospheric Chemistry and Physics, 11(21), 11267-11292.

Clément, L., McDonagh, E. L., Marzocchi, A., & Nurser, A. J. G. (2020). Signature of ocean warming at the mixed layer base. Geophysical Research Letters, 47(1), e2019GL086269. https://doi.org/10.1029/2019GL086269.

Dai, A., Fyfe, J. C., Xie, S. P., & Dai, X. (2015). Decadal modulation of global surface temperature by internal climate variability. Nature Climate Change, 5(6), 555-559.

DelSole, T., Tippett, M. K., & Shukla, J. (2011). A significant component of unforced multidecadal variability in the recent acceleration of global warming. Journal of Climate, 24(3), 909-926.

Delworth, T. L., Zeng, F., Vecchi, G. A., Yang, X., Zhang, L., & Zhang, R. (2016). The North Atlantic Oscillation as a driver of rapid climate change in the Northern Hemisphere. Nature Geoscience, 9(7), 509-512.

Desbruyeres, D., McDonagh, E. L., King, B. A., & Thierry, V. (2017). Global and full-depth ocean temperature trends during the early twenty-first century from argo and repeat hydrography. Journal of Climate, 30(6), 1985–1997. https://doi.org/10.1175/JCLI-D-16-0396.1

Deser, C., Lehner, F., Rodgers, K. B., Ault, T., Delworth, T. L., DiNezio, P. N., ... & Ting, M. (2020) a. Insights from Earth system model initial-condition large ensembles and future prospects. Nature Climate Change, 10(4), 277-286.

Deser, C., Phillips, A. S., Simpson, I. R., Rosenbloom, N., Coleman, D., Lehner, F., ... & Stevenson, S. (2020) b. Isolating the evolving contributions of anthropogenic aerosols and greenhouse gases: A new CESM1 large ensemble community resource. Journal of climate, 33(18), 7835-7858.

Dias, F. B., Fiedler, R., Marsland, S. J., Domingues, C. M., Clément, L., Rintoul, S. R., et al. (2020). Ocean heat storage in response to changing ocean circulation processes. Journal of Climate, 33(21), 9065–9082. https://doi.org/10.1175/JCLI-D-19-1016.1

Durack, P. J., & Wijffels, S. E. (2010). Fifty-year trends in global ocean salinities and their relationship to broad-scale warming. Journal of Climate, 23(16), 4342–4362. https://doi.org/10.1175/2010JCLI3377.1

Durack, P. J., Gleckler, P. J., Landerer, F. W., & Taylor, K. E. (2014). Quantifying underestimates of long-term upper-ocean warming. Nature Climate Change, 4(11), 999-1005.

Easterling, D. R., & Wehner, M. F. (2009). Is the climate warming or cooling?. Geophysical Research Letters, 36(8).

England, M. H., McGregor, S., Spence, P., Meehl, G. A., Timmermann, A., Cai, W., et al. (2014). Recent intensification of wind-driven circulation in the Pacific and the ongoing warming hiatus. Nature Climate Change, 4(3), 222–227. https://doi.org/10.1038/nclimate2106

Foster, G., & Rahmstorf, S. (2011). Global temperature evolution 1979–2010. Environmental research letters, 6(4), 044022.

Fröhlich, E. (2012). The role of surface charge in cellular uptake and cytotoxicity of medical nanoparticles. International journal of nanomedicine, 7, 5577.

Frölicher, T. L., Sarmiento, J. L., Paynter, D. J., Dunne, J. P., Krasting, J. P., & Winton, M. (2015). Dominance of the Southern Ocean in anthropogenic carbon and heat uptake in CMIP5 models. Journal of Climate, 28(2), 862–886. https://doi.org/10.1175/JCLI-D-14-00117.1

Fyfe, J. C., & Saenko, O. A. (2006). Simulated changes in the extratropical Southern Hemisphere winds and currents. Geophysical Research Letters, 33(6).

Gao, L., Rintoul, S. R., & Yu, W. (2018). Recent wind-driven change in Subantarctic Mode water and its impact on ocean heat storage. Nature Climate Change, 8(1), 58–63. https://doi.org/10.1038/s41558-017-0022-8

Gastineau, G., Friedman, A. R., Khodri, M., & Vialard, J. (2019). Global ocean heat content redistribution during the 1998–2012 Interdecadal Pacific Oscillation negative phase. Climate Dynamics, 53(1–2), 1187–1208. https://doi.org/10.1007/s00382-018-4387-9

Gille, S. T. (2008). Decadal-scale temperature trends in the Southern Hemisphere ocean. Journal of Climate, 21(18), 4749–4765. https://doi.org/10.1175/2008JCLI2131.1

Gillett, N. P., & Thompson, D. W. (2003). Simulation of recent Southern Hemisphere climate change. Science, 302(5643), 273-275.

Good, S. A., Martin, M. J., & Rayner, N. A. (2013). EN4: Quality controlled ocean temperature and salinity profiles and monthly objective analyses with uncertainty estimates. Journal of Geophysical Research: Oceans, 118(12), 6704–6716. https://doi.org/10.1002/2013JC009067

Gregory, J. M. (2000). Vertical heat transports in the ocean and their effect on time-dependent climate change. Climate Dynamics, 16(7), 501-515.

Häkkinen, S., Rhines, P. B., & Worthen, D. L. (2016). Warming of the global ocean: Spatial structure and water-mass trends. Journal of Climate, 29(13), 4949–4963. https://doi.org/10.1175/JCLI-D-15-0607.1

Hartmann, D. L., Tank, A. M. K., Rusticucci, M., Alexander, L. V., Brönnimann, S., Charabi, Y. A. R., ... & Zhai, P. (2013). Observations: atmosphere and surface. In Climate change 2013 the physical science basis: Working group I contribution to the fifth assessment report of the intergovernmental panel on climate change (pp. 159-254). Cambridge University Press.

Helm, K. P., Bindoff, N. L., & Church, J. A. (2010). Changes in the global hydrological-cycle inferred from ocean salinity. Geophysical Research Letters, 37(18), L18701. https://doi.org/10.1029/2010GL044222

Henley, B. J., Gergis, J., Karoly, D. J., Power, S., Kennedy, J., & Folland, C. K. (2015). A tripole index for the interdecadal Pacific oscillation. Climate Dynamics, 45(11–12), 3077–3090. https://doi.org/10.1007/s00382-015-2525-1

Huang, B., Thorne, P. W., Banzon, V. F., Boyer, T., Chepurin, G., Lawrimore, J. H., ... & Zhang, H. M. (2017). Extended reconstructed sea surface temperature, version 5 (ERSSTv5): upgrades, validations, and intercomparisons. Journal of Climate, 30(20), 8179-8205.

IPCC (2013), Climate Change 2013: The Physical Science Basis. Contribution of Working Group I to the Fifth Assessment Report of the Intergovernmental Panel on Climate Change, Cambridge Univ. Press, Cambridge, U. K, 1535 pp.

Irving, D. B., Wijffels, S., & Church, J. A. (2019). Anthropogenic aerosols, greenhouse gases, and the uptake, transport, and storage of excess heat in the climate system. Geophysical Research Letters, 46(9), 4894–4903. https://doi.org/10.1029/2019GL082015

Ishii, M., Fukuda, Y., Hirahara, S., Yasui, S., Suzuki, T., & Sato, K. (2017). Accuracy of global upper ocean heat content estimation expected from present observational data sets. Sola, 13, 163–167. https://doi.org/10.2151/sola.2017-030

Johnson, G. C., & Lyman, J. M. (2020). Warming trends increasingly dominate global ocean. Nature Climate Change, 10(8), 757–761. https://doi.org/10.1038/s41558-020-0822-0

Johnson, G. C., Lyman, J. M., Boyer, T., Cheng, L., Domingues, C. M., Gilson, J., et al. (2020). Ocean heat content [in ‘State of the Climate in 2019’]. Bulletin of the American Meteorological Society, 101(8), S140–S144. https://doi.org/10.1175/BAMS-D-20-0105.1

Karl, T. R., Arguez, A., Huang, B., Lawrimore, J. H., McMahon, J. R., Menne, M. J., ... & Zhang, H. M. (2015). Possible artifacts of data biases in the recent global surface warming hiatus. Science, 348(6242), 1469-1472.

Kaufmann, R. K., Kauppi, H., Mann, M. L., & Stock, J. H. (2011). Reconciling anthropogenic climate change with observed temperature 1998–2008. Proceedings of the National Academy of Sciences, 108(29), 11790-11793.

Kay, J. E., Deser, C., Phillips, A., Mai, A., Hannay, C., Strand, G., ... & Vertenstein, M. (2015). The Community Earth System Model (CESM) large ensemble project: A community resource for studying climate change in the presence of internal climate variability. Bulletin of the American Meteorological Society, 96(8), 1333-1349.

Knight, J. R., Allan, R. J., Folland, C. K., Vellinga, M., & Mann, M. E. (2005). A signature of persistent natural thermohaline circulation cycles in observed climate. Geophysical Research Letters, 32(20).

Kobayashi, S., Ota, Y., Harada, Y., Ebita, A., Moriya, M., Onoda, H., et al. (2015). The JRA-55 reanalysis: General specifications and basic characteristics. Journal of Meteorological Society of Japan, 93(1), 5–48. https://doi.org/10.2151/jmsj.2015-001

Köhl, A. (2014). Detecting processes contributing to interannual halosteric and thermosteric sea level variability. Journal of Climate, 27(6), 2417–2426. https://doi.org/10.1175/JCLI-D-13-00412.1

Kosaka, Y., & Xie, S. P. (2013). Recent global-warming hiatus tied to equatorial Pacific surface cooling. Nature, 501(7467), 403-407.

Kucharski, F., Ikram, F., Molteni, F., Farneti, R., Kang, I. S., No, H. H., ... & Mogensen, K. (2016). Atlantic forcing of Pacific decadal variability. Climate Dynamics, 46(7-8), 2337-2351.

Lean, J. L., & Rind, D. H. (2009). How will Earth's surface temperature change in future decades?. Geophysical Research Letters, 36(15).

Lee, S. K., Park, W., Baringer, M. O., Gordon, A. L., Huber, B., & Liu, Y. (2015). Pacific origin of the abrupt increase in Indian Ocean heat content during the warming hiatus. Nature Geoscience, 8(6), 445–449. https://doi.org/10.1038/ngeo2438

Levitus, S., J. I. Antonov, T. P. Boyer, O. K. Baranova, H. E. Garcia, et al. (2012), World ocean heat content and thermosteric sea level change (0-2000 m), 1955-2010, Geophys. Res. Lett. , 39, doi:10.1029/2012gl051106.

Li, Q., & England, M. H. (2020). Tropical Indo-Pacific teleconnections to Southern Ocean mixed layer variability. Geophysical Research Letters, 47(15), e2020GL088466. https://doi.org/10.1029/2020GL088466

Li, X., Xie, S. P., Gille, S. T., & Yoo, C. (2016). Atlantic-induced pan-tropical climate change over the past three decades. Nature Climate Change, 6(3), 275-279.

Li, Y., Han, W., & Zhang, L. (2017). Enhanced decadal warming of the southeast Indian Ocean during the recent global surface warming slowdown. Geophysical Research Letters, 44(19), 9876–9884. https://doi.org/10.1002/2017GL075050

Liu, W., Lu, J., Xie, S. P., & Fedorov, A. (2018). Southern Ocean heat uptake, redistribution, and storage in a warming climate: The role of meridional overturning circulation. Journal of Climate, 31(12), 4727–4743. https://doi.org/10.1175/JCLI-D-17-0761.1

Llovel, W., & Terray, L. (2016). Observed southern upper-ocean warming over 2005–2014 and associated mechanisms. Environmental Research Letters, 11(12), 124023. https://doi.org/10.1088/1748-9326/11/12/124023

Loeb, N. G., Lyman, J. M., Johnson, G. C., Allan, R. P., Doelling, D. R., Wong, T., ... & Stephens, G. L. (2012). Observed changes in top-of-the-atmosphere radiation and upper-ocean heating consistent within uncertainty. Nature Geoscience, 5(2), 110-113. https://doi.org/10.1038/ngeo1375.

Lyu, K., Zhang, X., Church, J. A., & Wu, Q. (2020). Processes responsible for the southern hemisphere ocean heat uptake and redistribution under anthropogenic warming. Journal of Climate, 33(9), 3787–3807. https://doi.org/10.1175/JCLI-D-19-0478.1

Lyu, K., Zhang, X., Church, J. A., Hu, J., & Yu, J. Y. (2017). Distinguishing the quasi-decadal and multidecadal sea level and climate variations in the Pacific: Implications for the ENSO-like low-frequency variability. Journal of Climate, 30(13), 5097–5117. https://doi.org/10.1175/JCLI-D-17-0004.1

Maher, N., England, M. H., Gupta, A. S., & Spence, P. (2018). Role of Pacific trade winds in driving ocean temperatures during the recent slowdown and projections under a wind trend reversal. Climate Dynamics, 51(1), 321-336.

Makarim, S., Sprintall, J., Liu, Z., Yu, W., Santoso, A., Yan, X. H., & Susanto, R. D. (2019). Previously unidentified Indonesian Throughflow pathways and freshening in the Indian Ocean during recent decades. Scientific Reports, 9(1), 7364. https://doi.org/10.1038/s41598-019-43841-z

Marsh, D. R., Mills, M. J., Kinnison, D. E., Lamarque, J. F., Calvo, N., & Polvani, L. M. (2013). Climate change from 1850 to 2005 simulated in CESM1 (WACCM). Journal of climate, 26(19), 7372-7391.

Marshall, D. P., & Zanna, L. (2014). A conceptual model of ocean heat uptake under climate change. Journal of Climate, 27(22), 8444-8465.

Marshall, G. J. (2003). Trends in the Southern Annular Mode from observations and reanalyses. Journal of Climate, 16(24), 4134–4143. https://doi.org/10.1175/1520-0442(2003)016<4134:TITSAM>2.0.CO;2

McGregor, S., Timmermann, A., Stuecker, M. F., England, M. H., Merrifield, M., Jin, F. F., & Chikamoto, Y. (2014). Recent Walker circulation strengthening and Pacific cooling amplified by Atlantic warming. Nature Climate Change, 4(10), 888-892.

Meehl, G. A., Arblaster, J. M., Bitz, C. M., Chung, C. T., & Teng, H. (2016)a. Antarctic sea-ice expansion between 2000 and 2014 driven by tropical Pacific decadal climate variability. Nature Geoscience, 9(8), 590-595.

Meehl, G. A., Arblaster, J. M., Chung, C. T., Holland, M. M., DuVivier, A., Thompson, L., ... & Bitz, C. M. (2019). Sustained ocean changes contributed to sudden Antarctic sea ice retreat in late 2016. Nature communications, 10(1), 1-9.

Meehl, G. A., Hu, A., Santer, B. D., & Xie, S. P. (2016)b. Contribution of the Interdecadal Pacific Oscillation to twentieth-century global surface temperature trends. Nature Climate Change, 6(11), 1005-1008.

Meehl, G. A., Washington, W. M., Arblaster, J. M., Hu, A., Teng, H., Kay, J. E., ... & Strand, W. G. (2013). Climate change projections in CESM1 (CAM5) compared to CCSM4. Journal of Climate, 26(17), 6287-6308.

Meijers, A. J. S., Bindoff, N. L., & Rintoul, S. R. (2011). Frontal movements and property fluxes: Contributions to heat and freshwater trends in the Southern Ocean. Journal of Geophysical Research, 116(C8), C08024. https://doi.org/10.1029/2010JC006832

Meijers, A. J. S., Cerovečki, I., King, B. A., & Tamsitt, V. (2019). A see-saw in Pacific subantarctic mode water formation driven by atmospheric modes. Geophysical Research Letters, 46(22), 13152–13160. https://doi.org/10.1029/2019GL085280

Morice, C. P., Kennedy, J. J., Rayner, N. A., & Jones, P. D. (2012). Quantifying uncertainties in global and regional temperature change using an ensemble of observational estimates: The HadCRUT4 data set. Journal of Geophysical Research: Atmospheres, 117(D8).

Morrison, A. K., Griffies, S. M., Winton, M., Anderson, W. G., & Sarmiento, J. L. (2016). Mechanisms of Southern Ocean heat uptake and transport in a global eddying climate model. Journal of Climate, 29(6), 2059-2075.

Otterå, O. H., Bentsen, M., Drange, H., & Suo, L. (2010). External forcing as a metronome for Atlantic multidecadal variability. Nature Geoscience, 3(10), 688-694.

Qu, T., Fukumori, I., & Fine, R. A. (2019). Spin-up of the Southern Hemisphere super gyre. Journal of Geophysical Research: Oceans, 124, 154–170. https://doi.org/10.1029/2018JC014391

Qu, T., Gao, S., & Fine, R. A. (2020). Variability of the sub-Antarctic mode water subduction rate during the argo period. Geophysical Research Letters, 47(13), e2020GL088248. https://doi.org/10.1029/2020GL088248

Queste, B. Y., Abrahamsen, E. P., du Plessis, M. D., Gille, S. T., Gregor, L., Mazloff, M. R., et al. (2020). Southern Ocean [in 'State of the Climate in 2019']. Bulletin of the American Meteorological Society, 101(8), S307–S309. https://doi.org/10.1175/BAMS-D-20-0090.1

Rathore, S., Bindoff, N. L., Phillips, H. E., & Feng, M. (2020). Recent hemispheric asymmetry in global ocean warming induced by climate change and internal variability. Nature Communications, 11(1), 2008. https://doi.org/10.1038/s41467-020-15754-3

Rhein, M., Rintoul, S. R., Aoki, S., Campos, E., Chambers, D., Feely, R. A., ... & Talley, L. D. (2013). Observations: ocean.

Rodríguez-Fonseca, B., Polo, I., García-Serrano, J., Losada, T., Mohino, E., Mechoso, C. R., & Kucharski, F. (2009). Are Atlantic Niños enhancing Pacific ENSO events in recent decades?. Geophysical Research Letters, 36(20).

Roemmich, D., & Gilson, J. (2009). The 2004–2008 mean and annual cycle of temperature, salinity, and steric height in the global ocean from the Argo Program. Progress in Oceanography, 82(2), 81–100. https://doi.org/10.1016/j.pocean.2009.03.004

Roemmich, D., Church, J., Gilson, J., Monselesan, D., Sutton, P., & Wijffels, S. (2015). Unabated planetary warming and its ocean structure since 2006. Nature Climate Change, 5(3), 240–245. https://doi.org/10.1038/nclimate2513

Roemmich, D., Gilson, J., Sutton, P., & Zilberman, N. (2016). Multidecadal change of the South Pacific gyre circulation. Journal of Physical Oceanography, 46(6), 1871–1883. https://doi.org/10.1175/JPO-D-15-0237.1

Sallée, J. B. (2018). Southern ocean warming. Oceanography, 31(2), 52–62. https://doi.org/10.5670/oceanog.2018.215

Santer, B. D., Bonfils, C., Painter, J. F., Zelinka, M. D., Mears, C., Solomon, S., ... & Wentz, F. J. (2014). Volcanic contribution to decadal changes in tropospheric temperature. Nature Geoscience, 7(3), 185-189. https://doi.org/10.1038/ngeo2098

Schneider, D. P., Deser, C., & Fan, T. (2015). Comparing the impacts of tropical SST variability and polar stratospheric ozone loss on the Southern Ocean westerly winds. Journal of Climate, 28(23), 9350-9372.

Seidov, D., & Maslin, M. (2001). Atlantic ocean heat piracy and the bipolar climate see-saw during Heinrich and Dansgaard–Oeschger events. Journal of Quaternary Science: Published for the Quaternary Research Association, 16(4), 321-328.

Silvy, Y., Guilyardi, E., Sallée, J. B., & Durack, P. J. (2020). Human-induced changes to the global ocean water masses and their time of emergence. Nature Climate Change, 10, 1–7.

Smith, D. M., Booth, B. B., Dunstone, N. J., Eade, R., Hermanson, L., Jones, G. S., ... & Thompson, V. (2016). Role of volcanic and anthropogenic aerosols in the recent global surface warming slowdown. Nature Climate Change, 6(10), 936-940.

Smith, T. M., Reynolds, R. W., Peterson, T. C., & Lawrimore, J. (2008). Improvements to NOAA's historical merged land–ocean surface temperature analysis (1880–2006). Journal of Climate, 21(10), 2283-2296.

Solomon, S., Daniel, J. S., Neely, R. R., Vernier, J. P., Dutton, E. G., & Thomason, L. W. (2011). The persistently variable "background" stratospheric aerosol layer and global climate change. Science, 333(6044), 866-870.

Solomon, S., Rosenlof, K. H., Portmann, R. W., Daniel, J. S., Davis, S. M., Sanford, T. J., & Plattner, G. K. (2010). Contributions of stratospheric water vapor to decadal changes in the rate of global warming. Science, 327(5970), 1219-1223.

Stauning, P. (2013). Reduced solar activity disguises global temperature rise. Atmospheric and Climate Sciences, 2014.

Stolpe, M. B., Medhaug, I., Sedláček, J., & Knutti, R. (2018). Multidecadal variability in global surface temperatures related to the Atlantic meridional overturning circulation. Journal of Climate, 31(7), 2889-2906.

Swart, N. C., & Fyfe, J. C. (2012). Observed and simulated changes in the Southern Hemisphere surface westerly wind-stress. Geophysical Research Letters, 39(16), L16711. https://doi.org/10.1029/2012GL052810

Swart, N. C., Gille, S. T., Fyfe, J. C., & Gillett, N. P. (2018). Recent Southern Ocean warming and freshening driven by greenhouse gas emissions and ozone depletion. Nature Geoscience, 11(11), 836–841. https://doi.org/10.1038/s41561-018-0226-1

Thompson, D. W., & Solomon, S. (2002). Interpretation of recent Southern Hemisphere climate change. Science, 296(5569), 895-899.

Ting, M., Kushnir, Y., & Li, C. (2014). North Atlantic multidecadal SST oscillation: External forcing versus internal variability. Journal of Marine Systems, 133, 27-38.

Ting, M., Kushnir, Y., Seager, R., & Li, C. (2009). Forced and internal twentieth-century SST trends in the North Atlantic. Journal of Climate, 22(6), 1469-1481.

Trenberth, K. E. (2015). Has there been a hiatus?. Science, 349(6249), 691-692.

Trenberth, K. E., & Dai, A. (2007). Effects of Mount Pinatubo volcanic eruption on the hydrological cycle as an analog of geoengineering. Geophysical Research Letters, 34(15).

Trenberth, K. E., Dai, A., Van Der Schrier, G., Jones, P. D., Barichivich, J., Briffa, K. R., & Sheffield, J. (2014). Global warming and changes in drought. Nature Climate Change, 4(1), 17-22.

Tung, K. K., & Zhou, J. (2013). Using data to attribute episodes of warming and cooling in instrumental records. Proceedings of the National Academy of Sciences, 110(6), 2058-2063.

Volkov, D. L., Lee, S. K., Gordon, A. L., & Rudko, M. (2020). Unprecedented reduction and quick recovery of the South Indian Ocean heat content and sea level in 2014–2018. Science Advances, 6(36), eabc1151. https://doi.org/10.1126/sciadv.abc1151

Volkov, D. L., Lee, S. K., Landerer, F. W., & Lumpkin, R. (2017). Decade-long deep-ocean warming detected in the subtropical South Pacific. Geophysical Research Letters, 44(2), 927–936. https://doi.org/10.1002/2016GL071661

von Schuckmann, K., Cheng, L., Palmer, M. D., Hansen, J., Tassone, C., et al. (2020). Heat stored in the Earth system: Where does the energy go? Earth System Science Data, 12(3), 2013–2041. https://doi.org/10.5194/essd-12-2013-2020

Watanabe, M., Shiogama, H., Tatebe, H., Hayashi, M., Ishii, M., & Kimoto, M. (2014). Contribution of natural decadal variability to global warming acceleration and hiatus. Nature Climate Change, 4(10), 893-897.

Wei, M., Qiao, F., & Deng, J. (2015). A quantitative definition of global warming hiatus and 50-year prediction of global-mean surface temperature. Journal of the Atmospheric Sciences, 72(8), 3281-3289.

Wu, Z., & Huang, N. E. (2009). Ensemble empirical mode decomposition: a noise-assisted data analysis method. Advances in adaptive data analysis, 1(01), 1-41.

Wu, Z., Huang, N. E., Wallace, J. M., Smoliak, B. V., & Chen, X. (2011). On the time-varying trend in global-mean surface temperature. Climate dynamics, 37(3), 759-773.

Xie, S. P., & Kosaka, Y. (2017). What caused the global surface warming hiatus of 1998–2013?. Current Climate Change Reports, 3(2), 128-140.

Yan, X. H., Boyer, T., Trenberth, K., Karl, T. R., Xie, S. P., Nieves, V., et al. (2016). The global warming hiatus: Slowdown or redistribution? Earth's Future, 4(11), 472–482. https://doi.org/10.1002/2016EF000417

Yao, S. L., Huang, G., Wu, R. G., & Qu, X. (2016). The global warming hiatus—a natural product of interactions of a secular warming trend and a multi-decadal oscillation. Theoretical and Applied Climatology, 123(1-2), 349-360.

Zhang, R., & Delworth, T. L. (2007). Impact of the Atlantic multidecadal oscillation on North Pacific climate variability. Geophysical Research Letters, 34(23).

Zhang, R., Delworth, T. L., Sutton, R., Hodson, D. L., Dixon, K. W., Held, I. M., ... & Vecchi, G. A. (2013). Have aerosols caused the observed Atlantic multidecadal variability?. Journal of the Atmospheric Sciences, 70(4), 1135-1144.

Zhang, W., & Yan, X. H. (2017). The subpolar North Atlantic Ocean heat content variability and its decomposition. Scientific Reports, 7(1), 13748. https://doi.org/10.1038/s41598-017-14158-6

Zhang, Y., Feng, M., Du, Y., Phillips, H. E., Bindoff, N. L., & McPhaden, M. J. (2018). Strengthened Indonesian Throughflow drives decadal

Zhang, Y., Wallace, J. M., & Battisti, D. S. (1997). ENSO-like interdecadal variability: 1900–93. Journal of climate, 10(5), 1004-1020.

Zika, J. D., Gregory, J. M., McDonagh, E. L., Marzocchi, A., & Clément, L. (2020). Recent water mass changes reveal mechanisms of ocean warming. https://doi.org/10.1175/JCLI-D-20-0355.1

Appendix A

SUPPLEMENTARY MATERIAL FOR CHAPTER 2

Figure A.1, Figure A.2, Table A.1 to Table A.2, and Multiple linear regression

Introduction

This file contains supplementary figures and tables supporting the analysis presented in the main manuscript file.

Figure A.1 to Figure A.2 is the total GST time series over 1920-2013 forced by CESM-LE and CESM-xaer experiments.

Table A.1 is the summary of the coupled climate model experiments used in part1, including the CESM-LE, CESM-xaer, Pacific Pacemaker and Atlantic Pacemaker.

Table A.2 is the summary of forced responses by model experiments. For example, the CESM-LE ensemble mean is used to identify the external forcing.

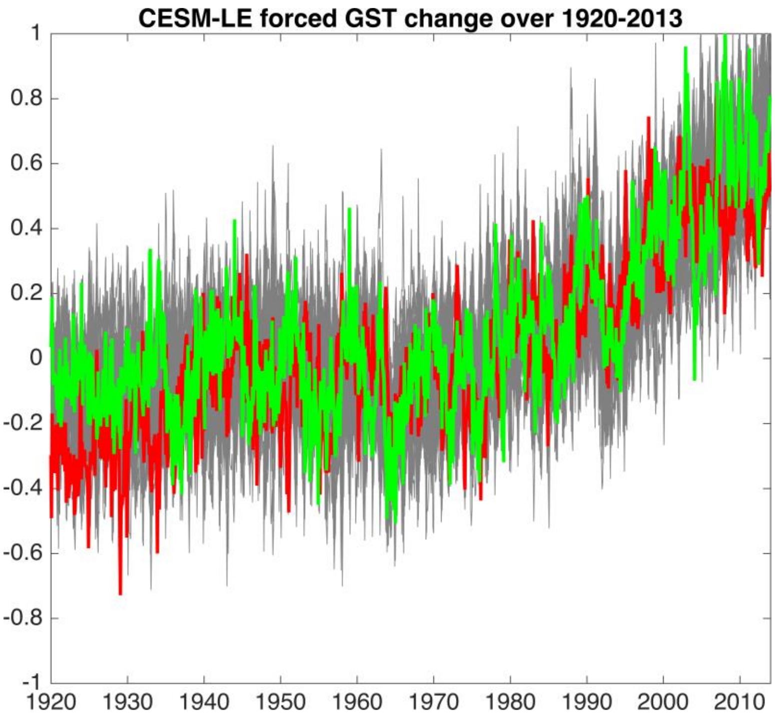

Figure A.1. GST change over 1920-2013 forced by CESM-LE experiment. The gray lines are ensemble members. The green line is the ensemble mean of CESM-LE. The red line is the observed GST change estimated by HadCRUT4 data set.

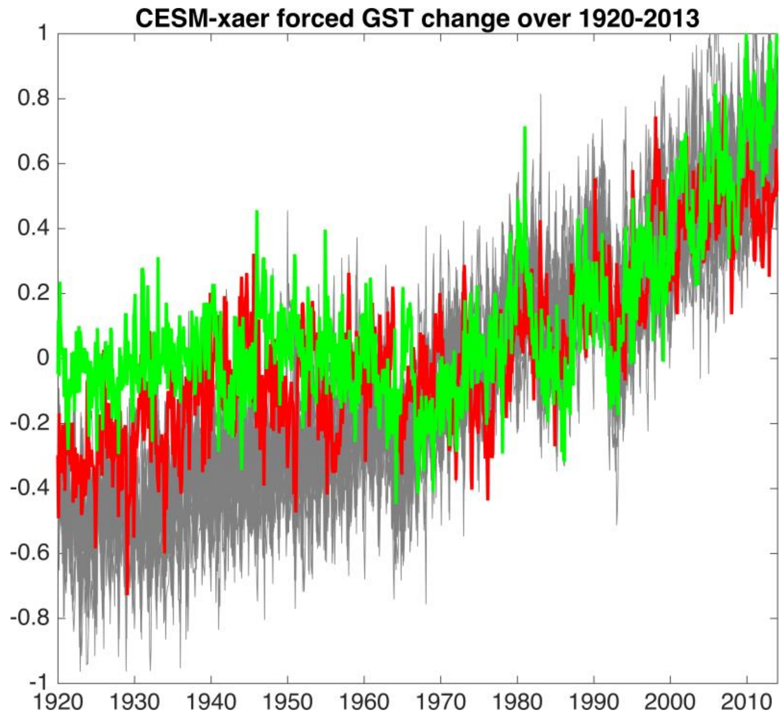

Figure A.2. GST change over 1920-2013 forced by CESM-xaer experiment. The gray lines are ensemble members. The green line is the ensemble mean of CESM- xaer. The red line is the observed GST change estimated by HadCRUT4 data set.

Table A.1 Summary of the CESM1 experiments

Experiments	Time-varying forcing	Ensemble members	Time
CESM-LE	All historical radiative forcings	40	1920-2100
CESM-xaer	All historical radiative forcings, but fixed industrial aerosol	20	1920-2080
Pacific Pacemaker	All historical radiative forcings+ Observed SST anomalies in eastern tropical Pacific (15ºN-15ºS;80º-180ºW)	20	1920-2013
Atlantic Pacemaker	All historical radiative forcings+ Observed SST anomalies in North Atlantic (5ºN-55ºN)	10	1920-2013

Table A.2 Summary of forced responses by model experiments

Forcing	Ensemble mean
External forcing	CESM-LE
Aerosol forcing	CESM-xaer
Pacific forcing	Pacific pacemaker ensemble member - Ensemble mean of CESM-LE
Atlantic forcing	Atlantic pacemaker ensemble member - Ensemble mean of CESM-LE

Methods

Multiple linear regression (MLR), also termed as multiple regression, is used to study the learner relationship between the dependent variable and multiple independent variables. The number of the predictors that used to predict the outcome in MLR are equal or larger than two. In this part, the MLR is applied to to model the linear relationship between the four components (IAV, IDV, MDV, ST) of GST and response SST variable.

$$y_i = \beta_0 + \beta_0 X_{i1} + \beta_1 X_{i2} + \beta_2 X_{i3} + \cdots + \beta_p X_{ip} + \varepsilon$$

Where, the i is the number of observations.

y_i is the dependent variable, here is the SST.

X_i represents the four signals, including IAV, IDV, MDV and ST.

β_0 is the intercept.

β_p is the slope coefficient for signals in different time scales.

ε is the model's error term. Known as the model residuals.

Appendix B

SUPPLEMENTARY MATERIAL FOR CHAPTER 3

Contents of this file

Figures B.1 to B.11

Introduction

This file contains supplementary figures supporting the analysis presented in the main manuscript file.

Figure B.1 to Figure B.3 show global zonal integrated OHC change and the spatial patterns over different time periods calculated from the Ishii data, the EN4 data and the Scripps Argo data.

Figure B.4 and Figure B.8 show the zonal and meridional averages of the vertical displacement of isopycnals over the periods of 2003-2012, 2013-2019 and 1960-2019 in the SPAC and SEIO regions, respectively.

Figure B.5, Figure B.7 and Figure B.9 depict the zonal averages of the changes in the potential temperature and salinity and their heave and spiciness components in the SPAC and the SEIO regions over the periods of 2003-2012, 2013-2019 and 1960-2019.

Figure B.6 and Figure B.10 show the spatial patterns of the temperature and the salinity spiciness changes along 26.75 kg/m3 during the periods of 2003-2012, 2013-2019 and 1960-2019.

Figure B.11 shows the vertical displacement of isopycnals and the hodograph of the heave versus spiciness anomalies in the SEIO region.

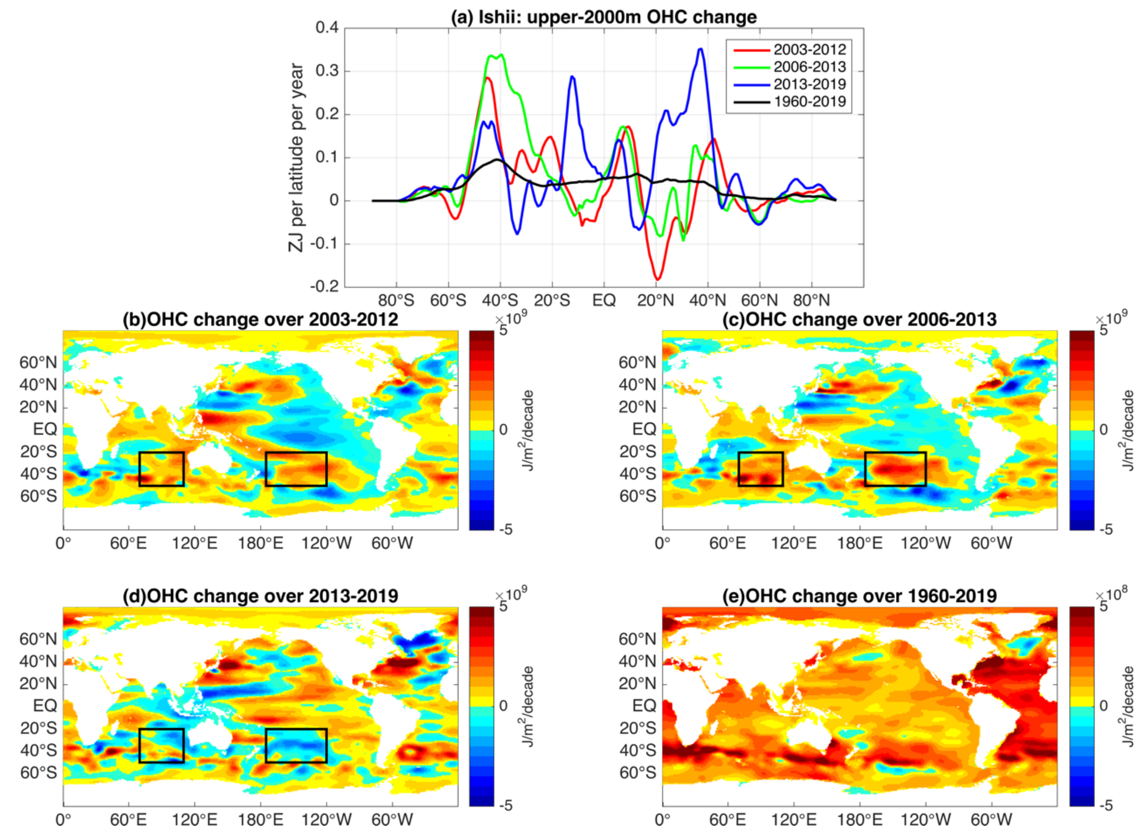

Figure B.1. Similar as in Figure 3.1 but for the upper-2000m depth-integrated OHC changes calculated from the Ishii data. (a) Global zonal integrated OHC changes (ZJ per degree latitude per year) over 2003–2012 (red line), 2006–2013 (green line), 2013–2019 (blue line), and 1960–2019 (black line). (b)-(e) Spatial patterns of OHC changes (J/m^2/decade) during 2003–2012, 2013–2019, 2006–2013, and 1960–2019, respectively; The black boxes in (b)-(d) indicate the two studying regions in the SEIO (20°–50°S, 70°–110°E) and SPAC (185°–240°S, 20°–50°E).

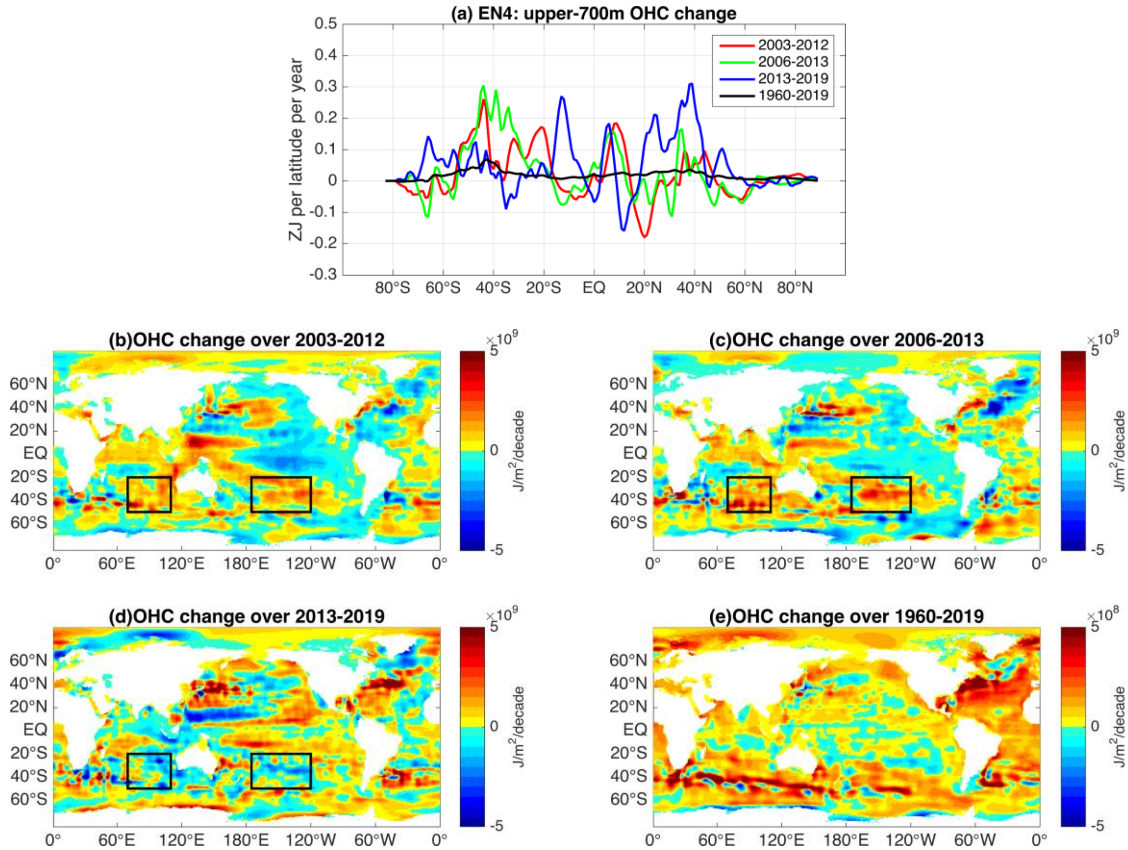

Figure B.2. Similar as in Figure 3.1 but for the upper-700m depth-integrated OHC changes calculated from EN4 data. (a) Global zonal integrated OHC changes (ZJ per degree latitude per year) during 2003–2012 (red line), 2006–2013 (green line), 2013–2019 (blue line), and 1960–2019 (black line). (b)-(e) Spatial patterns of OHC changes (J/m^2/decade) during 2003–2012, 2013–2019, 2006–2013, and 1960–2019, respectively; The black boxes in (b)-(d) indicate the two studying regions in the SEIO (20°–50°S, 70°–110°E) and SPAC (185°–240°S, 20°–50°E).

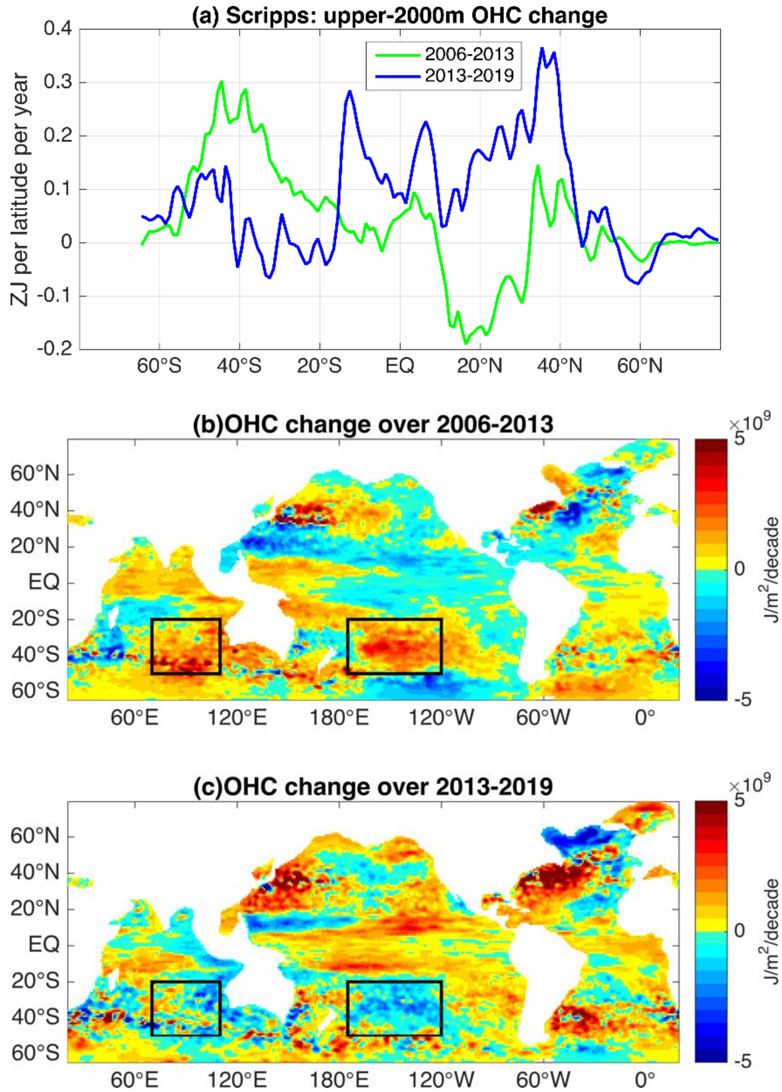

Figure B.3. Similar as in Figure 3.1 but for the upper-2000m depth-integrated OHC changes calculated from the Scripps Argo data. (a) Global zonal integrated OHC changes (ZJ per degree latitude per year) during 2006–2013 (green line) and 2013–2019 (blue line). (b)-(c) Spatial patterns of OHC changes (J/m^2/decade) during 2006–2013 and 2013–2019. The black boxes in (b)-(c) indicate the two studying regions in the SEIO (20°–50°S, 70°–110°E) and SPAC (185°–240°S, 20°–50°E).

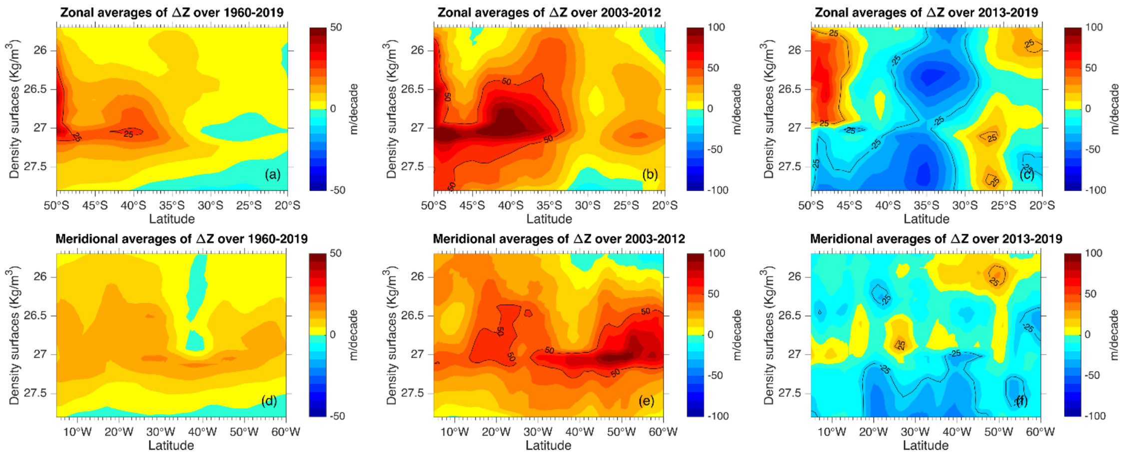

Figure B.4. Zonal and Meridional averages of the vertical displacement (m/decade, positive downward) of isopycnals in the SPAC region over (left panels) 1960–2019, (middle panels) 2003–2012 and (right panels) 2013–2019.

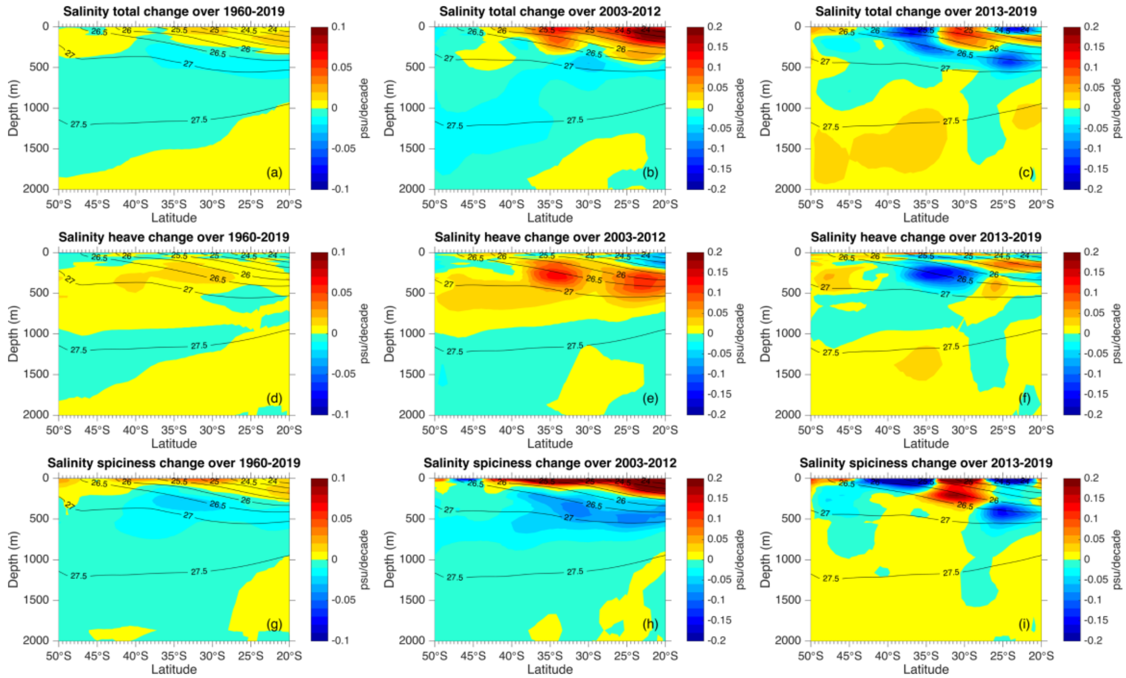

Figure B.5. Similar as in Figure 3 but for zonal averages of the changes in the salinity, heave, and spiciness components (°C/decade) in the SPAC region over (left panels) 1960–2019, (middle panels) 2003–2012 and (right panels) 2013–2019. The mean density surfaces over each period are superimposed as contours.

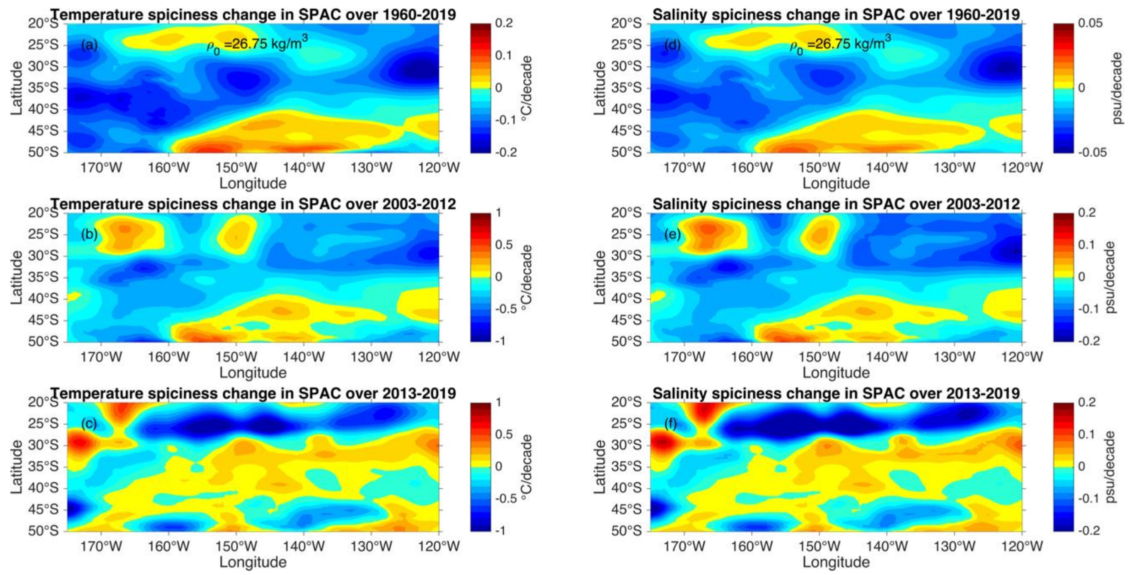

Figure B.6. Spatial patterns of the potential temperature spiciness changes (Unit: °C/decade, left panels) and the salinity spiciness changes (Unit: psu/decade, right panels) along 26.75 kg/m^3 in the SPAC region. (Upper panels) 1960-2019; (middle panels) 2003-2012; (lower panels) 2013-2019.

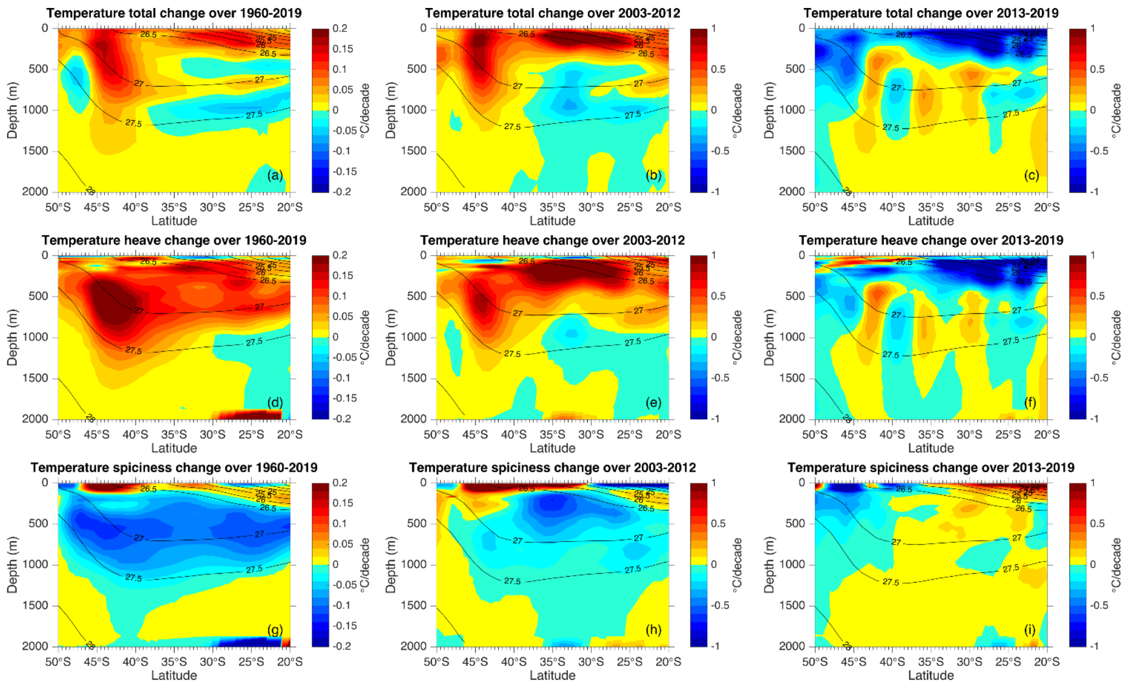

Figure B.7. Similar as in Figure 3.3 but for the zonal averages of the changes in the potential temperature, heave, and spiciness components (°C/decade) in the SEIO region over (left panels) 1960–2019, (middle panels) 2003–2012, and (right panels) 2013–2019. The mean density surfaces over each period are superimposed as contours.

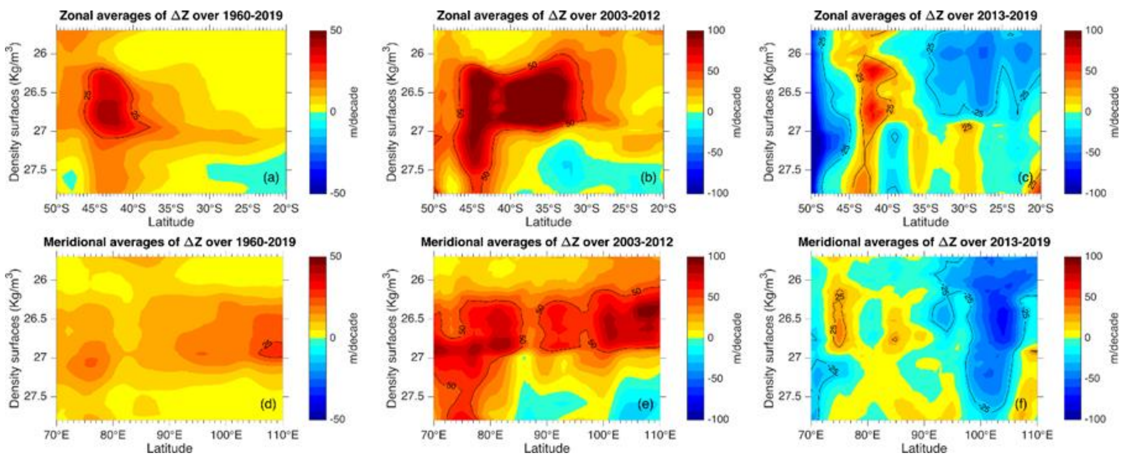

Figure B.8. Zonal and Meridional averages of the vertical displacement (m/decade, positive downward) of isopycnals in the SEIO region over (left panels) 1960–2019, (middle panels) 2003–2012, and (right panels) 2013–2019.

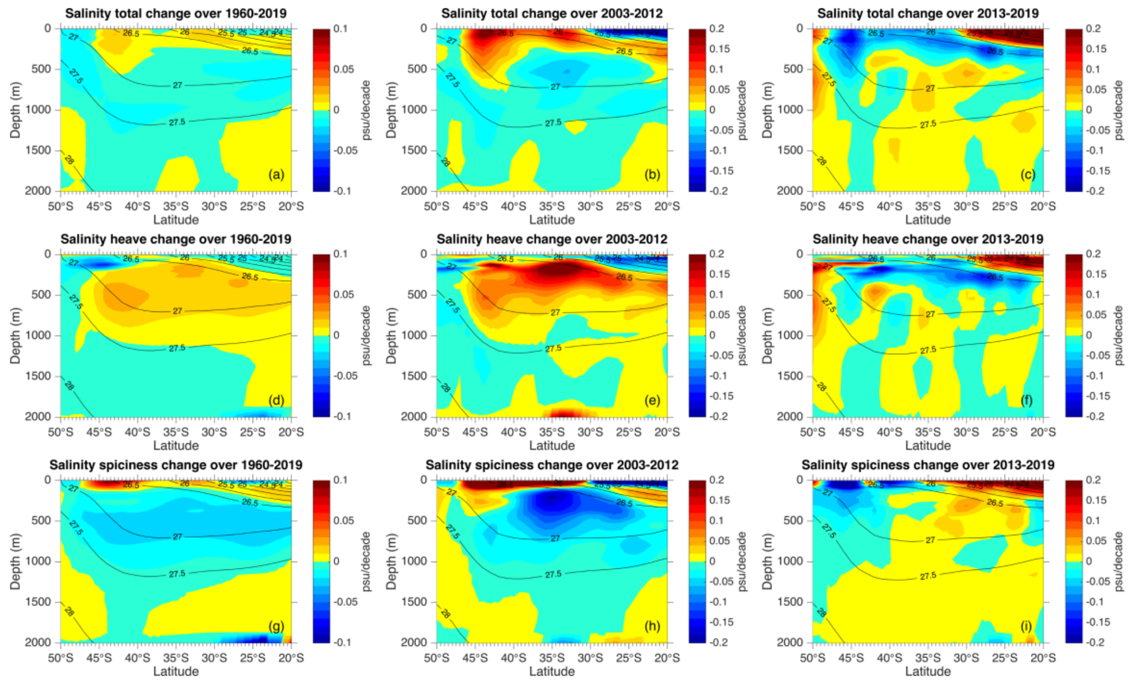

Figure B.9. Similar as in Figure 3.3 but for zonal averages of the changes in the salinity, heave, and spiciness components (°C/decade) in the SEIO region over (left panels) 1960–2019, (middle panels) 2003–2012, and (right panels) 2013–2019. The mean density surfaces over each period are superimposed as contours.

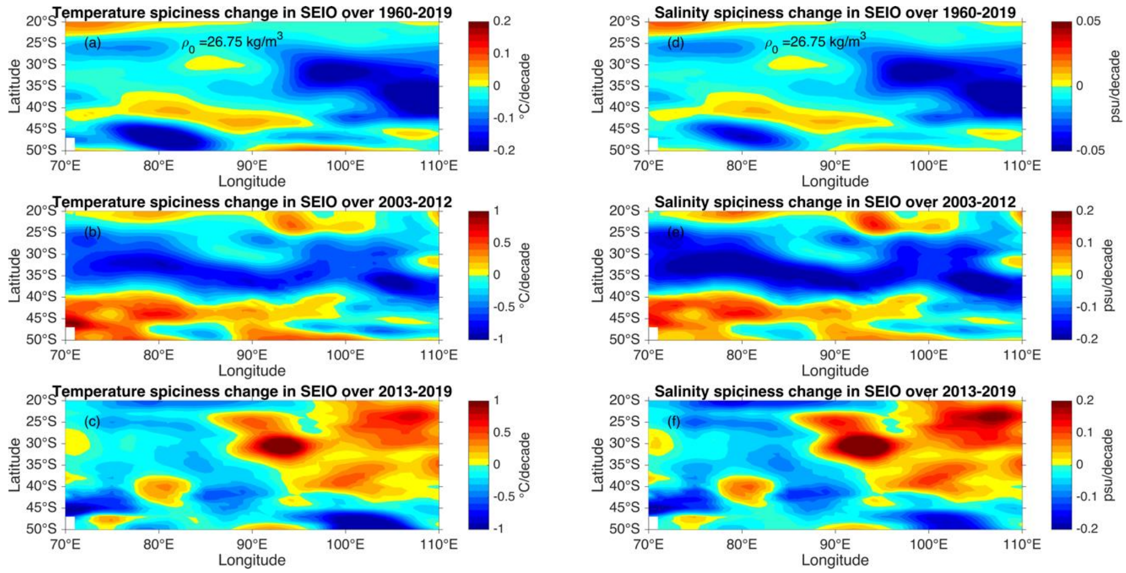

Figure B.10. Spatial patterns of the potential temperature spiciness changes (Unit: °C/decade, left panels) and the salinity spiciness changes (Unit: psu/decade, right panels) along 26.75 kg/m^3 in the SEIO region. (Upper panels) 1960-2019; (middle panels) 2003-2012; (lower panels) 2013-2019.

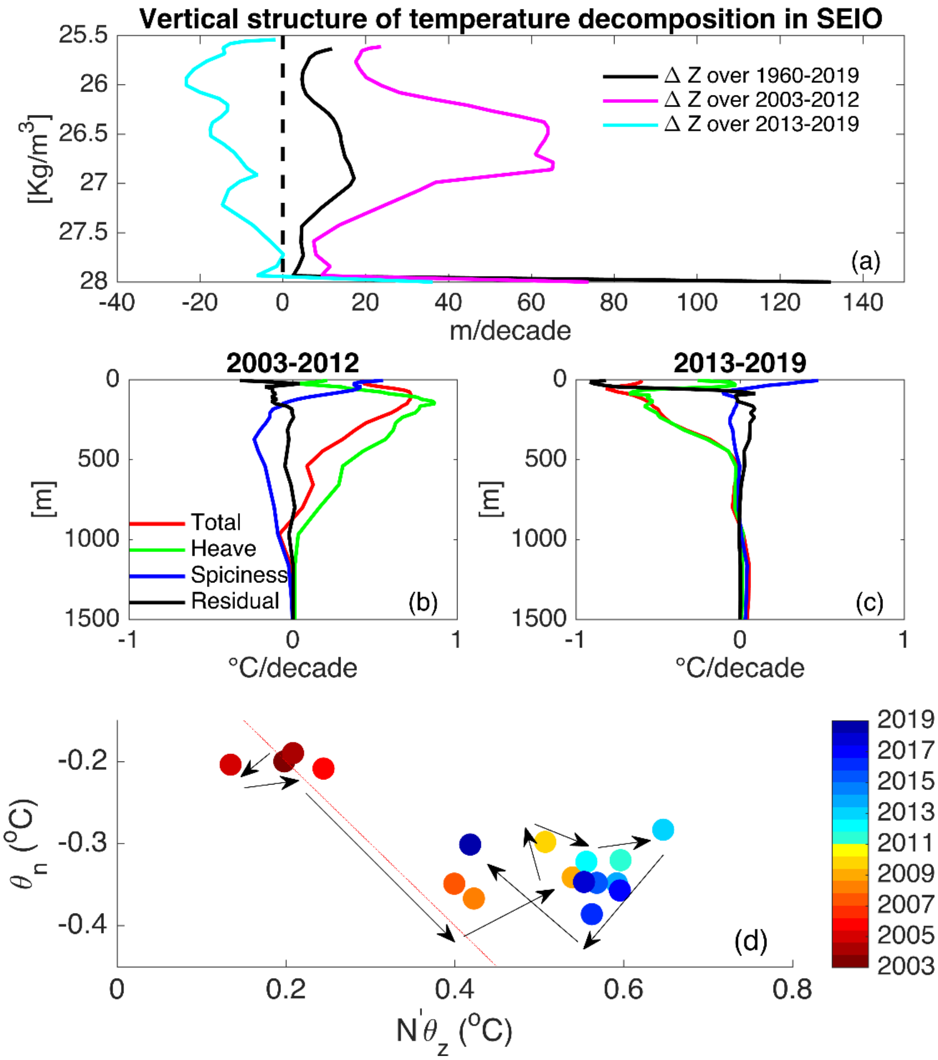

Figure B.11. Similar as in Figure 3.4 but for the vertical structure of temperature decomposition in the SEIO region. (a) Vertical displacement (m/decade) of the density surfaces in the SEIO region over 1960–2019 (black line), 2003–2012 (pink line), and 2013–2019 (cyan line). (b) Vertical profiles of the temperature changes (red line) along with heave (green line), spiciness (blue line), and residual (black line) components over 2003–2012 in the SEIO region. (c) Similar as in (b) but for changes over 2013–2019. (d) Hodograph of the heave and spiciness components of the 200–700m annual temperature anomalies relative to 1960–1980 in the SEIO region. The red dashed line indicates the zero temperature anomalies, as the heave and spiciness components cancel each other out. The colors of the circles and the arrows illustrate the time evolution from 2003 to 2019.

Appendix C

SUPPLEMENTARY MATERIAL FOR CHAPTER 4

Contents of this file

Figures C.1 to C.3

Introduction

This file contains supplementary figures supporting the analysis presented in the main manuscript file.

Figure C.1 show the spatial pattern of global zonal integrated OHC changes over different time periods calculated from the IAP data, the CESM-LE model, CESM-PAC model and the difference between these two models.

Figure C.2 to C.3 show the globally zonal integrated OHC changes (ZJ per degree latitude per year) in the upper 2000m over 1979-2013, 2003–2012 and 2006-2013 from the IAP, CESM-LE and CESM-PAC models.

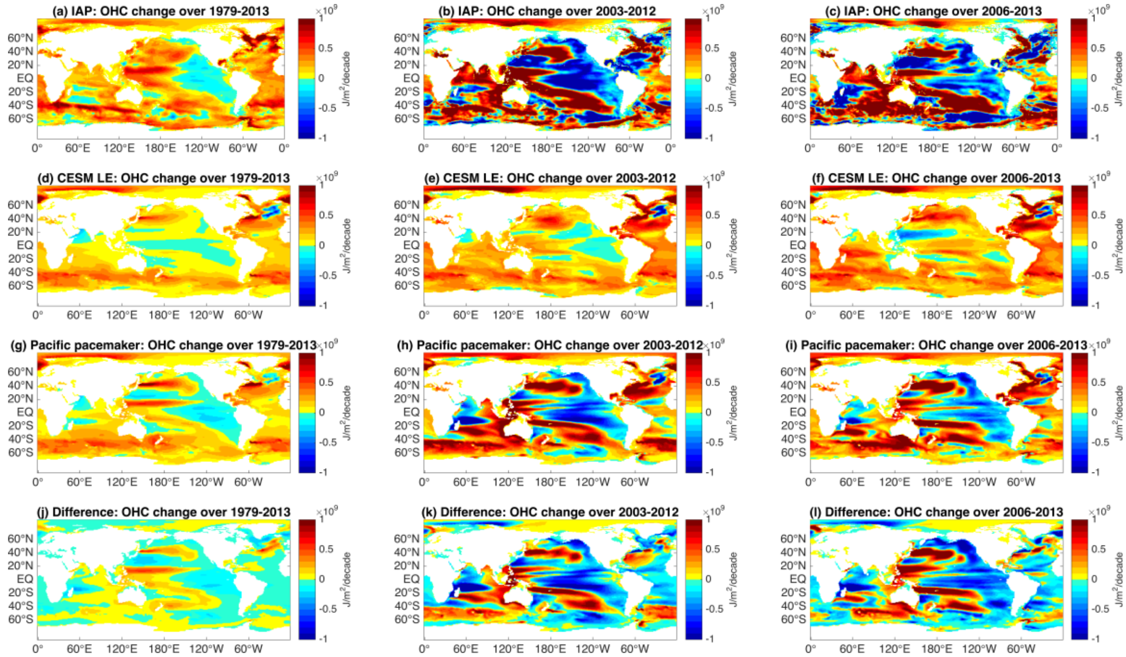

Figure C.1. The Upper-2000m depth-integrated OHC changes calculated from the IAP data and model simulations. (a) Spatial patterns of the OHC changes (J/m^2/decade) over 1979-2013, 2003-2012,2006-2013. (a)-(c) is from IAP data set. (d)-(e) is from CESM-LE model experiment. (g)-(i) is from the Pacific Pacemaker model experiment. (j)-(l) is obtained from Pacific Pacemaker model experiment minus CESM-LE ensemble mean.

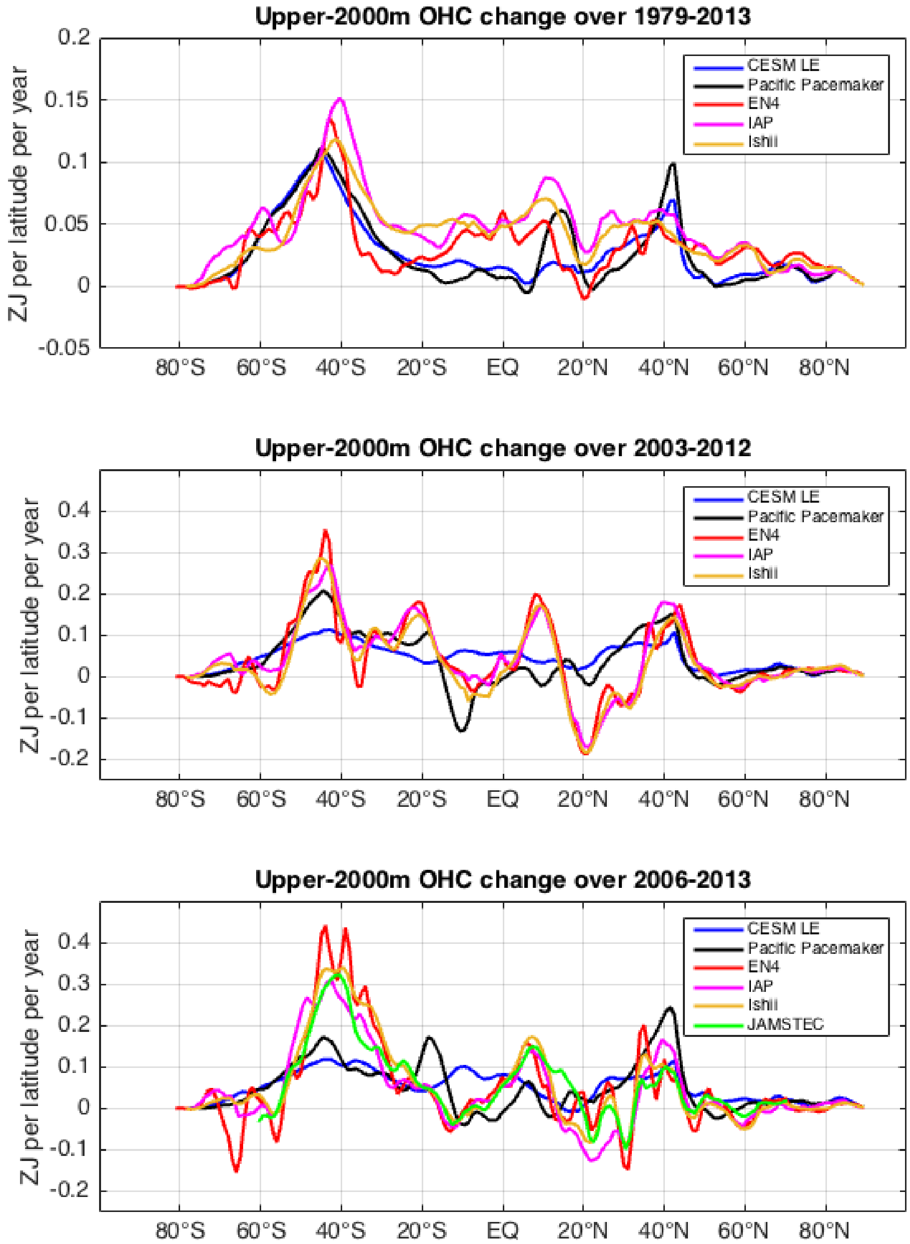

Figure C.2. Globally zonal integrated OHC changes (ZJ per degree latitude per year) in the upper 2000m over 1979-2013(a), 2003–2012 (b) and 2006-2013(c). CESM-LE (blue), Pacific Pacemaker (black), EN4(red), IAP(Magenta), Ishii (orange), JAMSTEC (green).

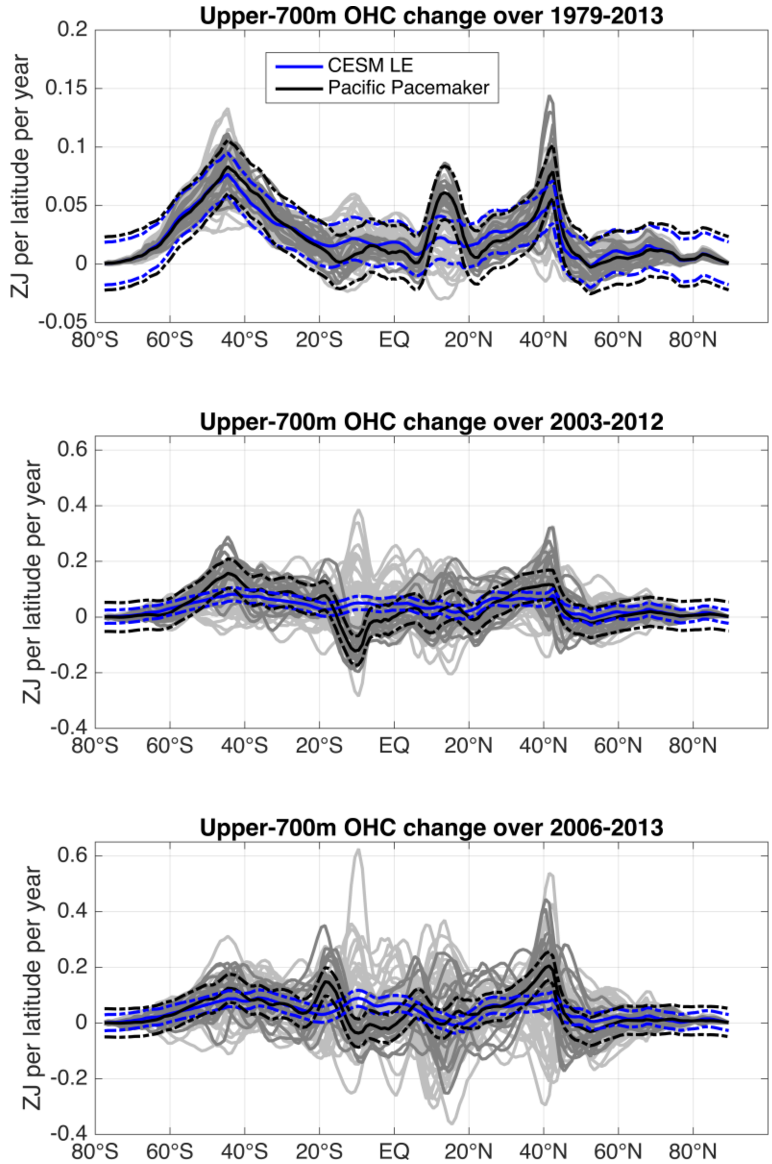

Figure C.3. Globally zonal integrated OHC changes (ZJ per degree latitude per year) in the upper 700m over 1979-2013(a), 2003–2012 (b) and 2006-2013(c). The light gray lines are CESM-LE ensemble members. The dark gray lines are Pacific Pacemaker ensemble members. The blue lines are CESM-LE ensemble means and the dashed blue lines are the standard deviation of the CESM-LE ensemble mean. The same for Pacific Pacemaker, the black lines are Pacific Pacemaker ensemble means and the dashed black lines are the standard deviation of the Pacific Pacemaker ensemble mean with a uniform bin width (0.1 °C/decade). The line is calculated by probability density function with mean and standard value.

Table C.1 Summary of correlations between EOF1 and index

EOF and Index	Correlation coefficient (r)
EOF1 (IAP) & IPO index	-0.86
EOF1 (IAP) & Nino 3.4 index	-0.83
EOF2 (IAP) & SAM index	0.76

Appendix D

PUBLICATIONS

Published:

Wang, Lina, et al. "Analysis of seasonal characteristics of water exchange in Beibu Gulf based on a particle tracking model." Regional Studies in Marine Science 18 (2018): 35-43.

Wang, Lina, et al. "Recent Shift in the Warming of the Southern Oceans Modulated by Decadal Climate Variability." Geophysical Research Letters: e2020GL090889.

In preparation:

Wang, Lina, et al. " Frequency-dependent modulators of the historical global surface temperature change' In processing.

Appendix E

PERMISSIONS FROM JOURNALS

This Agreement between Dr. Lina Wang ("You") and John Wiley and Sons ("John Wiley and Sons") consists of your license details and the terms and conditions provided by John Wiley and Sons and Copyright Clearance Center.

License Number	5042801347404
License date	Apr 05, 2021
Licensed Content Publisher	John Wiley and Sons
Licensed Content Publication	Geophysical Research Letters
Licensed Content Title	Recent Shift in the Warming of the Southern Oceans Modulated by Decadal Climate Variability
Licensed Content Author	Lina Wang, Kewei Lyu, Wei Zhuang, et al
Licensed Content Date	Feb 3, 2021
Licensed Content Volume	48
Licensed Content Issue	3
Licensed Content Pages	10
Type of use	Dissertation/Thesis
Requestor type	Author of this Wiley article
Format	Print and electronic
Portion	Full article
Will you be translating?	No
Title	research assistant
Institution name	university of delaware
Expected presentation date	May 2021
Requestor Location	Dr. Lina Wang 614 loveville road, Apartment B4G

	HOCKESSIN, DE 19707 United States Attn: Dr. Lina Wang
Publisher Tax ID	EU826007151
Total	0.00 USD